The impact of atmospheric stability on the global blockage effect of offshore wind farms

Master of Science Thesis - J. van Til

TU Delft

The impact of atmospheric stability on the global blockage effect of offshore wind farms

by

Master of Science Thesis - J. van Til

to obtain the degree of Master of Science

at the Delft University of Technology,

to be defended publicly on Thursday December 15, 2021 at 15:00 PM.

Student number:	4315898
Project duration:	January 19th 2021 - December 15th 2021

Thesis committee:

Prof. Dr. S. J. Watson,	TU Delft, Wind Energy (AE)	Chairman
Dr. Ir. D. J. N. Allaerts,	TU Delft, Wind Energy (AE)	Thesis supervisor
Dr. S. R. de Roode,	TU Delft, Geoscience & Remote Sensing (CEG)	Thesis committee member

TU Delft

Preface

This thesis report was produced during possibly the most challenging times of the 21st century, while the (wind) energy sector experiences both a major transition and a wave of criticism from public opinion. Initially, this thesis aimed to develop a linearised RANS wind farm modelling software but was redirected after two months as this intended research gap was filled by the availability of the newly developed linearised RANS wind farm modelling software: ORFEUS.

While writing this report, I assumed the reader to have previous knowledge of wind energy, fluid dynamics and the modelling of those two. The thesis contains the necessary theory to understand and follow the research. Emphasis for understanding this research lies in Chapter 4, which explains the key strategies.

I desire to express my thanks to Dries Allaerts who supervised my thesis from the very start on a consistent level. Dries gave me the freedom and advice on redirecting the thesis into a different field from his and the initially intended research. He gave me the required support, constructive criticism and feedback to increase the quality of work. Although we have seen each other only twice in real life, I valued the times we met.

Antonio Segalini for being open-minded, without hesitation, determined to help out a student from a different country and university. This work was made possible by the willingness to share the unpublished, newly developed wind modelling software ORFEUS. Flexibility and for being able to meet at almost any time of the day (or night). J. Strickland for willing to share the results of her LES study to improve the quality of this thesis. Furthermore, Jakob Economou (Winterwind), Wim Bierbooms (TU Delft) and Lizet Ramirez (WindEurope) for helping me out with research data and background theory. My family Jan, Gerdine and Sam van Til for providing me with mental support, distraction and even with feedback when needed. The international community of MSc SET and its study association DSEA for providing the social safety net. Furthermore my roommates, other family members, colleagues at the Faculty of 3mE and friends for pulling me through the thesis. Lastly, I want to thank the 4J's for providing the opportunity to study, sport (tennis and rowing (RIP)) and hang out.

I hope that this thesis inspires you as a reader to have increased interest in offshore wind energy, be it on a technical level or not. For me personally, this has been the most fun project to work on throughout my 8.5 years of studying at the Technical University of Delft. I will always look back to this thesis and master's with a warm and whole feeling.

Delft, December 2021
Justin van Til

Abstract

OBJECTIVE: This thesis research is set up to increase the knowledge on the influence of atmospheric stability on the Global Blockage Effect (GBE) of offshore wind farm flows, thereby aiming to improve the accuracy of energy yield calculations and predictions of offshore wind farms.
METHODOLOGY: Numerical simulations were run with the linearised Reynolds-averaged Navier–Stokes (RANS) modelling software ORFEUS comparing a fictitious 5 by 5 farm case with an isolated row case and a freestanding turbine case in order to quantify the GBE, after a verification study and a validation with both an empirical function and J. Strickland's LES study on the GBE. To find out more about the effect of the atmospheric stability on the GBE, under varying atmospheric stability, different farm layouts under different freestream wind speeds were simulated. Quantifying the GBE both by looking at the power deficit as well as upstream velocity deficit. Comparing the GBE losses to the wake losses, as well as looking at the array efficiency, behaviour of the GBE spanwise along the front row and peaks in the upstream velocity deficit.
RESULTS: In agreement with previous research on the influence of atmospheric stability on the GBE, this research showed that the GBE had a growing increase under more stable atmospheric conditions. Despite this increase of GBE with atmospheric stability, the relative turbine interaction loss, which includes the wake loss, due to the GBE staying constant with atmospheric stability. Investigating the GBE over different wind speeds led to the conclusion that the GBE is only present in region 2 of the power curve and follows the shape of the Ct curve in that same region. The influence of the farm alignment was key, doubling the impact of the GBE of a staggered farm compared to an aligned farm. With that, a staggered farm also led to an increased influence of the atmospheric stability on the GBE. The array efficiency of the farm decreased with increasing stability, but was concluded not to be a result of the increasing losses of GBE, but rather because of increasing wake losses. Examining the behaviour of the GBE in the lateral direction showed an increase of the GBE towards the centre of the farm. This difference between the edge and centre behaviour of the GBE was found to be strongly increased under a more stable atmosphere. The peak in velocity deficit upstream of the farm due to the GBE increased both in magnitude and in distance to the farm with increasing atmospheric stability, criticizing the industry's assumed upstream distance of X=2.5D of the GBE.
CONCLUSION: More stable atmospheric conditions led to an increased GBE, and with that an increased difference of the GBE between the centre and edge of the farm, an increased influence of the farm alignment on the GBE and an increased occurring distance of the GBE upstream of the farm. The main recommendation for further research is to pursue validation and research on the impact of atmospheric stability on the GBE at existing wind farms.

Abbreviations

ABL Atmospheric Boundary Layer. xi, 5–9, 17, 22, 23

AD Actuator Disk. xi, 18, 21

ASL Atmospheric Surface Layer. 4–7, 9, 10, 18, 21

CFD Computational Fluid Dynamics. 17, 18, 32

D&H Deaves and Harris. xi, 23, 24

DNS Direct Numerical Simulation. 22

DoE Design of Experiments. xiii, 29, 31, 57

FA Free Atmosphere. 5–8, 43

FR First Row. 39

GBE Global Blockage Effect. v, xi–xiii, 2–5, 12–18, 27, 38–41, 43–53, 67

GCS Grid Convergence Study. xiii, 28, 30–32, 63

LCOE Levelized Cost Of Energy. 2

LES Large Eddy Simulation. 4, 17, 41, 52

MOST Monin-Obukhov Similarity Theory. xi, 9–11, 18, 43

RANS Reynolds-averaged Navier–Stokes. v, 4, 17, 18, 20–23, 43

SCADA Supervisory, Control And Data Acquisition. 18

ST Single Turbine. 39, 41

TKE Turbulence Kinetic Energy. 20, 21

Contents

Preface iii

Abstract v

List of Figures xi

List of Tables xiii

1 Introduction 1
- 1.1 Current state offshore wind energy . . . 1
- 1.2 Problem Statement . . . 2
- 1.3 Research questions . . . 3
- 1.4 Outline of thesis . . . 3

2 Physical background 5
- 2.1 Atmospheric Boundary Layer . . . 5
  - 2.1.1 An Atmospheric Boundary Layer Definition . . . 5
  - 2.1.2 Velocity profile . . . 7
  - 2.1.3 Surface roughness . . . 7
  - 2.1.4 Capping inversion . . . 8
- 2.2 Atmospheric Stability . . . 8
  - 2.2.1 An atmospheric stability definition . . . 8
  - 2.2.2 Monin-Obukhov similarity theory . . . 9
  - 2.2.3 Gravity Waves . . . 12
- 2.3 Global Blockage Effect . . . 12
  - 2.3.1 A Wind-farm flow blockage definition . . . 12
  - 2.3.2 Quantification . . . 13
- 2.4 Offshore wind farm . . . 14
  - 2.4.1 Power curve . . . 14
  - 2.4.2 Farm alignment . . . 15
  - 2.4.3 First row behaviour . . . 16

3 Modelling background: ORFEUS 17
- 3.1 ORFEUS . . . 17
- 3.2 Linearised Reynolds Averaged Navier-Stokes . . . 18
  - 3.2.1 Navier-Stokes equations . . . 18
  - 3.2.2 Reynolds decomposition . . . 19
  - 3.2.3 Linearisation . . . 20
  - 3.2.4 Turbine kinetic energy . . . 20
- 3.3 Linearised Actuator Disk theory . . . 21
- 3.4 Spectral Methods . . . 22
  - 3.4.1 A spectral method definition . . . 22
  - 3.4.2 Boundary conditions . . . 22
- 3.5 Incoming boundary layer . . . 23
- 3.6 Fringe Region . . . 24

4 Methodology 27
- 4.1 Theoretical case: 5 by 5 turbine farm . . . 27

4.2 Case verification . . . 28
4.2.1 Setup Upstream reflections study . . . 28
4.2.2 Upstream reflections study results . . . 30
4.2.3 Setup grid convergence study . . . 31
4.2.4 Grid convergence study results . . . 32
4.3 Simulation configuration settings . . . 32
4.3.1 Surface roughness . . . 32
4.3.2 Turbine delta . . . 32
4.3.3 Convergence . . . 33
4.3.4 Ramping value . . . 33
4.3.5 Final simulation configuration . . . 33
4.4 Quantification of GBE . . . 38
4.4.1 Power approach of the GBE . . . 39
4.4.2 Velocity approach of the GBE . . . 40
4.5 Validation . . . 41
4.5.1 Empirical correlation . . . 41
4.5.2 LES study on the GBE . . . 41

5 Results and Discussion **43**
5.1 *Relation between the freestream wind speed and the GBE* . . . 43
5.2 *Farm alignment and power output* . . . 44
5.2.1 Power output . . . 44
5.2.2 Farm alignment . . . 45
5.2.3 Wake losses and GBE losses . . . 47
5.3 *Power and GBE behaviour along the first row* . . . 48
5.4 *Extent and magnitude of upstream velocity loss due to the GBE* . . . 49

6 Conclusions **51**
6.1 Conclusions . . . 51
6.2 Recommendations . . . 53

Appendices **55**
Appendix A - DoE upstream reflections study . . . 57
Appendix B - Upstream reflections study . . . 61
Appendix C - Grid convergence study . . . 63
Appendix D - Atmospheric stability classifications . . . 65
Appendix E - GBE loss results . . . 67

Bibliography **69**

List of Figures

1.1 Change in global surface temperature (annual average) as observed and simulated using human & natural and only natural factors (both 1850-2020) [1] . . . 1
1.2 Annual offshore wind installations by country (left axis) and cumulative capacity (right axis) [2]. . . . 2
1.3 The average size of commercial offshore wind farm projects over the years in Europe [2]. 2
1.4 Quantification of the GBE for 10 different wind farms by four 3^{rd}-party consultants [3] . 3
1.5 Overview of research approach . . . 4

2.1 Atmospheric layers on earth . . . 5
2.2 The ideal gradient of atmospheric variables throughout the Atmospheric Boundary Layer (ABL) . . . 6
2.3 Variation in ABL depth due to convection and pressure difference in regions [4] . . . 7
2.4 Movement of air parcel relative to stable or unstable conditions . . . 8
2.5 Diurnal stability distribution of on-shore wind farm Vindeby (l) and off-shore wind farm Tystofte (r) [5] . . . 9
2.6 Effective velocity correction to the incoming boundary layer following the Monin-Obukhov Similarity Theory (MOST) [6] . . . 10
2.7 Example of a LIDAR system [7] . . . 11
2.8 Example of a 3D Sonic Anemometer (http://www.gillinstruments.com/) . . . 11
2.9 Simulated representation of the GBE. . . . 12
2.10 GBE approach of comparing upstream velocity profiles [8] . . . 13
2.11 Power curve and Ct curve. With (1) = Region 1, (2) = Region 2, (3) = Region 3, (4) = Region 4 . . . 15
2.12 Principle of a lateral aligned alignment in a wind farm [9] . . . 15
2.13 Principle of a staggered alignment in a wind farm [9] . . . 15
2.14 Influence of turbine spacing, thrust coefficient and farm size on the GBE [10] . . . 16

3.1 Wind farm flow model approaches [11] . . . 17
3.2 Schematic of a potential wind development over time [12]. . . . 20
3.3 The geometry of the canopy approach . . . 21
3.4 The geometry of the Actuator Disk (AD) approach . . . 21
3.5 Uniform profile . . . 24
3.6 Logarithmic law profile . . . 24
3.7 Power law profile . . . 24
3.8 Deaves and Harris (D&H) profile . . . 24
3.9 Side view of computational area without fringe region . . . 25
3.10 Side view of the computational area with an effective fringe region . . . 25
3.11 Nordström's visualization of the fringe function [13] . . . 25
3.12 Schlatter's visualization of the fringe function [14] . . . 25

4.1 Overview of theoretical 5 by 5 farm . . . 27
4.2 5 by 5 farm ran on ORFEUS default settings . . . 29
4.3 Colour plot of farm under very stable conditions with pre-verification settings . . . 30
4.4 Colour plot of farm under very stable conditions with post-verification settings . . . 30
4.5 Upstream velocity behaviour pre- and post-verification . . . 31
4.6 The complete computational domain . . . 34

4.7 Variation of frequency of occurrence of atmospheric stability with respect to wind speed at off-shore farm Omø [5] . . . 35
4.8 Velocity profiles for the 5 stability classes in ORFEUS at X = -59D . . . 36
4.9 The normalised power curve of the averaged first row turbine over P_{ref}, where P_{ref} is the theoretical power curve. . . . 36
4.10 The normalised power curve of the averaged first row turbine over P_{ref}, where P_{ref} is the neutral power curve. . . . 36
4.11 The normalised power curve for a single turbine over P_{ref}, where P_{ref} is the neutral power curve. . . . 37
4.12 The normalised power curve for a single turbine over P_{ref}, where P_{ref} is the theoretical power curve. . . . 37
4.13 Velocity profiles for the 5 stability classes in ORFEUS at X = -59D, with $\int U_{verystable} > \int U_{veryunstable}$ in red and $\int U_{verystable} < \int U_{veryunstable}$ in green. . . . 38
4.14 Overview of approaches for quantifying the GBE . . . 39
4.15 Aligned farm layout, in equations referenced to as ”aligned”. . . . 40
4.16 Staggered farm layout, in equations referenced to as ”staggered”. . . . 40
4.17 First row farm layout, in equations referenced to as ”FR”. . . . 40
4.18 Single turbine farm layout, in equations referenced to as ”ST” . . . 40

5.1 U_∞-$L_{aligned}$ . . . 43
5.2 U_∞-$L_{staggered}$ . . . 43
5.3 η_{array} and L_{GBE} over atmospheric stability at U_∞= 8m/s . . . 45
5.4 $L_{FR,aligned}$ over stability for different U_∞. . . . 46
5.5 $L_{FR,staggered}$ over stability for different U_∞. . . . 46
5.6 $L_{ST,aligned}$ over stability for different U_∞. . . . 46
5.7 $L_{ST,staggered}$ over stability for different U_∞. . . . 46
5.8 Distribution of magnitude of GBE losses at the staggered farm compared to the aligned farm. . . . 47
5.9 Wake loss (black) and GBE loss (red) over atmospheric stability at U_∞ = 8 m/s . . . 48
5.10 Loss distribution per atmospheric stability at U_∞ = 8 m/s . . . 48
5.11 L_{GBE} along the first row of a staggered farm . . . 48
5.12 Velocity deficit due to GBE, p_{GBE}, along the first row of a staggered farm . . . 48
5.13 Neutral conditions at U_∞ = 8 m/s . . . 49
5.14 Neutral conditions at U_∞ = 8 m/s . . . 49
5.15 Normalized upstream velocity of the staggered farm at U_∞ = 8 m/s . . . 50
5.16 $p_{staggered}(X)$ at U_∞ = 8 m/s . . . 50

1 Colour plot of farm under stable conditions with pre-verification settings . . . 61
2 Colour plot of farm under stable conditions with post-verification settings . . . 61
3 Colour plot of farm under neutral conditions with pre-verification settings . . . 61
4 Colour plot of farm under neutral conditions with post-verification settings . . . 61
5 Colour plot of farm under unstable conditions with pre-verification settings . . . 62
6 Colour plot of farm under unstable conditions with post-verification settings . . . 62
7 Colour plot of farm under very unstable conditions with pre-verification settings . . . 62
8 Colour plot of farm under very unstable conditions with post-verification settings . . . 62

List of Tables

2.1 Collective table of classifications based on Obukhov length . . . 11
2.2 Collective table of classifications based on stability parameter, ζ . . . 12
2.3 Nomenclature of flow blockage . . . 13

4.1 Turbine Specifications Siemens 2.3 MW MK II [15] . . . 28
4.2 Model parameters studied in the verification process . . . 29
4.3 Model parameters studied in the verification process . . . 30
4.4 Design of Experiments (DoE) for the Grid Convergence Study (GCS) . . . 31
4.5 Ratio edge turbine to centre turbine at fringe intensity 1.1 . . . 32
4.6 Ratio of the edge turbines to the centre turbine at fringe intensity 1.2 . . . 32
4.7 Selected model configuration . . . 34
4.8 Selected stability classification for simulations . . . 35
4.9 Comparing blockage efficiency with J. Strickland's LES study . . . 42

5.1 Power output (U_∞ = 8 m/s), η_{array} (U_∞ = 8 m/s) and averaged (U_∞ = 5 to 9 m/s) GBE loss for the aligned farm . . . 45
5.2 Power output (U_∞ = 8 m/s), η_{array} (U_∞ = 8 m/s) and averaged (U_∞ = 5 to 9 m/s) GBE loss for the staggered farm . . . 45
5.3 Peaks of $p_{staggered}(X)$ in upstream velocity . . . 50

1 Simulation configuration extending the fringe length (with a constant fringe start) . . . 57
2 Simulation configuration extending the start of the fringe region (with a constant fringe length) . . . 57
3 Simulation configuration extending start fringe region (i.e. a constant fringe ending) . . . 57
4 Simulation configuration extending the fringe intensity . . . 58
5 Simulation configuration extending the domain start . . . 58
6 Simulation configuration extending the spanwise domain . . . 58
7 Simulation configuration extending the vertical domain . . . 58
8 Simulation configuration extending the turbine delta parameter . . . 58
9 Simulation configuration extending Nz . . . 59
10 Simulation configuration extending Nx and Ny . . . 59
11 Simulation configuration extending the surface roughness (not computational) . . . 59

12 Absolute results convergence study at fringe intensity 1.1 . . . 63
13 Absolute results convergence study at fringe intensity 1.2 . . . 63
14 Normalised results over theoretical power from power curve of convergence study at fringe intensity 1.1 . . . 64
15 Normalised results over theoretical power from power curve of convergence study at fringe intensity 1.2 . . . 64

16 Stability Classification [A. van Wijk (1988) [16], J.P. Coelingh (1996) [17], M. Motta (2005) [5], Andrea Venora (2009) [18]] . . . 65
17 Stability Classification [Maarten Holtslag] (2016) [19] . . . 65
18 Stability Classification [Sven Erik Gryning (2007) [20], A. Peña (2008) [21]], A. Sathe (2011) [22], R. Barthelmie (2015) [23] . . . 65
19 Stability Classification [Sorbjan and Grachev][24], z = 40 m . . . 66

20 Stability Classification [Sanz Rodrigo] [25], z = 80 m 66
21 Stability Classification [Peña] [26], z = 15 m 66

22 Power losses (%) due to the GBE of the aligned farm calculated through the FR approach 67
23 Power losses (%) due to the GBE of the staggered farm calculated through the FR approach 67
24 Power losses (%) due to the GBE of the aligned farm calculated through the ST approach 67
25 Power losses (%) due to the GBE of the staggered farm calculated through the ST approach 67

1

Introduction

1.1. Current state offshore wind energy

There is a general growing interest in renewable energy. Countries all over the world are joining in agreements to meet certain levels of production of renewable energy [27, 28] with the objective of putting a hold on the rise of temperature demonstrated by the IPCC [1], shown in Figure 1.1.

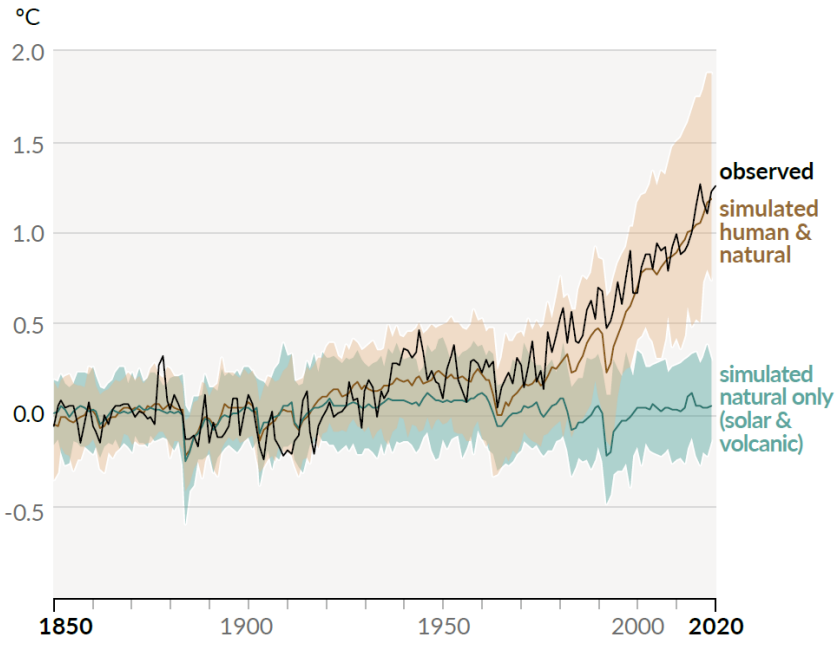

Figure 1.1: Change in global surface temperature (annual average) as observed and simulated using human & natural and only natural factors (both 1850-2020) [1]

Hydropower, which accounts for 60% of all renewable energy [29], wind energy and solar energy are the main carriers of renewable energy. Together they provide about 90% of all generated renewable electricity [29]. Out of these three sources, wind and solar have the highest growth potential and are expected to occupy two-thirds of the renewables' growth in 2021 [30]. COVID-19 restrictions might have had a negative effect on 2020's completed wind energy capacity installation in Europe [2]. Nevertheless, the cumulative installed capacity of offshore grid-connected wind farms keeps showing steady growth as can be seen in Figure 1.2. On top of that, last year's record of €26.3bn [2] raised in Europe for the financing of new offshore wind farms shows that offshore wind plays a substantial role in the energy transition.

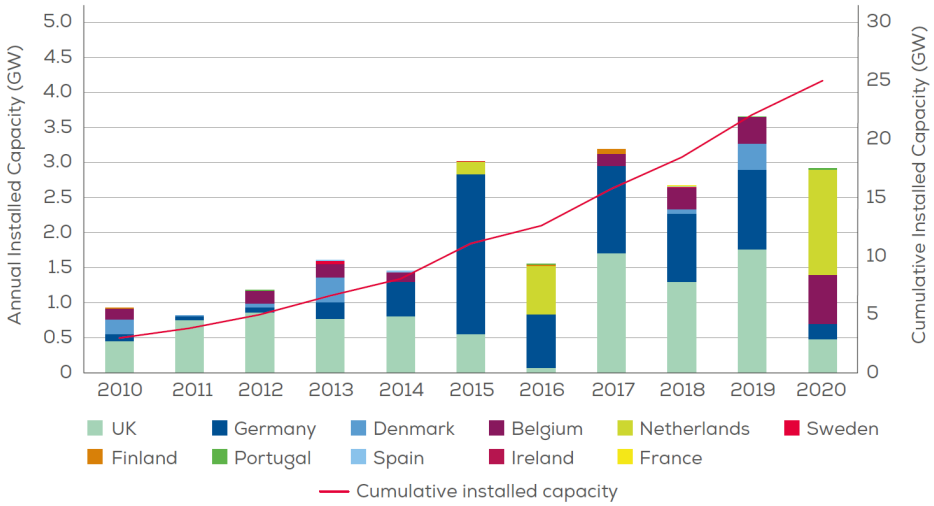

Figure 1.2: Annual offshore wind installations by country (left axis) and cumulative capacity (right axis) [2].

According to IRENA [31], to achieve the Paris Agreement, from 2015 35 % of the total electricity produced should come from on- and off-shore wind. With that the Levelized Cost Of Energy (LCOE) for offshore wind energy would drop from 0.13 USD/kWh in 2018 to 0.05-0.09 USD/kWh in 2030 and ultimately 0.03-0.07 USD/kWh in 2050 [31]. Figure 1.3 shows that the average wind farm size has been growing over the past years. In 2020, final investment decisions were made to install two "mammoth" offshore wind farms in the North Sea, namely the 1.5 GW Hollandse Kust Zuid wind farm and the 2.4 GW Dogger Bank A and B [2].

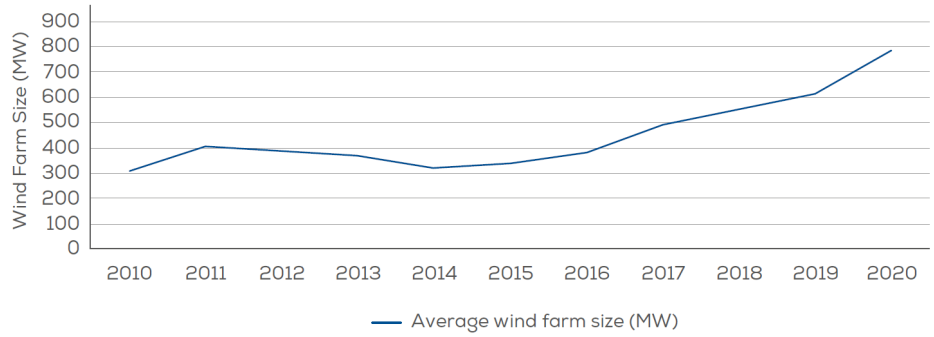

Figure 1.3: The average size of commercial offshore wind farm projects over the years in Europe [2].

1.2. Problem Statement

An effect that scales with the size of wind farms is the so-called Global Blockage Effect (GBE) [32, 33]. This is the phenomenon where the incoming boundary layer flow, upwind of the wind farm is slowed down because the wind turbines act as one large flow obstacle. For investors of new wind farms, the energy yield and the thereby associated array efficiency are crucial. Accurate prediction and modelling of that energy yield is of importance. Most array efficiency assessments are normalized by the production of the first row of the wind farm [34]. By normalizing over the first row, the false assumption is made that all turbine interactions are taken into account, while in fact the GBE is neglected [35]. Because of the normalization of downstream rows by the first row, overestimating the first row production leads to an overprediction of all rows downstream as well. Over the last years, there has been an increasing amount of research on the GBE [36], and it safe to assume that the GBE is not to be neglected in wind farm assessments. More and more renewable energy consultants

take the GBE into account in their models. Figure 1.4 shows the quantification of the GBE in 10 different wind farms by four 3^{rd}-party consultants. One can observe from this Figure that the GBE has a negative effect on the array efficiency of a farm, but also that the magnitude of the GBE differs considerably per consultant. Several academic papers and presentations from the wind industry emphasise the influence of atmospheric stability on the GBE, and while not including this topic, recommend that further research should be carried out [37, 38, 39, 40, 41]. This gap in research regarding the influence of atmospheric stability on the GBE will be the main focus of this thesis project.

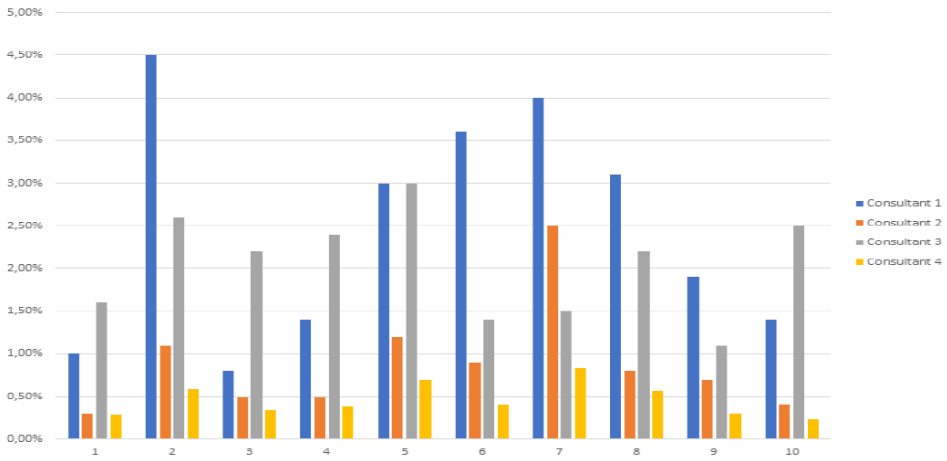

Figure 1.4: Quantification of the GBE for 10 different wind farms by four 3^{rd}-party consultants [3]

Industry presentations emphasize that further research on parameters that could influence the GBE is needed. Therefore, this thesis not only focuses on atmospheric stability as a parameter but also includes other parameters that could influence the relation between atmospheric stability and the GBE. An overview of these parameters is given later in this chapter in Section 1.4.

This thesis research is set up to quantify the influence of atmospheric stability on the GBE of offshore wind farm flows, thereby aiming to improve the accuracy of energy yield calculations and predictions of offshore wind farms.

1.3. Research questions

The following main research question of this thesis is stated, aimed to solve the problem stated in Section 1.2:

"How does atmospheric stability affect the global blockage effect?"

This main research question will be tackled by finding the influence of atmospheric stability on the following aspects:

- *"Relation between the freestream wind speed and the GBE"*
- *"Farm alignment and power output"*
- *"Power and GBE behaviour along the first row"*
- *"Extent and magnitude of upstream velocity loss due to the GBE"*

1.4. Outline of thesis

The flow chart shown in Figure 1.5 gives an overview of the factors that influence the GBE. The main research question is set up to find the influence of atmospheric stability on the GBE, which is coloured in blue in Figure 1.5. The sub-questions, coloured green in Figure 1.5, are all set up around the relation

between atmospheric stability and GBE and aim to expand the knowledge of the behaviour of the GBE under different atmospheric conditions. As shown in the legend of Figure 1.5 the influence of every sub-research field on the impact of atmospheric stability on the GBE will be investigated.

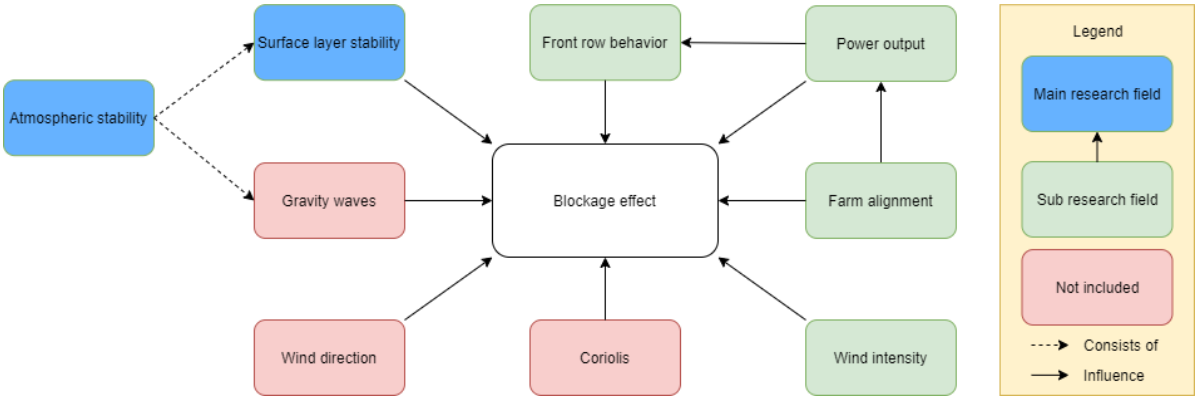

Figure 1.5: Overview of research approach

Atmospheric stability is an indicator for a flow to maintain or become turbulent [4]. Atmospheric stability influences both the velocity profile as well as the wake recovery [42]. A gravity wave is a wave moving in a fluid due to a restoring force of a vertically displaced flow [43] and is related to atmospheric stability as the atmospheric stability dictates the opportunity of vertical displacement of air parcels.

Turbines are located partly in the lower layer, the Atmospheric Surface Layer (ASL), and partly in the Ekman layer. Atmospheric stability is present in the entire atmosphere, but in the ASL, the atmospheric stability is dominated by the surface roughness and the Obukhov length and is commonly expressed through the Monin-Obukhov similarity theory. Since the introduction of this theory by A. S. Monin and A. M. Obukhov in 1954 [44] the theory has been favoured not only for modelling within, but also above the ASL. As Figure 1.5 shows, this thesis project only involves the influence of the atmospheric stability through the surface layer stability, or rather through the Monin-Obukhov similarity theory.

Sub-research questions which are included in this thesis are the wind intensity, farm alignment, power output and first row behaviour of a farm. In which with the wind intensity is meant the freestream wind upstream of the farm. The first row behaviour of the wind farm is impacted by the power output of the farm, which in its turn is impacted by the farm alignment. This thesis aims to distinguish and quantify the effects on the GBE of all these 4 sub-research fields.

Gravity waves, wind direction and Coriolis forces can all influence the extent of the GBE, but are not included in this thesis. For this thesis project, the linearised RANS model ORFEUS will be used to facilitate a large number of simulations and data analyses. Gravity waves are usually investigated using more detailed and extensive Large Eddy Simulation (LES) models [45] and are therefore not included in the scope of this thesis. Coriolis effects are not in the scope of this thesis project as they were not present in the version of ORFEUS at the time of the research. This thesis investigates the general effects regarding the GBE and is therefore not site-specific. Wind direction was believed to be too site-specific and was therefore not involved.

This report is structured as follows. The thesis starts with providing the relevant physical background and background about wind farm modelling in Chapters 2 and 3 respectively. Chapter 4 then explains how the research questions will be tackled. The results will be presented and discussed in Chapter 5. Finally, Chapter 6 presents the conclusions and recommendations.

2

Physical background

This chapter offers background theory about the physical phenomena related to the Global Blockage Effect (GBE) and atmospheric stability. The chapter starts by explaining the basics of the Atmospheric Boundary Layer (ABL) in Section 2.1. Section 2.2 introduces background about the atmospheric stability. Lastly, Section 2.3 elaborates on the GBE.

2.1. Atmospheric Boundary Layer

2.1.1. An Atmospheric Boundary Layer Definition

This Subsection elaborates on the ABL and the main layers of Earth's atmosphere. Figure 2.1 schematically illustrates, not true to scale, the main layers of Earth's atmosphere. All relevant theory for wind turbines involves the bottom layer, the troposphere. The troposphere itself can be subdivided into the Atmospheric Surface Layer (ASL) (Prandtl-layer, constant flux layer), the Ekman layer and the free troposphere. The ASL and the Ekman layer collectively form the atmospheric boundary layer ABL [46]. The ASL accords to the lower 10% of the ABL [4], which approximately represents the lower 100 m of the atmosphere [47]. The lower boundary for the ABL is the microlayer, while the upper boundary for the ABL is the capping inversion. The capping inversion is the thin layer between the ABL and the Free Atmosphere (FA) and is further detailed in Subsection 2.1.4.

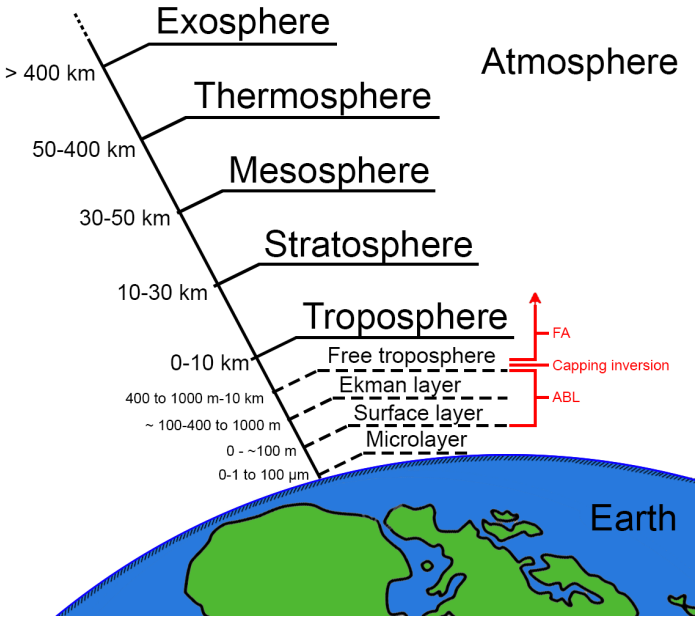

Figure 2.1: Atmospheric layers on earth

The ABL is the part of the troposphere which is influenced directly by the earth's surface within the time scale of about an hour or less [48]. In the ABL, atmosphere variables convert from surface values to FA characteristics [49]. Figure 2.2 shows a plot of the ideal ABL, in which there is a linear transition from the surface values to the FA values. At the surface the wind speed, U_s is considered 0. At the top of the boundary, the wind speed is considered to be equal to the Geostrophic wind, G. In reality, the velocity profile does not increase linearly from zero at the surface to the ABL height value, which is further explained in Section 2.1.2.

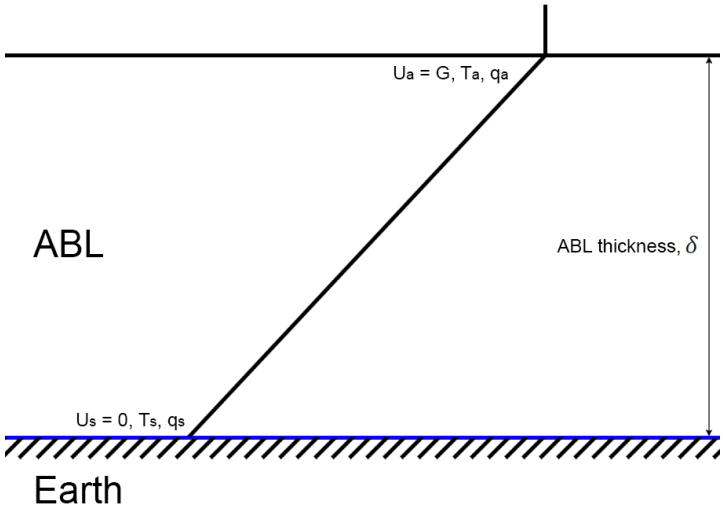

Figure 2.2: The ideal gradient of atmospheric variables throughout the ABL

The lowest layer which can be defined is a thin layer of centimetres high called the microlayer (interfacial layer) [4]. Offshore, the microlayer is called sea surface microlayer and is typically 1 to 100 μm thick [50]. In this layer, the molecular transport is dominating over turbulent transport, where a high virtual potential temperature gradient exists between the hot earth surface and the warm lower boundary of the ASL [4, 49].

The depth of the ABL, δ, ranges from tens of metres up to 4km [46] and is mainly influenced by vertical motion on synoptic and mesoscale. Furthermore, the depth of the ABL is thinner in higher pressure regions compared to lower pressure regions [4]. Figure 2.3 shows the difference in ABL depth due to the difference in pressure and displacement to high altitudes due to convection.

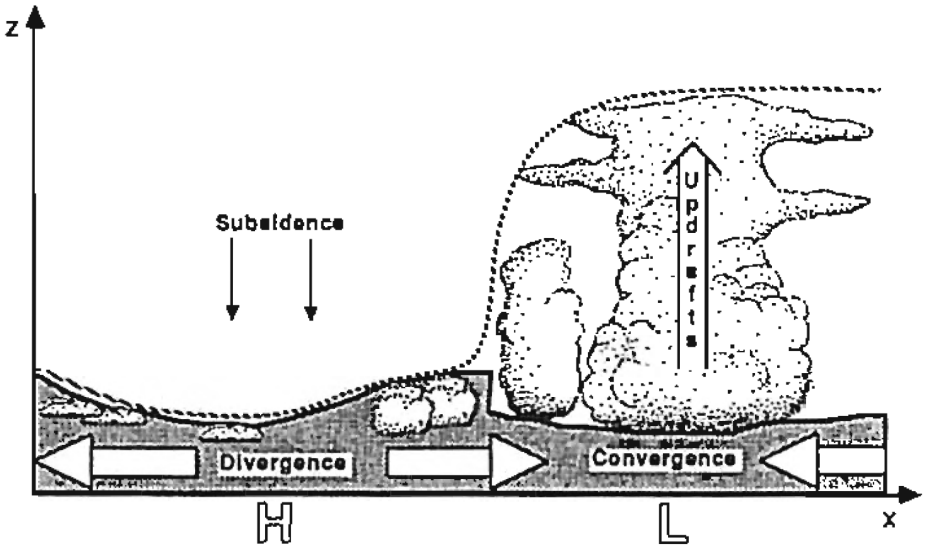

Figure 2.3: Variation in ABL depth due to convection and pressure difference in regions [4]

Over the years, the hub height of offshore turbines has increased and currently is typically above the ASL, meaning that the turbine rotor reaches in both the ASL and the Ekman layer [51]. This makes the turbine interaction with the lower atmosphere more complicated. Although the wind turbines do not reach the FA, the layer still plays a role as it interferes with the wind and stability in and around the wind farm [52]. A more stable FA leads to lower ABL height and thus a decreased array efficiency [52]. The upcoming Subsection 2.1.2 elaborates the influence of the layers on the velocity profile.

2.1.2. Velocity profile

The incoming boundary layer has multiple characteristics which can be expressed in the vertical direction. One of these characteristics which can be described vertically is the wind velocity, called the velocity profile (wind profile). The surface roughness, z_0, friction velocity, u^* and atmospheric stability dominate the velocity profile in the ASL [20]. Where z_0 is defined by the roughness on the surface. The friction velocity can be considered constant in the ASL. Atmospheric stability is dominated by temperature gradients [53]. At the bottom of the ABL, the velocity profile is 0, while at the top the velocity profile equals the geostrophic wind. Section 3.5 elaborates on the ways of modelling the velocity profile.

2.1.3. Surface roughness

Surface roughness, z_0, is considered the height at which the logarithmic wind profile extrapolates, towards the surface, to 0 m/s [48]. A higher surface roughness leads to more intense turbulence for the wind passing the roughness element [4, 48]. Vice versa, a perfectly smooth surface has a surface roughness of 0 m.

The surface roughness is strongly dependent on the waves and sea state [54]. Stronger winds lead to higher waves, which increases the surface roughness. Charnock's equation relates the surface roughness to the incoming boundary layer, as shown in Equation 2.1. As the atmospheric stability impacts the shear of the incoming boundary layer, the surface roughness is influenced by the atmospheric stability.

$$z_0 = \alpha_c \frac{u_*^2}{g} \tag{2.1}$$

Where α_c is the Charnock's parameter (-), u_* is the friction velocity (m/s) and g the gravitational acceleration (m/s^2).

2.1.4. Capping inversion

The capping inversion is a strong stable layer within the troposphere between the ABL and the FA. This stable layer prevents the FA from being influenced by the surface friction [51], it caps the turbulence caused by heat convection in the ABL. The height of the capping inversion (inversion height) varies with the depth of the ABL. D. Allaerts [55] showed that the inversion height has a high influence on the performance of offshore wind farms, showing a decrease in performance of 31% when increasing the inversion height from 500 m to 1500 m.

The flow above the capping inversion is non-turbulent and shear free [45] and is perpendicular to the pressure gradient and the Coriolis force. In some cases, in low-pressure regions, it is hard to define a capping inversion/top of the ABL due to the upward motions of boundary layer air to high altitudes in the troposphere.

2.2. Atmospheric Stability

2.2.1. An atmospheric stability definition

One can distinguish three states of atmospheric stability: stable, unstable and neutral conditions. The atmosphere is stable when a displaced parcel tends to return to its original height after being displaced vertically. A stable ABL mainly occurs during nighttime when the lower surface is cold. The atmosphere is unstable when the vertically displaced parcel further accelerates in its direction of displacement. An unstable ABL mainly comes with warm surfaces during the day. The atmosphere is neutral when parcels neither accelerate or decelerate after being displaced. [48]

The dashed line in Figure 2.4 shows the change in potential temperature and altitude of a displaced parcel. Potential temperature, θ, is the temperature that an air parcel would have if moved adiabatically to standard pressure, p_0 . The right bold line represents the atmospheric behaviour when stable, while the left bold line represents the atmospheric behaviour when unstable. As the air parcels move differently depending on the stability, the wind speed profile also assumes different shapes. [18]

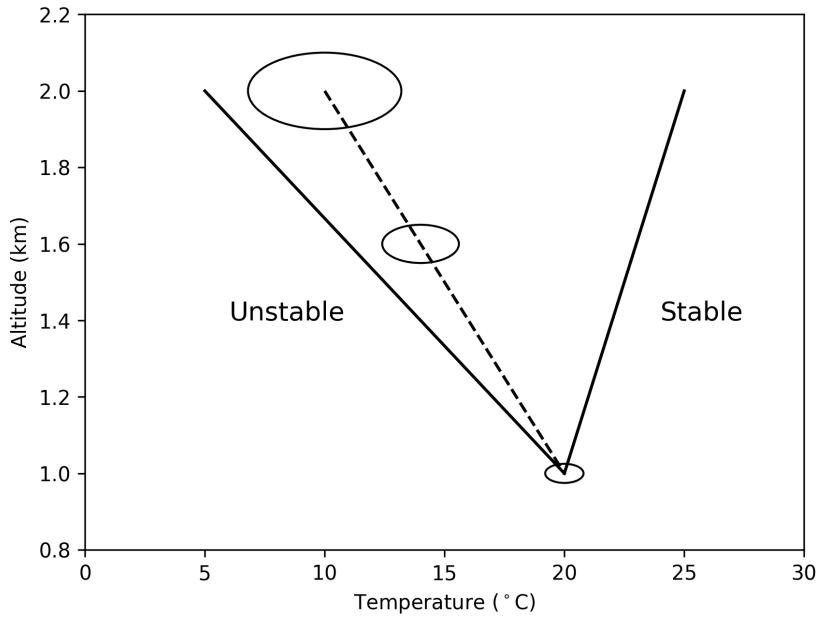

Figure 2.4: Movement of air parcel relative to stable or unstable conditions

The diurnal alteration of stability is typically noticeable onshore as the earth surface tends to cool and warm easily. Offshore, however, the surface water is less sensitive to diurnal temperature changes due to the high heat capacity of water and a large amount of mixing within the top water layer of the

sea. Because of the slow varying sea surface temperature, the diurnal stability change pattern is less present or even non-existent. In general, offshore wind is more uniform and stable due to homogeneous conditions [56] [4]. Figure 2.5 shows the difference between onshore and offshore diurnal stability conditions.

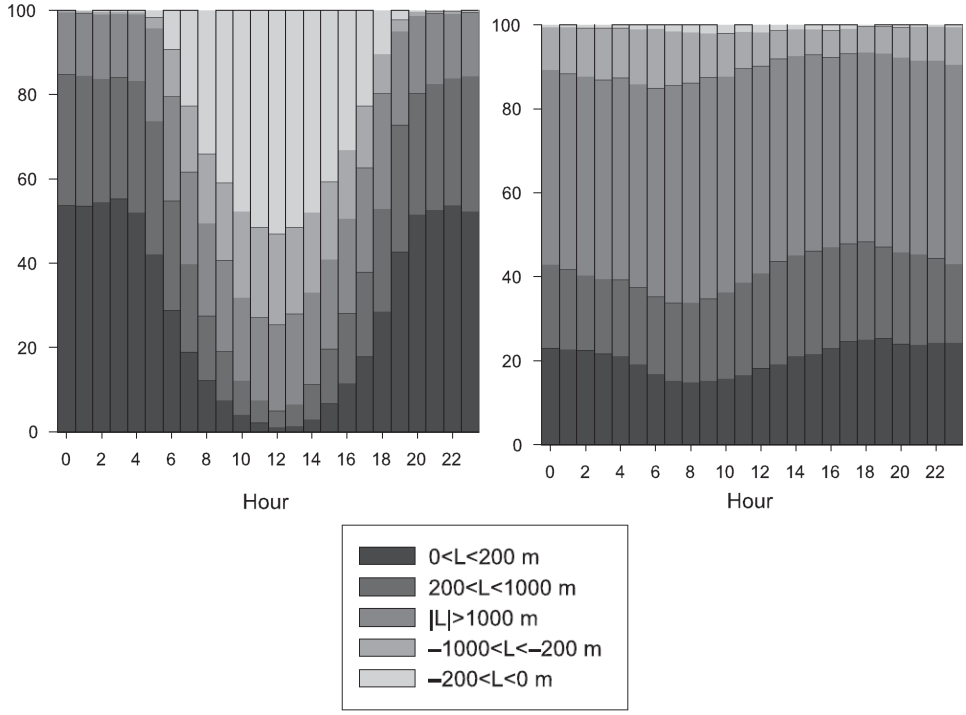

Figure 2.5: Diurnal stability distribution of on-shore wind farm Vindeby (l) and off-shore wind farm Tystofte (r) [5]

The atmospheric stability of the ABL affects both turbine performance and the structure and dynamics of turbine wake flows. For a standalone turbine, the influence of the atmospheric stability is mainly effective through the change in shear and turbulence of the incoming boundary layer [32]. The more stable the atmospheric conditions, the higher the shear and the weaker the turbulence. Vice versa, the more unstable the atmospheric stability the lower the shear and the stronger the turbulence. More unstable conditions lead to faster wake recovery, due to enhanced mixing processes of the airflow [42].

2.2.2. Monin-Obukhov similarity theory

Monin-Obukhov Similarity Theory (MOST) is a method used to describe wind shear in the ASL and can be seen as a correction to the neutral wind profile due to stratification [57]. It was developed by A. S. Monin and A. M. Obukhov in 1954 [44]. According to the duo, the atmospheric stability in the surface layer is influenced by three factors: g/T_0, u^* and $q/(c_p\rho)$. Where g is the gravitational acceleration (m/s^2), T_0 is the surface temperature, u^* is the friction velocity (m/s), q is the kinematic heat flux (Km/s), c_p is the specific heat $(J/K/Kg)$ and ρ is the air density (kg/m^3). They assumed that with a single parameter, the Obukhov Length, L, the atmospheric turbulence in the surface layer could be described. L is the height from which the turbulence is dominated by buoyancy rather than by mechanical effects like shear and friction [51]

$$L = -\frac{u_*^3 T_0}{\kappa g(\overline{w'\theta_v'})_s} = -\frac{u_*^3}{\kappa \frac{g}{T_0}(\overline{w'\theta_v'})_s} \tag{2.2}$$

Where $(\overline{w'\theta_v'})_s$ is the kinematic heat flux at the surface. Herein u_* is defined as

$$u_* = \sqrt{\frac{\tau}{\rho}} \tag{2.3}$$

where τ is the surface shear stress (Pa). In the ASL, both $(\overline{w'\theta_v'})_s$ and τ are assumed to be vertically constant [44]. Using the Obukhov length, the atmospheric stability corrected wind profile based on MOST can be constructed as follows:

The non-dimensional wind stability correction, ψ_m, depends on the stability and is given with Equation 2.4:

$$\psi_m = \begin{cases} 1 + 5\frac{z}{L} & ,stable \\ (1 - 16\frac{z}{L})^{-\frac{1}{4}} & ,unstable \end{cases} \tag{2.4}$$

Using ψ_m, the final stability-corrected velocity profile under stable conditions is then obtained in Equation 2.5.

$$\begin{aligned} \frac{dU}{dz} &= \frac{u_*}{kz}\psi_m(\frac{z}{L}), \\ U &= \frac{u_*}{\kappa} \cdot \int^z \frac{\psi_m(\frac{z}{L})}{z} dz, \\ U &= \frac{u_*}{\kappa} \cdot \left[\ln z + \frac{5}{L}z\right]_{z_0}^{z} \end{aligned} \tag{2.5}$$

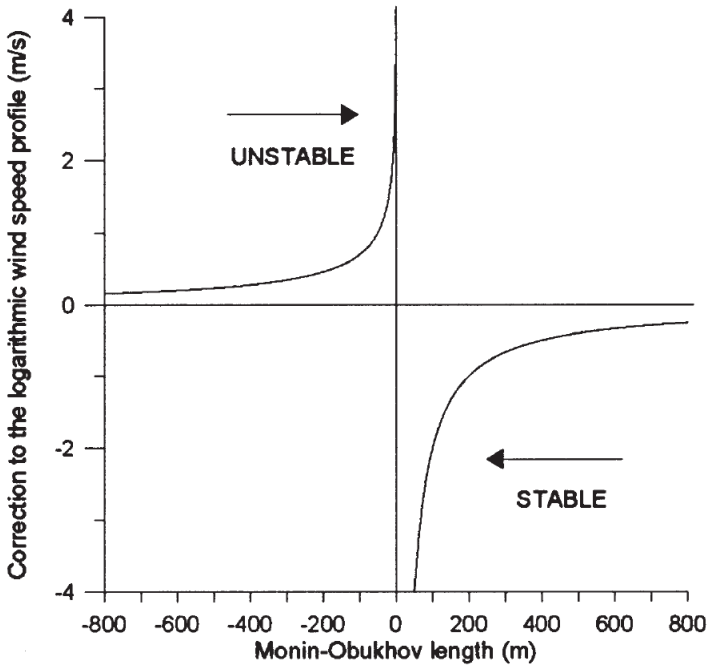

Figure 2.6: Effective velocity correction to the incoming boundary layer following the MOST [6]

Figure 2.6 plots the velocity correction because of the MOST. A negative L describes unstable air. A positive L describes stable air and L = ∞ and L = -∞ describes neutral air. MOST is only applicable in horizontally homogeneous surfaces and quasi-stationary conditions. The Obukhov length can be

estimated with wind speed and temperature measurements at two different heights, through the Richardson number, R_i or through the bulk Richardson number, Ri_b [58]. The data needed to estimate the Obukhov length is commonly measured with scanning LIDAR [59], shown in Figure 2.7 or a Sonic 3D anemometer, shown in Figure 2.8.

Figure 2.7: Example of a LIDAR system [7]

Figure 2.8: Example of a 3D Sonic Anemometer (http://www.gillinstruments.com/)

The Obukhov length is not the only parameter to classify atmospheric stability. From Buckingham's PI-theorem the dimensionless stability parameter (MOST parameter), $\zeta = z/L$ was founded, where z is the height and L is the Obukhov Length. It is unknown whether Lettau found this stability parameter independently of Obukhov [60]. A distinction between the stable, unstable and neutral air can be made based on the dimensionless parameter z/L [4]:

$$\begin{aligned} \frac{z}{L} > 0 \quad & \text{stable} \\ \frac{z}{L} < 0 \quad & \text{unstable} \\ \frac{z}{L} = 0 \quad & \text{neutral} \end{aligned} \tag{2.6}$$

Tables 2.1 and 2.2 summarize the different stability classifications used in previous research study's.

Table 2.1: Collective table of classifications based on Obukhov length

Stability Class	[16], [17], [5], [18]	[19]	[20], [21],[22], [23]
Very stable	0 <L <200 m	0 <L ≤ 80 m	10 <L <50 m
Stable	200 <L <1000 m	80 <L ≤ 480 m	50 <L <200 m
Neutral		480 ≤ L or L ≤ -80 m	|L| >500 m
Near-neutral	|L| >1000 m		−500 <L <−200 m
Unstable	-1000 <L <-200 m	-80 ≤ L <-20 m	-200 <L <-100 m
Very unstable	-200 <L <0 m	-20 ≤ L <0 m	-100 <L <−50 m

Table 2.2: Collective table of classifications based on stability parameter, ζ

Stability Class	z = 40 m, [24]	z = 80 m, [25]	z = 15 m, [26]
Extremely stable	ζ >50	ζ >2	
Very stable	0.6 < ζ <50	0.6 < ζ <2	
Stable		0.2 < ζ <0.6	0.03 < ζ < 3
Slightly stable	0.02 < ζ <0.6	0.02 < ζ <0.2	
Neutral			$\lvert\zeta\rvert$ < 0.03
Near-neutral	0 < ζ <0.02	0 < ζ <0.02	
Unstable			-0.2 < ζ < -0.03
Very unstable			-1.5 < ζ < -0.2

2.2.3. Gravity Waves

Following up on the explanation in Section 2.1.1 about the displacement of air parcels under different stability scenario's, one can unravel another phenomenon, namely, gravity waves. The returning of the parcels to their equilibrium state happens in an oscillatory manner, which creates a wave called a gravity (buoyancy) wave. There are different optional sources for the vertical displacement of air parcels: forced convection, mountain relief, frontal regions, jet-stream flow or perturbations associated with the geostrophic wind, G [48]. In the case of an offshore wind farm the wind is displaced upward due to the blocking farm, creating gravity waves in that way [45]

2.3. Global Blockage Effect

2.3.1. A Wind-farm flow blockage definition

Flow blockage is the effect where the incoming wind speed is reduced and deflected upwards and sideways due to mass conservation of wind turbines [32]. There are two types of flow blockage: local and global flow blockage. Local flow blockage occurs in front of every operating turbine, independent of the setup it is based in. When multiple turbines are located together in a farm or cluster, they create a collective flow blockage called the Global Blockage Effect (GBE). The red dotted square in Figure 2.9 shows this phenomenon, where one can clearly see the incoming wind slowing down gradually in front of the wind farm. The GBE causes a small reduction in upstream velocity, but as the power production of a turbine below the rated wind speed scales with the incoming velocity to the third power, the total power loss in a wind farm can be in the size of percentages.

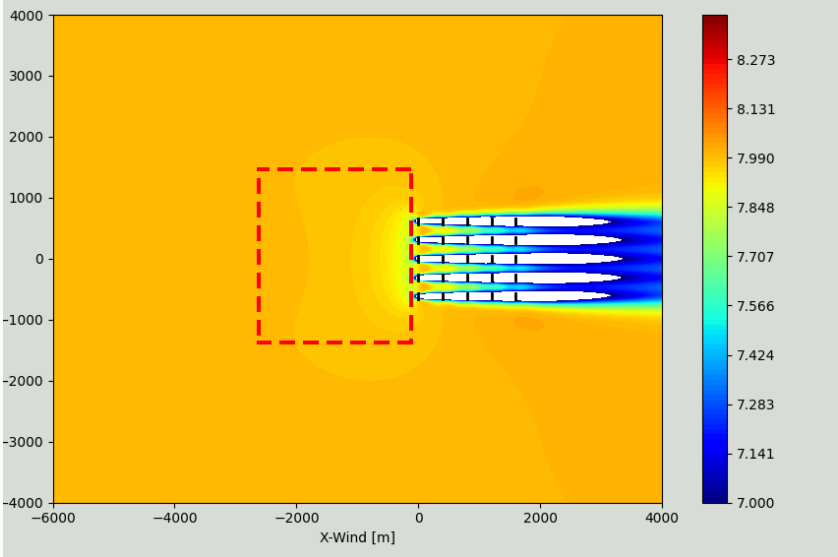

Figure 2.9: Simulated representation of the GBE.

Alternate ways of naming for a phenomenon happens frequently in science, and so is the case for the phenomenon flow blockage. Therefore, Table 2.3 gives an overview of the range of names for both local and global flow blockage. For the sake of consistency, for the continuation of this thesis, the term Global Blockage Effect (GBE) will be used.

Table 2.3: Nomenclature of flow blockage

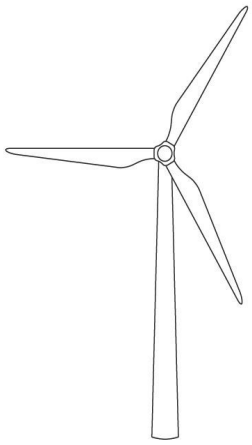	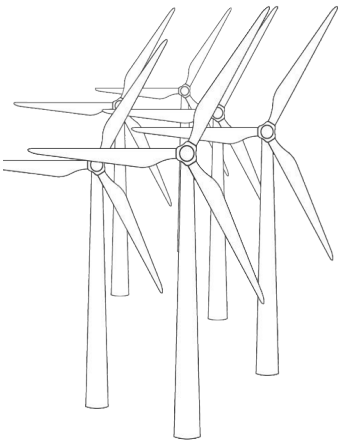
Local blockage effect [61] Turbine induction zone [62]	Global Blockage Effect (GBE) [59] Wind-farm-scale blockage [35] Cumulative turbine induction [35] Wind-farm induction zone [32] Compression zone [63] Two-scale blockage [64]

2.3.2. Quantification

A consequent approach to quantifying the GBE effect is essential. In the current research state, there are two main ways of quantifying the GBE, either by looking at the upstream velocity loss, like D. Medici does as shown in Figure 2.10, or by comparing the power performances of the turbines.

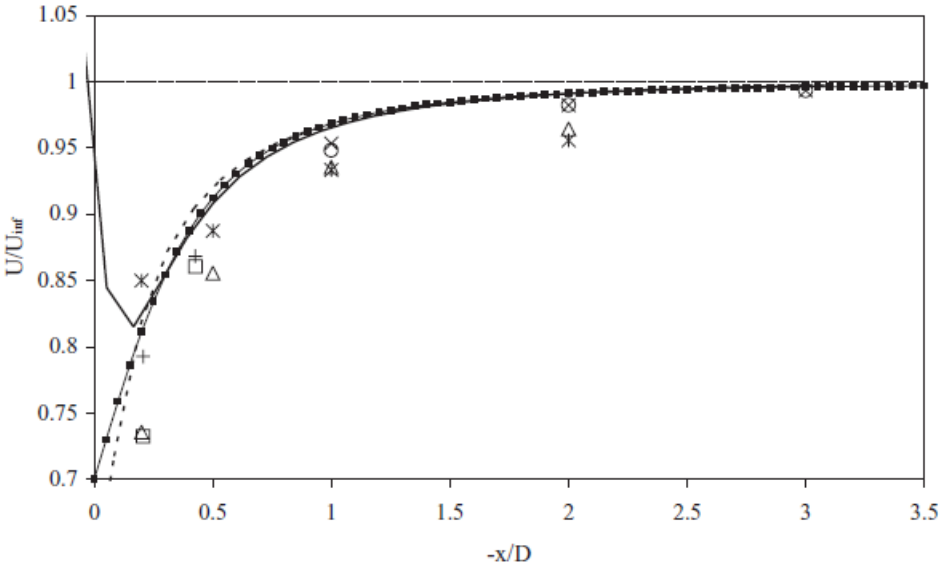

Figure 2.10: GBE approach of comparing upstream velocity profiles [8]

It is safe to say that the industry norm for the upstream distance of quantifying the GBE is 2.5D [32]. One can not compare quantified results of the velocity approach with results of the power approach, as produced power scales to the third with velocity. A relative decrease in velocity due to the GBE leads to a larger relative decrease in power. The GBE is not always expressed as a loss, A. Sebastiani [65] for example, expresses the GBE as the efficiency of the turbine based on the centre rotor wind speed, as Equation 2.7 shows.

$$\eta_b(\Phi) = \frac{P_{ref}}{P_\infty} \tag{2.7}$$

T. Nishino [61] has yet another approach, as he expresses the GBE by comparing the power coefficient values, C_p.

A. Sebastiani states in his research that the correct approach for quantifying the GBE in modelling is by comparing the incoming wind of a fully operating farm to that of an isolated upstream row of turbines [65]. The GBE can then be expressed as an efficiency factor shown in equation 2.8:

$$\eta_b(\Phi) = \frac{\sum_{i=1}^{n(\Phi)} [U_{da_i}(\Phi)]^3}{\sum_{i=1}^{n(\Phi)} [U_{df_i}(\Phi)]^3} \tag{2.8}$$

where, $n(\Phi)$ is the number of turbines in the upstream row (-), Φ is the wind direction (□), $U_{da_i}(\Phi)$ is the wind speed in a fully operating wind farm (m/s) and $U_{df_i}(\Phi)$ is the wind speed in an isolated first row only (m/s).

DNV has a similar approach as A. Sebastiani, but rather aims to reach a correction factor for a total turbine interaction efficiency which is split into a wakes-only factor and a GBE factor, as defined in Equation 2.9.

$$\eta_{totalturbineinteraction} = \frac{\sum_{All} P_{i,wf}}{\sum_{All} P_{i,I}} = \eta_{bl} \cdot \eta_{wakesonly} \tag{2.9}$$

where $P_{i,wf}$ is the power from the turbine (kW) i when the entire wind farm is operating. $P_{i,I}$ is the power from turbine i operating in isolation (kW). η_{bl} is the GBE efficiency (-), and $\eta_{wakesonly}$ is the wake efficiency (-). Here, $\eta_{totalturbineinteraction}$ can be seen as the array efficiency and consists of the turbine interaction losses, which are considered to be wake losses and losses due to the GBE.

2.4. Offshore wind farm

2.4.1. Power curve

A power curve plots the potential power production of a single turbine over incoming freestream velocity, U_∞. Usually, the turbine manufacturer delivers the power curve constructed from wind speed measurements 2.5D upstream of the turbine, following the IEC protocol [66].

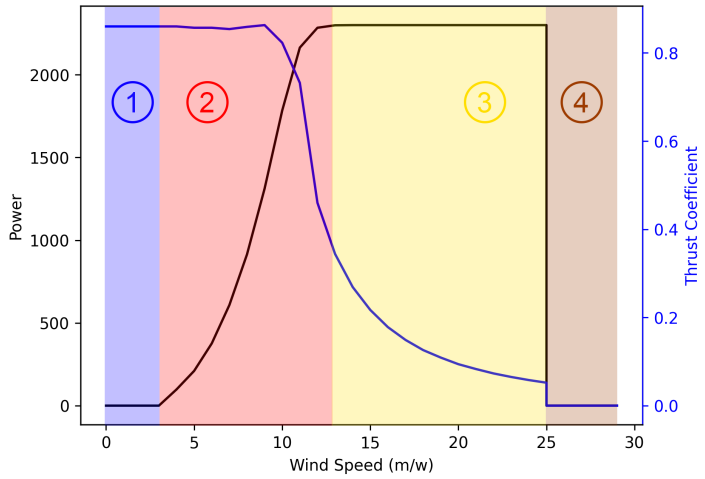

Figure 2.11: Power curve and Ct curve. With (1) = Region 1, (2) = Region 2, (3) = Region 3, (4) = Region 4

Figure 2.11 shows the power curve and the Ct curve of the Siemens 2.3 MW MK II turbine. The power curve can be divided into four operating regions, which are also shown in Figure 2.11. Region 1 is the region belonging to wind speeds lower than the cut-in speed, in which the turbine does not generate power. Region 2 is the region in which the turbine produces power up to its nominal power production, P_{rated}. Region 3 is often called the full load region [67] and reaches from the rated wind speed to the cut-out speed. In Region 3, the turbine produces at its rated power. Region 4 belongs to wind speeds over the cut-out speed. In region 4, the turbine does not generate any power.

2.4.2. Farm alignment

There are endless possible formations of turbines in a wind farm, two common ways of aligning turbines in a farm relative to the incoming wind direction can be distinguished. The first alignment is a non-staggered alignment (purely longitudinal alignment, perfectly aligned), where the wind turbines are aligned rows in the direction of the incoming wind, as shown in Figure 2.12. The second alignment is a staggered alignment, where the farm rows are under an angle with regard to the incoming wind, in such a way that the turbines alternate with respect to the wind, as visualised in Figure 2.13.

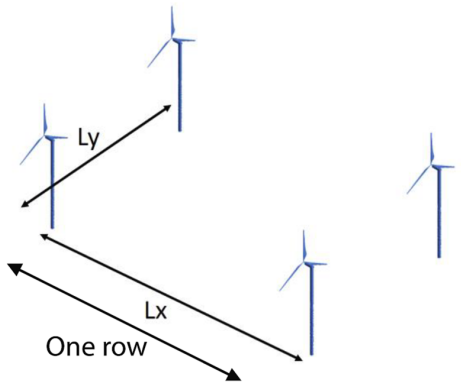

Figure 2.12: Principle of a lateral aligned alignment in a wind farm [9]

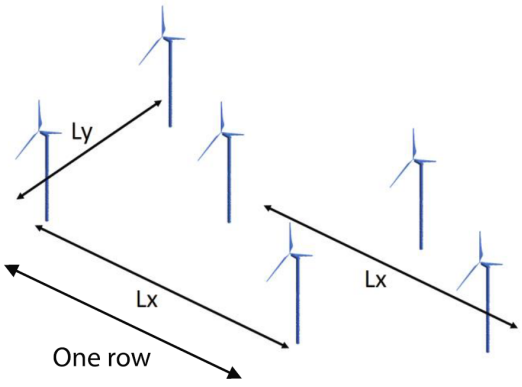

Figure 2.13: Principle of a staggered alignment in a wind farm [9]

Different turbine alignment and turbine spacing lead to different power extractions from the incoming wind, as R. Stevens showed [68]. J. Strickland studied the influence of turbine alignment and turbine spacing on the GBE [36]. Figure 2.14 concludes that both turbine spacing, thrust coefficient and farm size are of influence on the size of the GBE.

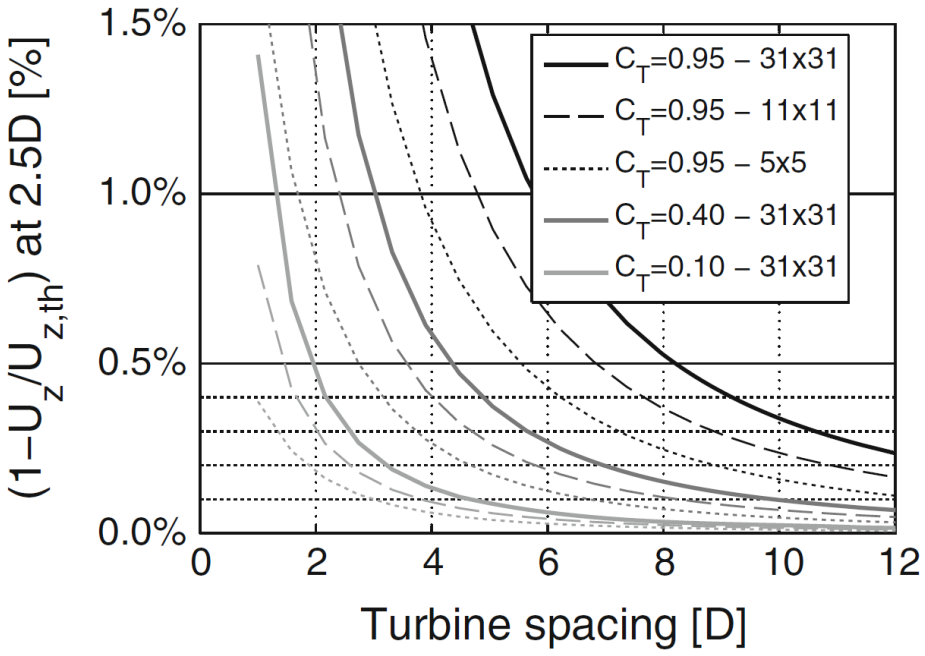

Figure 2.14: Influence of turbine spacing, thrust coefficient and farm size on the GBE [10]

2.4.3. First row behaviour

In A. Segalini's study on the GBE [69], a variance in velocity deficit can be found along the first row, where centre turbines experience the highest velocity deficit and edge turbines the lowest velocity deficit. A. Segalini finds a correlation between the turbine spacing and the first row behaviour where the smaller the turbine spacing, in this case $S_x \cdot S_y$, the higher the difference between centre and edge turbine output due to the GBE.

3

Modelling background: ORFEUS

There are three main methods for investigating of the ABL-flow behaviour around wind farms: analytical modelling, Computational Fluid Dynamics (CFD) and experimental methods. CFD models can be very accurate, but require long CPU times which makes them significantly more expensive. Analytical models have a hard time reaching the same accuracy but come with lower computational costs. Experiments are mainly carried out in wind tunnels or in the field and serve rather as a form of validation than as a form of prediction. [69]

The model used in this thesis project is the linearised RANS modelling software called ORFEUS (On Resource optimisation For Energy USage) [70]. Throughout this Chapter, the implemented background of topics relevant for ORFEUS will be explained.

3.1. ORFEUS

There are many ways of modelling the GBE from resolved physics to modelled physics. The more resolved physics the model contains the higher the computational costs, like the LES methods shown in Figure 3.1. The more the model tends towards modelled physics the less accurate the results are.

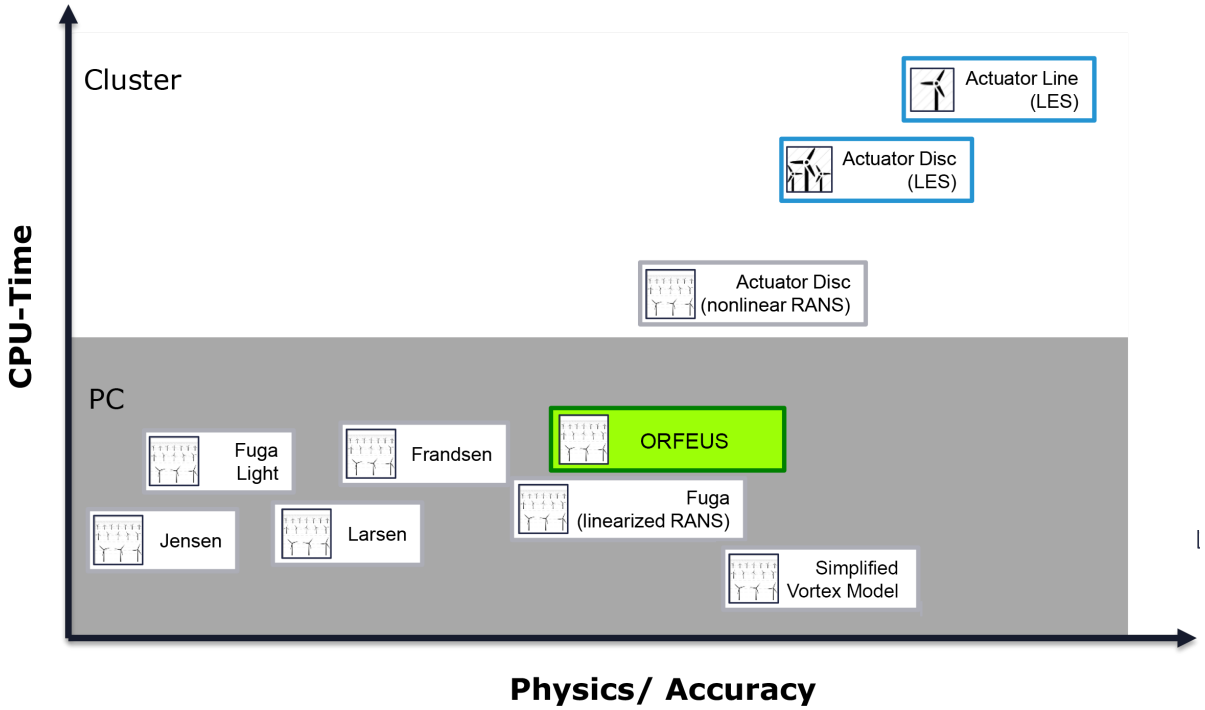

Figure 3.1: Wind farm flow model approaches [11]

ORFEUS is a linearised RANS software based on the theory explained in the previous sections of this Chapter. ORFEUS' strength is its fast execution compared to other CFD models, due to the numerical implementation. ORFEUS' performance towards other wind farm modelling software is estimated in Figure 3.1. It is coded in Python single-handedly by A. Segalini in 2016 [11, 70], based on his previous developed model with Ebenhoch et al. [38]. R. Braunbehrens developed a wake model within ORFEUS and validated his work with the Lillgrund and Horns Rev farms [71]. A. Sebastiani compared the wake losses and blockage effect in ORFEUS with two numerical simulation tools and 10 years of Supervisory, Control And Data Acquisition (SCADA) data for the wind farm of Lillgrund [65]. A. Segalini together with F. Castellani compared ORFEUS' performance with 2 other numerical simulation tools and SCADA data of a wind farm in the South of Italy [70]. G. Crasto et al. compared the modelled freestream flow of ORFEUS with two other numerical simulation tools and validated the results with SCADA data.

Often, wind farm models include wake models which are added "onto" the model. This results in the traditional wake-only approach, in which the GBE can not be included. ORFEUS uses the Actuator Disk (AD) theory, which is further elaborated on in 3.3, which does not result in a wake-only approach, but rather includes the GBE in the turbine interaction losses. There is an option in ORFEUS to include more accurate wake models, like the Jensen wake model, but this is not included in this thesis.

ORFEUS is based on the linearisation of flows to around the parallel base state, which is further elaborated on in Section 3.2.3. In that sense, only perturbations of the base state need to be solved, which are less computational heavy. The numerical execution of ORFEUS is based on two spectral methods: the Fourier method and the Chebyshev method, which are further discussed in 3.4. The Fourier spectral method requires a fringe region, explained in Section 3.6, in order to keep the domain size respectable. The fringe region acts as an artificial recovery region of the disturbed wind. It requires the code to be computed iteratively for all grid points. The user can define the allowed error before the computation is considered converged. The grid dimensioning is adjustable but is equispaced in the horizontal plane. The grid spacing in the vertical direction can be selected more freely and does not have to be uniform. Apart from the computational parameters a user has to deliver turbine specifications, including a Ct curve, power curve and the turbine's dimensioning. As well as the undisturbed velocity profile, farm layout, wind direction and atmospheric stability. The latter is included through Monin-Obukhov Similarity Theory (MOST). This theory is valid for the Atmospheric Surface Layer (ASL) stability. In ORFEUS the theory is active for the entire vertical domain, which in reality would exceed the height of the ASL. The implementation of atmospheric stability through MOST leads to the stability corrected velocity profile. Following Prandtl's mixing length theory the eddy viscosity is obtained from the undisturbed velocity profile. In that way, a vertical profile for the eddy viscosity is formed. The turbulence is only affected by the undisturbed eddy viscosity distribution, which stays the same in the streamwise direction, independent of wake effects, for example.

The following Sections of this Chapter all treat a specific underlying theory relevant for ORFEUS.

3.2. Linearised Reynolds Averaged Navier-Stokes

The Reynolds-averaged Navier–Stokes (RANS) equations are the foundation for many wind farm models, including ORFEUS. The RANS equations are obtained by applying Reynolds decomposition to the Navier-Stokes equations. Reynolds decomposition is the technique where a fluctuating variable is split into an average part and a fluctuating part. This Section elaborates on the derivation of the linearised RANS equations, as this is considered crucial for understanding the basics of the wind farm flow model used in this thesis, and for the sake of understanding the derivation of the boundary conditions for the used spectral methods.

3.2.1. Navier-Stokes equations

To obtain the linearised RANS equations, first, the Navier-Stokes equations are obtained. The Navier-Stokes equations are obtained through the conservation of mass and momentum. The conservation

of mass equation (the continuity equation) of the Navier-Stokes is derived as follows. Say there is a control volume with dimensions $\delta x, \delta y, \delta z$. The inflow can be expressed as follows [46]:

$$\rho U - \frac{\partial}{\partial x}(\rho U)\frac{\delta x}{2}, \tag{3.1}$$

and the outflow as follows:

$$\rho U + \frac{\partial}{\partial x}(\rho U)\frac{\delta x}{2} \tag{3.2}$$

Where ρ is the fluid density (kg/m^3), $\delta x, \delta y$ and δz are the dimensions of the control volume (m) and U is velocity of the fluid (m/s).

Following the conservation of mass equation of the Navier-Stokes equations is constructed:

$$\left[\rho U - \frac{\partial}{\partial x}(\rho U)\frac{\delta x}{2}\right]\delta y \delta z - \left[\rho U + \frac{\partial}{\partial x}(\rho U)\frac{\delta x}{2}\right]\delta y \delta z = -\frac{\partial}{\partial x}(\rho U)\delta x \delta y \delta z \tag{3.3}$$

Ultimately, the mass equation is derived:

$$\frac{1}{\rho}\frac{D\rho}{Dt} + \nabla \boldsymbol{U} = 0 \tag{3.4}$$

Where t is time (s) and $\nabla \boldsymbol{U}$ is the divergence of the velocity vector.

Under the Boussinesq approximation the first term of the continuity equation, $\frac{1}{\rho}\frac{D\rho}{Dt}$, can be neglected as it is small with respect to the divergence of velocity, $\nabla \boldsymbol{U}$, so that the continuity equation becomes:

$$\frac{\partial U}{\partial x} + \frac{\partial V}{\partial y} + \frac{\partial W}{\partial z} = \nabla U = 0 \tag{3.5}$$

The construction of the momentum equations starts with Newton's second law:

$$\Sigma F = ma \tag{3.6}$$

Where F is force (N), m is mass (kg) and a is acceleration (m/s^2). Writing out Newton's second law in parameters of a three dimensional space gives the fully written out Navier-Stokes momentum equation for the x direction:

$$\rho\left(\frac{\partial U}{\partial t} + U\frac{\partial U}{\partial x} + V\frac{\partial U}{\partial y} + W\frac{\partial U}{\partial z}\right) = \rho g_x - \frac{\partial P}{\partial x} + \mu\left(\frac{\partial^2 U}{\partial x^2} + \frac{\partial^2 U}{\partial y^2} + \frac{\partial^2 U}{\partial z^2}\right) \tag{3.7}$$

Where P is pressure (Pa),μ is the dynamic viscosity (Pas). μ is related to the kinematic viscosity, ν, as follows:

$$\nu = \mu/\rho \tag{3.8}$$

3.2.2. Reynolds decomposition

The Reynolds decomposition is used in order to be able to linearise the interactions of perturbations, which will be further explained in Section 3.2.3. The Reynolds decomposition literally decomposes an instantaneous measurement into a mean value and a turbulent fluctuation. By applying the Reynolds decomposition to the incoming boundary layer, the velocity splits:

$$\begin{aligned} U &= U_0 + u, \\ V &= V_0 + v, \\ W &= W_0 + w \end{aligned} \tag{3.9}$$

Where U, V and W are the wind velocities in x-,y- and z-direction respectively (m/s), U_0 and V_0, W_0 are the mean velocities in x-,y- and z-direction respectively (m/s) , u, v and w are the turbulent fluctuation of the wind velocities in x-,y- and z-direction respectively (m/s). Figure 3.2 visualizes the Reynolds decomposition schematically.

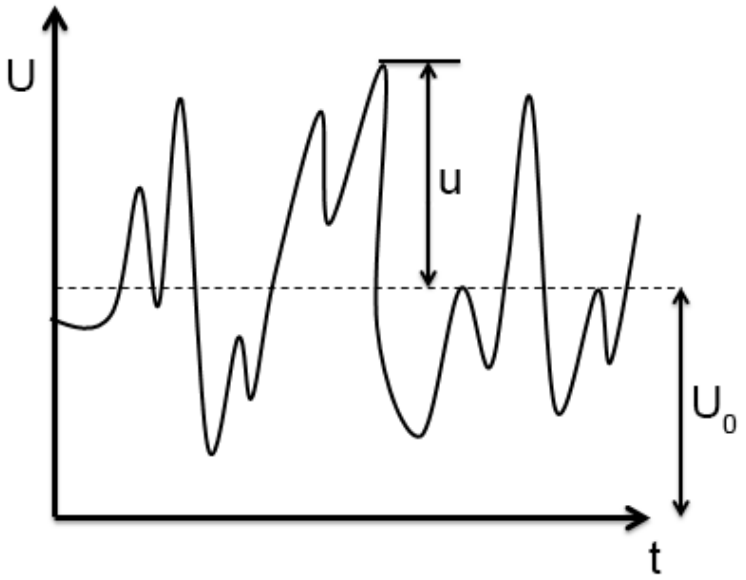

Figure 3.2: Schematic of a potential wind development over time [12].

3.2.3. Linearisation

By linearising, the mean flow called in 3.2.2 is decomposed into a uniform background flow (baseflow), which is assumed to be parallel, and a perturbation induced by the wind farm, defined by F_x and F_y. Through this linearisation of the RANS equations, the products of perturbations will be neglected [46]. After applying the Reynolds decomposition one receives the linearised RANS equations:

$$\begin{aligned} U_0 \frac{\partial u}{\partial x} + w \frac{dU_0}{dz} &= -\frac{\partial p}{\partial x} + \frac{\partial \tau_{xz}}{\partial z} + F_x, \\ U_0 \frac{\partial v}{\partial x} &= -\frac{\partial p}{\partial y} + \frac{\partial \tau_{yz}}{\partial z} + F_y, \\ U_0 \frac{\partial w}{\partial x} &= -\frac{\partial p}{\partial z}, \\ \frac{\partial u}{\partial x} + \frac{\partial v}{\partial y} + \frac{\partial w}{\partial z} &= 0 \end{aligned} \tag{3.10}$$

3.2.4. Turbine kinetic energy

Computing a proper wind shear profile is the foundation of every RANS model, but also hard to assess as so many parameters have an influence on the wind profile. A method for measuring the intensity of turbulence is through the expression of the Turbulence Kinetic Energy (TKE), calculated through Equation 3.11 [4].

$$TKE = 0.5(\overline{U'^2} + \overline{V'^2} + \overline{W'^2}) \tag{3.11}$$

Where $\overline{U'^2}$, $\overline{V'^2}$, $\overline{W'^2}$ are the latitudinal, longitudinal and vertical velocities (m/s) respectively. In RANS models, the expression of TKE can be used to obtain the eddy viscosity, ν_t, in Equation 3.12.

$$\nu_t = c\sqrt{k}l_m \tag{3.12}$$

Where c is a coefficient, k is the TKE (J/kg) and l_m is the mixing length (m). Through this method, better estimations of near-wall velocity profiles and turbulence characterisation (K - ϵ model) can be obtained [72]. The version of ORFEUS with which this thesis was carried out, did not include TKE based calculation of the eddy viscosity. Instead, the eddy viscosity, as a function of height, in this version of ORFEUS is calculated through the friction velocity and the undisturbed velocity profile, as shown in Equation 3.2.4:

$$\nu_t(z) = \kappa u_* z \tag{3.13}$$

Where κ is the Von Kármán constant, u_* is the friction velocity (m/s) and z is the height (m). In the ASL the friction velocity can be considered constant. In ORFEUS, the friction velocity is considered constant throughout the entire domain. As the undisturbed velocity profile changes with atmospheric stability, the eddy viscosity profile does too.

3.3. Linearised Actuator Disk theory

The wind turbines in a wind farm apply a force on the incoming boundary layer. Three methods for modelling this force are discussed. One way is to model the wind turbines collectively as a canopy interacting with the incoming boundary layer. The canopy can be represented as individual blocks, representing the turbines, as shown in Figure 3.3, or as one single block. A second approach is to include the effect of the wind turbines in the effective surface roughness. A third way of implementing the wind turbine forces is through the AD theory, as shown in Figure 3.4. In this method, the wind turbines are seen as porous disks applying a uniform distributed force, f_i in Equation 3.10, on the incoming boundary layer.

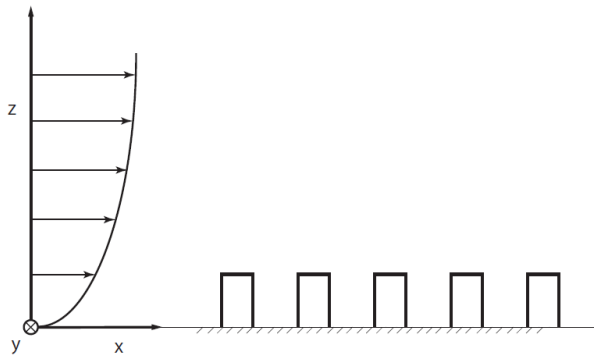

Figure 3.3: The geometry of the canopy approach

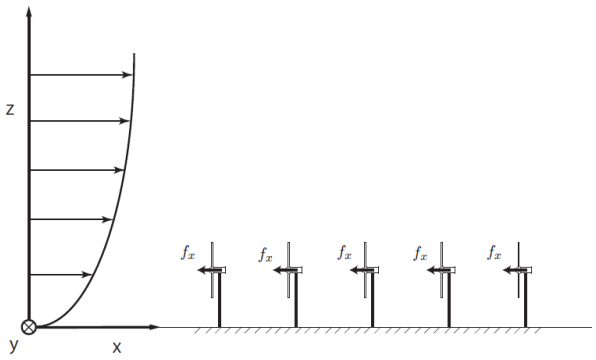

Figure 3.4: The geometry of the AD approach

The total force of a turbine is defined in Equation 3.14.

$$F_x = T = \frac{1}{2}\rho U_{turbine}^2 C_T A \tag{3.14}$$

Where T is the collective disk thrust force, $U_{turbine}$ is the velocity at the turbine (m/s) expressed in Equation 3.15, C_T is the thrust coefficient and A is the area of the disk. The velocity at each turbine is obtained by integrating the velocity components located in the rotor volume.

$$U_{turbine} = \frac{1}{V} \int U dV \tag{3.15}$$

Where U is the local velocity of the grid point in the disk (m/s) and V is the volume of the disk (m^3).

In ORFEUS, the freestream velocity is estimated with a calibration function:

$$U_{\infty,estimated} = U_{turbine} \cdot f(C_T) \tag{3.16}$$

The sensitivity as a result of the tower, the hub distance to the ground, the Reynolds number are included in the C_T.

3.4. Spectral Methods

3.4.1. A spectral method definition

There are several main methods to numerically solve the differential equations and to find values for the grid points: Direct Numerical Simulation (DNS), finite difference methods, finite volume methods and spectral methods. Finite difference methods are based on obtaining solutions for small finite elements, from the meshed space, based on their neighbouring values and solutions. This may require very fine democratization and therefore a very computational heavy method of solving and loses out in accuracy if not computed correctly. Spectral methods aim to create an algebraic function out of the differential equation. This is done by transforming the differential equation to a different domain, e.g., the frequency domain. The advantage of this method is that, without losing out on accuracy, a lot of computational power is saved, but it also has limited flexibility when modelling complex geometries [73].

The two spectral methods used in ORFEUS are the Fourier spectral method and the Chebyshev spectral method. The requirement for the Fourier spectral method is that the input needs to be periodic without boundary conditions. The horizontal plane can be seen as infinite as there are no boundary conditions on any side of the wall parallel plane. Therefore, the streamwise and spanwise directions of the wind farm can be expressed as infinite and periodic inputs, which makes the Fourier spectral method an appropriate method. The Fourier method is not suitable for the vertical dimension as both the ground and top of the ABL require boundary conditions. The Chebyshev spectral method is more suitable for the vertical dimension as this spectral method includes boundary conditions, which for ORFEUS are explained in the following Section 3.4.2. Chebyshev does not work with an equispaced grid and therefore enables a refinement towards the boundaries. ORFEUS makes use of both the Fourier spectral method and the Chebyshev spectral method.

3.4.2. Boundary conditions

The boundary conditions for the Chebyshev method, at the top and bottom boundary conditions, are constructed as follows in ORFEUS:

- The lower boundary condition should imply the wall function, where U(Z=0) = 0 m/s.
- The higher boundary condition is derived as follows:

At high distances above the farm, the velocity is considered almost constant, so that the term $\frac{dU_0}{dz}$, from the Navier-Stokes Equations 3.10 is neglected. No external forces and stresses, like thrust forces from the turbines, are assumed to be present at this high altitude, so that the terms $\frac{\partial \tau_{xz}}{\partial z}$ and $\frac{\partial \tau_{yz}}{\partial z}$, f_x, f_y and f_z from Equations 3.10 are considered to be 0, giving the reduced RANS equation shown in Equation 3.17:

$$\begin{aligned} U_0 \frac{\partial u}{\partial x} &= -\frac{\partial p}{\partial x}, \\ U_0 \frac{\partial v}{\partial x} &= -\frac{\partial p}{\partial y}, \\ U_0 \frac{\partial w}{\partial x} &= -\frac{\partial p}{\partial z}, \\ \frac{\partial u}{\partial x} + \frac{\partial v}{\partial y} + \frac{\partial w}{\partial z} &= 0 \end{aligned} \tag{3.17}$$

When then taking the divergence of the momentum equations:

$$U_0 \frac{\partial}{\partial x}(\nabla u) = -\nabla \nabla p = -\nabla^2 p, \tag{3.18}$$

Combining this equation with the continuity equation, $\nabla u = 0$, this leads to:

$$\nabla^2 p = 0 \tag{3.19}$$

at high altitudes. Combining this statement with the Laplacian of the w-momentum equation gives:

$$U_0 \frac{\partial}{\partial x}(\nabla^2 w) = -\frac{\partial}{\partial x}\nabla^2 p = 0 \rightarrow \frac{\partial}{\partial x}(\nabla^2 w) = 0, \tag{3.20}$$

Assuming that far upstream, at x = $-\infty \rightarrow \nabla^2 w = 0$, from Equation 3.20 one obtains the upper boundary condition above the farm of $\nabla^2 w = 0$.

3.5. Incoming boundary layer

The incoming boundary layer can be seen as the velocity input for the linearised RANS equations. The function for the incoming boundary layer represents the undisturbed wind profile U_∞ and can be implemented in several ways, of which the most common are the power law, the logarithmic law, the uniform flow and the Deaves and Harris (D&H) model. These most common velocity profiles are expressed in Figures 3.5 - 3.7 with the concerning equations [74, 75]. The uniform profile is the most simplistic velocity profile being homogeneous in the vertical direction and does not represent a realistic velocity profile, but is rather used for the sake of its simplicity in simulations. The logarithmic law considers the impact of the surface and its roughness. From 60 m and above the logarithmic law starts to deviate from the actual wind profile. The power law should replace the logarithmic law for z>60m altitudes [76]. The advantage of the D&H is the ease of implementation, as it is a single function with the same accurate representation as the logarithmic law at low heights and reaches up to the top of the ABL [75].

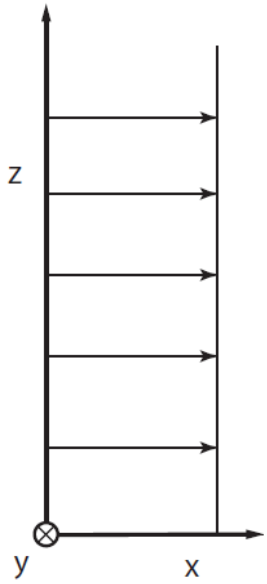

Figure 3.5: Uniform profile

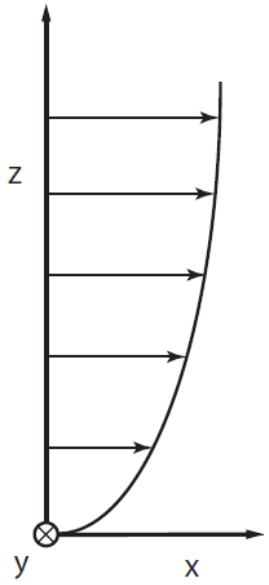

Figure 3.6: Logarithmic law profile

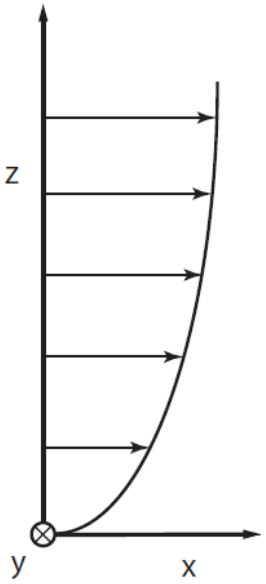

Figure 3.7: Power law profile

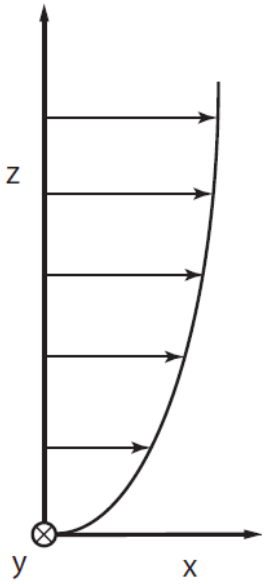

Figure 3.8: D&H profile

$$U(z) = C \qquad \text{(Uniform profile)}$$

$$U(z) = U(z_\infty) \cdot \frac{\ln(z/z_0)}{\ln(z_\infty/z_0)} \qquad \text{(Logarithmic law)}$$

$$U(z) = U(z_{ref}) \cdot \left(\frac{z}{z_{ref}}\right)^{\alpha} \qquad \text{(Power law)}$$

$$U(z) = \frac{u_*}{\kappa}\left[\ln\frac{z}{z_0} + 5.75\left(\frac{z}{z_{ref}}\right) - 1.88\left(\frac{z}{z_{ref}}\right)^2 - 1.33\left(\frac{z}{z_{ref}}\right)^3 + 0.25\left(\frac{z}{z_{ref}}\right)^4\right] \qquad \text{(D\&H profile)}$$

Where U(z) is the wind speed at height z (m/s), z_0 is the surface roughness (m), z_{ref} is the reference height, $U(z_{ref})$ is the wind speed at reference height (m/s), u_* is the friction velocity (m/s), κ is the Von Kármán constant (-), α is the Hellmann exponent (-) [77].

3.6. Fringe Region

As stated in Section 3.4, ORFEUS uses the Fourier method for computing both horizontal directions. As this method is periodic and proposedly infinite, it does not have a natural boundary. An artificial boundary has to be set in order to achieve a computational domain [78]. In ORFEUS, periodic boundary conditions are imposed at the artificial boundary.

The fringe region (filter, damping layer, absorbing layer and sponge layer) is an artificial buffer implemented in a model on the back or sides of the wind farm to prevent turbine wake effects from being recycled back into the inlet of the farm [45], as visualised in Figure 3.9. P. Spalart introduced this method and called the fringe region a ”black hole” where information gets destroyed” [79].

Following this approach, the computational domain is split into a useful region, in which the turbines are located, and a fringe region, as can be seen in Figure 3.10. If one chooses not to implement a fringe region, the streamwise computational domain would have to be significantly larger, as all disturbances would have to decay by diffusion processes, before retrieving the desired inflow conditions [38]. Hence, the decay in the fringe region is accelerated by imposing a ”non-physical force”, the fringe force, so that the desired inflow conditions are obtained at the end of the domain.

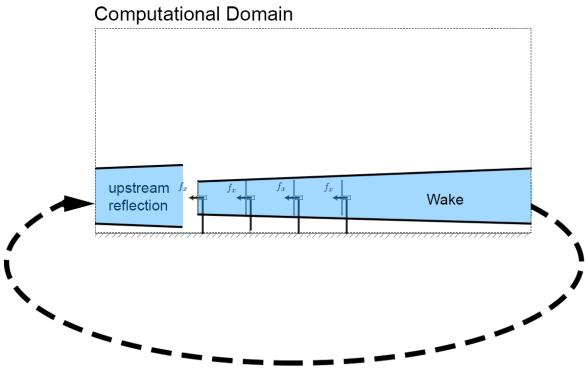

Figure 3.9: Side view of computational area without fringe region

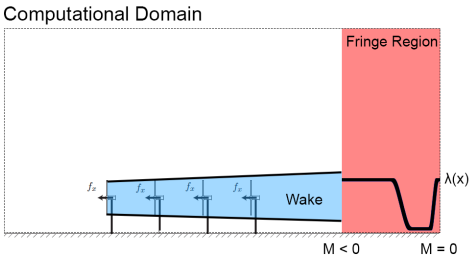

Figure 3.10: Side view of the computational area with an effective fringe region

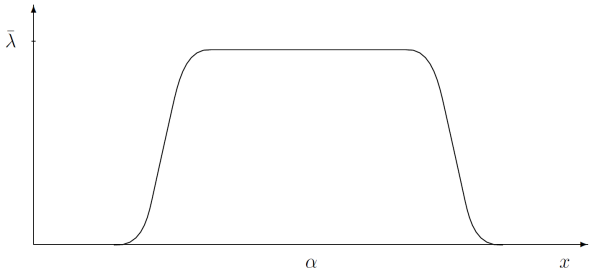

Figure 3.11: Nordström's visualization of the fringe function [13]

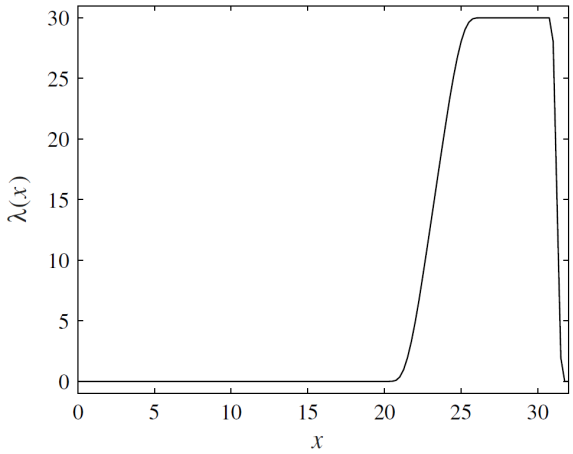

Figure 3.12: Schlatter's visualization of the fringe function [14]

The magnitude of this fringe force is defined by the fringe function. The fringe function used in ORFEUS is based on Lundblad's method [80], also used by J. Nordström [13] and by Schlatter [14] who both visualised the same fringe function as Figure 3.11, 3.12 accordingly. Equation 3.21 describes this generic fringe function.

$$\lambda(x) = \bar{\lambda}[S\left(\frac{x - x_{start}}{\Delta_{rise}}\right) - S\left(\frac{x - x_{end}}{\Delta_{fall}} + 1\right)], \tag{3.21}$$

where λ_{max} is the maximum damping strength, x is the streamwise position, x_{start} is the streamwise starting distance of the fringe region, x_{end} is streamwise ending distance of the fringe region, Δ_{rise} is the rise distance, Δ_{fall} is the fall distance and $S()$ is the smoothed step function described in 3.22.

$$S(x) = \begin{cases} 0 & x \leq 0 \\ 1/[1 + \exp\left(\frac{1}{x-1} + \frac{1}{x}\right)] & 0 < x < 1 \\ 1 & x \geq 1 \end{cases} \tag{3.22}$$

ORFEUS uses this fringe region method, but with a slightly adopted fringe function:

$$\lambda(x) = -6 * \frac{[S\left(\frac{x-x_{start}}{0.5*(x_{end}-x_{start})}\right) - S\left(\frac{x-x_{end}}{0.2*(x_{end}-x_{start})} + 1\right)]}{x_{end} - x_{start}}, \tag{3.23}$$

Finally, the nonphysical force is created in Equation 3.24. Lundbladh states that to achieve maximum damping, both the total length of the fringe and λ_{max} have to be tuned [80].

$$F_{fringe} = -\bar{\lambda} \cdot \lambda(x)u \tag{3.24}$$

4

Methodology

This chapter describes the methodology for reaching the required foundation for answering the research questions. The chapter starts with a description of the simulated wind farm setup in Section 4.1. Section 4.2 follows up with a description of the verification process on which the decisions for the configurations are based. Section 4.3 backs the choice of the selected simulation parameters. Section 4.4 immerses in the quantification of the GBE. The final Section 4.5 compares the performance of ORFEUS' GBE under neutral conditions with the LES study on the GBE of J. Strickland [36].

4.1. Theoretical case: 5 by 5 turbine farm

This section describes the decisions made regarding the offshore wind farm setup used in the simulations.

This research was initially set up for the existing offshore wind farm of Lillgrund on which previous studies regarding the GBE [81] and atmospheric stability [82] has been done but was shifted to a theoretical 5 by 5 offshore wind farm. This decision was made to avoid possible influence by Lillgrund's arbitrary farm layout and due to the lack of LIDAR data, as the more common glsSCADA data is not covering the required data for this research regarding atmospheric stability. Instead, a lateral and longitudinal perfectly aligned, symmetrical, theoretical 5 by 5 farm was set up. For the sake of convenience, identical wind turbines and simulation conditions as existing in the Lilgrund wind farm are applied to the 5 by 5 theoretical farm, which will be deeper explored in the rest of this Section.

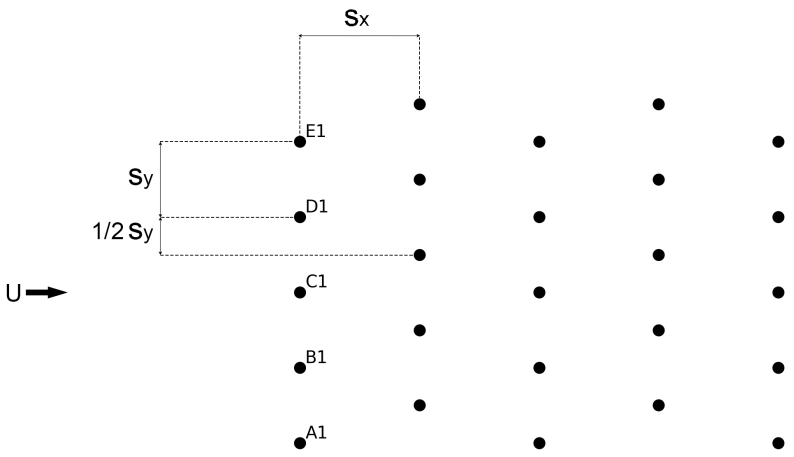

Figure 4.1: Overview of theoretical 5 by 5 farm

Figure 4.1 gives an overview of one of the simulated 5 by 5 farm setups including turbine spacings and wind direction. The Lillgrund turbine spacing of s_x = 4.30D, giving S_x = 400 m, and s_y = 3.30D, giving S_y = 307 m [81] is assumed for the 5 by 5 farm, as visualised in 4.15. Table 4.1 presents the turbine specifications of the selected Siemens 2.3 MW MK II turbine. The rotor diameter of, $D = 93$ m, will be used to normalize distances. The hub height will be referred to as $Z_{ref} = 65$ m. U_∞ is the freestream velocity at Z_{ref}.

Table 4.1: Turbine Specifications Siemens 2.3 MW MK II [15]

Specification	value
Rotor type	3-bladed, horizontal axis
Rotor position	Upwind
Rotor diameter	93 m
Hub height	65 m
Swept area	6800 m2
Rotor speed	6 – 16 rpm
Aerodynamic regulation	Pitch regulation
Yaw system	Active
Controller type	Microprocessor
glsSCADA system	WPS
Tower	Cylindrical
Rotor weight	60 ton
Nacelle weight	82 ton
Tower weight (70 m)	134 ton

4.2. Case verification

The verification of the theoretical wind farm is done in two stages. In Sections 4.2.1 and 4.2.2, the right domain sizing and fringe settings are decided in the upstream reflections study. Thereafter, in Sections 4.2.3 and 4.2.4, a GCS is done in order to obtain the right computational resolution settings.

4.2.1. Setup Upstream reflections study

Every form of simulating needs a verification process to produce correct and realistic results, this is no different for simulating in ORFEUS. Figure 4.2 demonstrates a run in case the verification process is disregarded and ORFEUS is run on its default settings for the 5 by 5 farm. In this case, the fringe region is not dimensioned correctly, resulting in unrealistic results in the form of unphysical upstream reflections, due to missing momentum in the periodicity of the horizontal Fourier method, leading to upstream wake reflections. Section 3.6 provides the background in detail of the fringe region and upstream reflections.

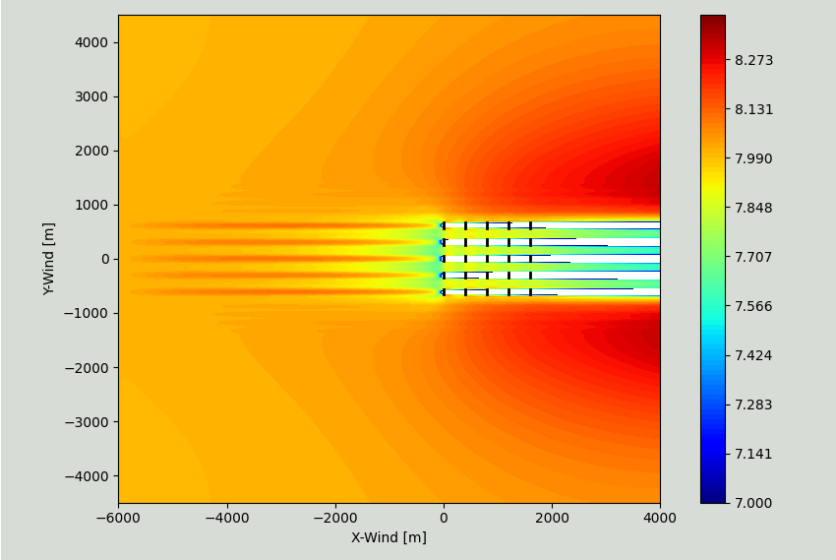

Figure 4.2: 5 by 5 farm ran on ORFEUS default settings

The main purpose of this sensitivity study is to reach the right simulation dimensions and fringe characteristics, so that upstream wake reflections are avoided and the flow around the wind farm is more continuous and realistic. The extend of the upstream wake reflections was dependent on the atmospheric stability class. As the upstream wake reflections were most severe under very stable conditions, the sensitivity process will be executed under the very stable atmospheric stability class. After reaching the desired parameters for the very stable stability class, the behaviour of the other stability classes will be further investigated. Table 4.2 shows the parameters that were investigated in the upstream reflections study. The optimal outcome is initially decided by the eye from top down colour plots and subsequently examined by comparing quantitative results.

Table 4.2: Model parameters studied in the verification process

Parameter	Minimum value	Maximum value
Fringe length (constant fringe start)	11000 [m]	23000 [m]
Fringe start (constant fringe length)	5000 [m]	13000 [m]
Fringe start (constant fringe ending)	5000 [m]	13000 [m]
Fringe intensity	0.9 [-]	1.3 [-]
Domain start	-4000 [m]	-12000 [m]
Spanwise domain	7000 [m]	15000 [m]
Vertical domain	1000 [m]	5000 [m]
Turbine delta	30 [m]	110 [m]
Nz	30 [-]	70 [-]
Nx & Ny	64 [-]	1028 [-]
Surface roughness*	0.0001 [m]	0.01 [m]

* Not a computational parameter

It is expected that the fringe length and fringe intensity will have the highest impact on the upstream reflections. The definitions of these parameters have been explained in section 3.6. Tables 1 - 11 in Appendix A shows the complete Design of Experiments (DoE) for the upstream reflections study. 4.3 reveals all selected parameters. The final results for this sensitivity study are presented in Section 4.2.2. The optimal value from these results was not selected for every parameter, either because the

selected value showed similar performance and was preferred for the sake of computational time, or the parameter was not of influence at all.

4.2.2. Upstream reflections study results

This Subsection presents the essential results of the upstream reflections study. More results of this upstream reflections study can be found in Appendix B. Figures 4.3 and 4.4 show a top down colour plot of the wind farm before verification and after verification under very stable conditions. The streamwise velocity is coloured on a scale from U = 7.0 m/s to 8.4 m/s. One can observe that after tuning the computational parameters an improved upstream behaviour is shown with less upstream disturbance.

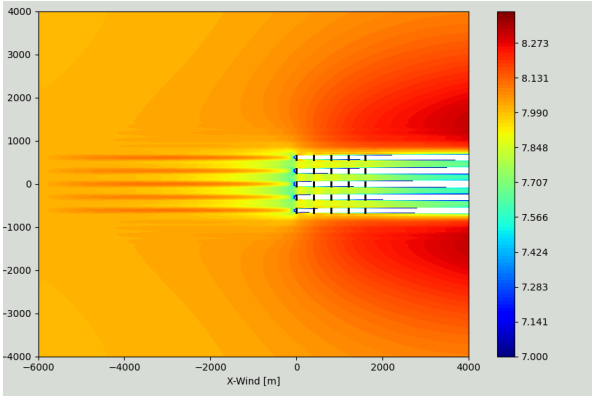

Figure 4.3: Colour plot of farm under very stable conditions with pre-verification settings

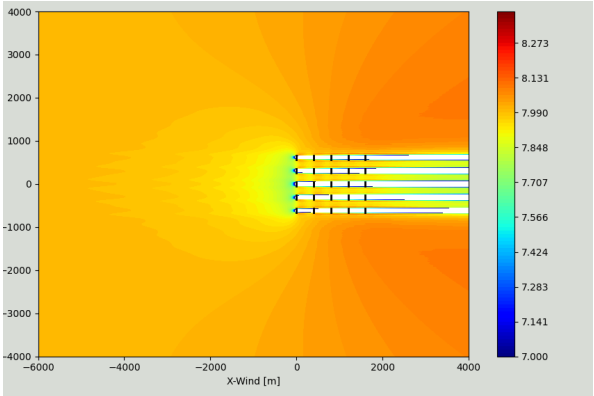

Figure 4.4: Colour plot of farm under very stable conditions with post-verification settings

Table 4.3 summaries the results of the upstream reflections study. For every parameter, five different values are taken between the lowest and the highest value. The impact stands for the corresponding parameter. The optimal value returns the optimal value based on the evaluation of the top-down colour plots by the eye. Parameters associated with the fringe region had the most impact. Parameters associated with the grid resolution also were of influence, which increased the urgency for a GCS.

Table 4.3: Model parameters studied in the verification process

Parameter	Lowest value	Highest value	Impact[1]	Optimum
Fringe length (constant fringe start)	11000 [m]	23000 [m]	++	23000 [m]
Fringe start (constant fringe length)	5000 [m]	13000 [m]	++	23000 [m]
Fringe start (constant fringe ending)	5000 [m]	13000 [m]	–	13000 [m]
Fringe intensity	0.9 [-]	1.3 [-]	++	1.2
Domain start	-4000 [m]	-12000 [m]	–	4000, 6000 [m]
Spanwise domain	7000 [m]	15000 [m]	–	7000 [m]
Vertical domain	1000 [m]	5000 [m]	+	4000 [m]
Turbine delta	30 [m]	110 [m]	–	50
Nz	30 [-]	70 [-]	+-	30, 40, 50
Nx & Ny	64 [-]	1028 [-]	+	512 x 512
Surface roughness*	0.0001 [m]	0.01 [m]	–	–

[1] – no impact, - minimal impact, +- small impact, + some impact, ++ high impact

[*] Not a computational parameter

Apart from comparing the colour plots by the eye, a more quantitative approach was done. The velocity gradient upstream of the farm is compared both upstream of the centre first turbine and exactly between the centre turbine its neighbouring turbine. Figure 4.5 compares the normalized

upstream velocities over the reference speed so that nonphysical values are easier to capture. From Figure 4.5 an unphysical increase for the centreline turbine, labelled Uc, and an unphysical decrease for the upstream velocity midway between two turbines, labelled $Umid$, can be observed. After the verification process Uc and $Umid$ show a more identical behaviour.

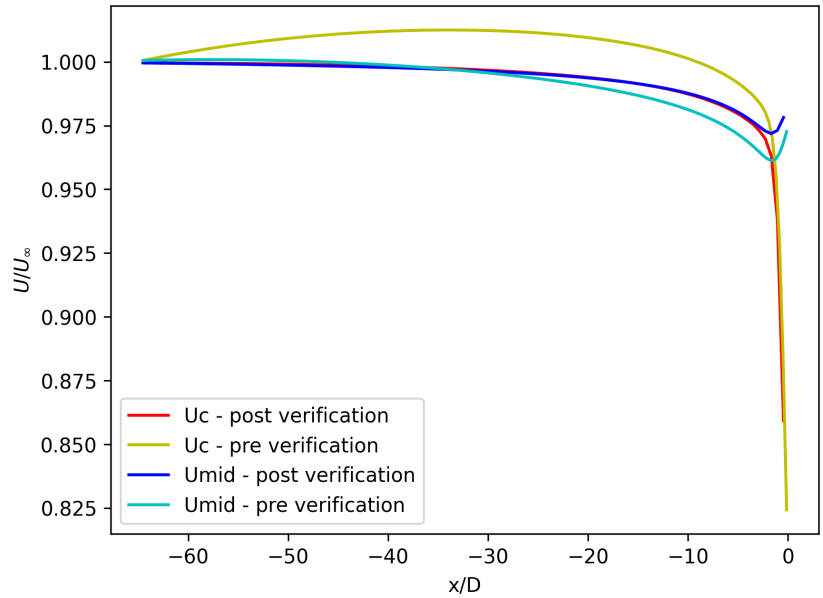

Figure 4.5: Upstream velocity behaviour pre- and post-verification

4.2.3. Setup grid convergence study

After the elimination of the upstream reflections, a grid convergence study was done to obtain the correct dimensional resolution in ORFEUS. The performance of the individual turbines in the first row of the aligned farm was compared under different grid resolutions. Table 4.4 shows the DoE for the Grid Convergence Study (GCS). The GCS is done with a fringe intensity of 1.1 and 1.2, which is not shown in Table 4.4 but contains the same N_y and N_z. The results from the upstream reflections study resulted in a slight preference for a fringe intensity of 1.2, but for the sake of convergence and computational time, a fringe intensity of 1.1 would be preferred.

Table 4.4: Design of Experiments (DoE) for the GCS

Fringe	Ny	Nz
1.1	50	20
1.1	50	50
1.1	50	100
1.1	300	20
1.1	300	50
1.1	300	100
1.1	625	20
1.1	625	50
1.1	625	100
1.1	1000	20
1.1	1000	50
1.1	1000	100

The following Section 4.2.4 presents the results of the GCS. Based on these results of the GCS a grid resolution of $N_y = 625$, $N_z = 50$ and fringe intensity = 1.1 were selected. This resulted in a rotor coverage of 48 grid points in the vertical YZ-plane.

4.2.4. Grid convergence study results

This Subsection presents the results of the Grid Convergence Study (GCS). The complete GCS can be found in Appendix C.

Tables 4.5 and 4.6 show the processed results from the GCS. As the aligned farm behaves symmetrical, the power ratios are only shown from the centre turbine, C1, to one side, E1. The trend column is added to clarify whether an increase or decrease of power production occurs, working from the centre to the edge turbine. The computational time varied with the resolution but was not tracked.

Table 4.5: Ratio edge turbine to centre turbine at fringe intensity 1.1

Fringe	Ny	Nz	C1/C1	D1/C1	E1/C1	Trend
1.1	50	20	DNC	DNC	DNC	DNC
1.1	50	50	DNC	DNC	DNC	DNC
1.1	50	100	DNC	DNC	DNC	DNC
1.1	300	20	1	1.094	1.118	↑↑
1.1	300	50	1	1.090	1.139	↑↑
1.1	300	100	1	1.086	1.129	↑↑
1.1	625	20	1	1.001	1.004	↑↑
1.1	625	50	1	1.009	1.019	↑↑
1.1	625	100	1	1.012	1.026	↑↑
1.1	1000	20	1	1.000	1.004	↑↑
1.1	1000	50	1	0.998	1.002	↓↑
1.1	1000	100	1	0.995	0.999	↓↑

[1] DNC = Did Not Converge

Table 4.6: Ratio of the edge turbines to the centre turbine at fringe intensity 1.2

Fringe	Ny	Nz	C1/C1	D1/C1	E1/C1	Trend
1.2	50	20	DNC	DNC	DNC	DNC
1.2	50	50	DNC	DNC	DNC	DNC
1.2	50	100	DNC	DNC	DNC	DNC
1.2	300	20	1	1.094	1.119	↑↑
1.2	300	50	1	1.090	1.140	↑↑
1.2	300	100	1	1.086	1.129	↑↑
1.2	625	20	1	1.001	1.004	↑↑
1.2	625	50	1	1.009	1.020	↑↑
1.2	625	100	1	1.012	1.026	↑↑
1.2	1000	20	1	1.000	1.004	↑↑
1.2	1000	50	1	0.998	1.002	↓↑
1.2	1000	100	1	0.995	0.999	↓↑

[1] DNC = Did Not Converge

From tables 4.5 and 4.6 one can observe that low-resolution runs did not converge, while too high resolutions lead to oscillating patterns in the power production, observing from the centre to the edge turbine. Where one expects a continuous increase from the centre to the edge turbine. Although there was a small margin in power results, a preference was made selecting N_y= 625 and N_z= 50. With N_x= 1024, a detailed resolution was obtained, while limiting the computational time. The simulation converges and a realistic gradient in the power production along the first row was obtained at this resolution. The fringe intensity was selected to be 1.1 as this leads to more security of convergence and less computational time.

4.3. Simulation configuration settings

After the upstream reflections study and the GCS, the final computational simulation settings were obtained. Other key parameters and their selected values are elaborated on in this Section.

4.3.1. Surface roughness

Section 2.1.3 presents the theoretical background of the surface roughness and its influence on the velocity profile. European Wind Atlas assumes a surface roughness of $z_0 = 2 \cdot 10^{-4} m$ for conditions over water surfaces [83], which is a value which is used by A. Creech's approach in his high-resolution CFD modelling of Lillgrund [84] and is taken as a standard for water surfaces in wind modelling software WAsP [85] as well as presented in his lecture reader [76] at the TU Delft, M. Zaayer. These arguments were convincing enough to use a surface roughness of $z_0 = 2 \cdot 10^{-4} m$ in all simulations. ORFEUS does not include Charnock's Equation of relating the surface roughness to the wind shear, which was explained in Section 2.1.3.

4.3.2. Turbine delta

The turbines apply a thrust force which is located in the rotor plane of the turbine:

$$F_{thrust} = -\alpha \cdot U^2 \tag{4.1}$$

Where F_{thrust} is the thrust force. α a calibrated coefficient function [81]. U is the local velocity at the rotor. ORFEUS computes its iterations at every grid point, which do by default not coincide with the turbine rotors. To let the grid points coincide with the thrust force, the force is smoothed and distributed in the streamwise direction using a Gaussian filter. The turbine δ parameter is the standard deviation of this Gaussian distribution. A less smoothed Gaussian filter would be the better representation of the thrust force at the rotor, this also means that the grid points do not read the force at its actual value, but possibly an undervalued force. A value of $\delta \sim 1.5 \cdot \Delta X$ is advised by A. Segalini [86], in which ΔX is the streamwise grid spacing. With the streamwise domain length of 26km and a streamwise resolution of $N_x = 1024$, a $\Delta X = 25.0$ is reached, resulting in a turbine delta value of $\delta \sim 1.5 \cdot 25.0 \approx 35.0$.

4.3.3. Convergence

A numeric result cannot always be found in the easy form of:

$$\begin{aligned} A(x) &= B \\ x &= A^{-1} \cdot B \end{aligned} \tag{4.2}$$

ORFEUS computes in iterations and converges to a computed value, as discussed in Chapter 3. For iterative algorithms, a result is reached when the output converges. If the output diverges, no valid result is reached. The convergence parameter is the threshold that defines a converged simulation. The smaller the convergence parameter, the smaller the allowance of error during the iterations. In other words, the smaller the convergence parameter, the more reliable the output. For these simulations, a convergence of 0.001 m/s is assumed, which is also the recommended value by the ORFEUS manual [86].

4.3.4. Ramping value

At every iteration in ORFEUS, a new value is constructed at every grid point which is partly based on the previously computed solution and party based on the new calculated solution. The ramping value, $k_{ramping}$, indicates the ratio between the contribution of the old computed force and the new computed force, through the relaxation factor, α. The new solution is computed as follows,

$$S_1 = \alpha S_x + (1 - \alpha) S_0 \tag{4.3}$$

Where S_1 is a given solution, S_x is a new computed solution, S_0 is the old computed force and α is the relaxation factor. With $\alpha = 1$ the old computed force is completely cancelled out and replaced by the new computed solution, S_x. In ORFEUS, the relaxation factor α is based on the ramping parameter:

$$\alpha = 1 - \frac{k_{ramping} - 1}{10} \tag{4.4}$$

For these simulations, the default value of the ramping value of $k_{ramping} = 4$ is assumed. The ramping value has a second function: the forces of the turbines are introduced throughout the iterations. This is done as strong forces might lead to divergence. As the ramping value decreases the magnitude of these strong forces, divergence is prevented. With every iteration, the impact of the ramping value on the forces decreases (13% effective after 3 iterations, 2% effective after 5 iterations), so the final result is not impacted by the ramping value.

4.3.5. Final simulation configuration

Table 4.2 summarizes the selected simulation configuration within ORFEUS. After the sensitivity study in 4.2.1 a total fringe length of 50% of the total streamwise domain was reached.

Table 4.7: Selected model configuration

Parameter	Selected value
Domain start	-6000 [m]
Domain end	20000 [m]
Domain length	26000 [m]
Spanwise domain	-5000 to 5000 [m]
Vertical domain	0 to 1000 [m]
Fringe start	7000 [m]
Fringe length	13000 [m]
Fringe intensity	1.1 [-]
Nx & Ny	1024x625 [-]
Nz	50 [-]
Turbine δ	35 [m]
Convergence	0.001 [m/s]
Ramping value,	4
Surface roughness	0.0002 [m]

Figure 4.6 shows the complete computational domain with the aligned farm inside.

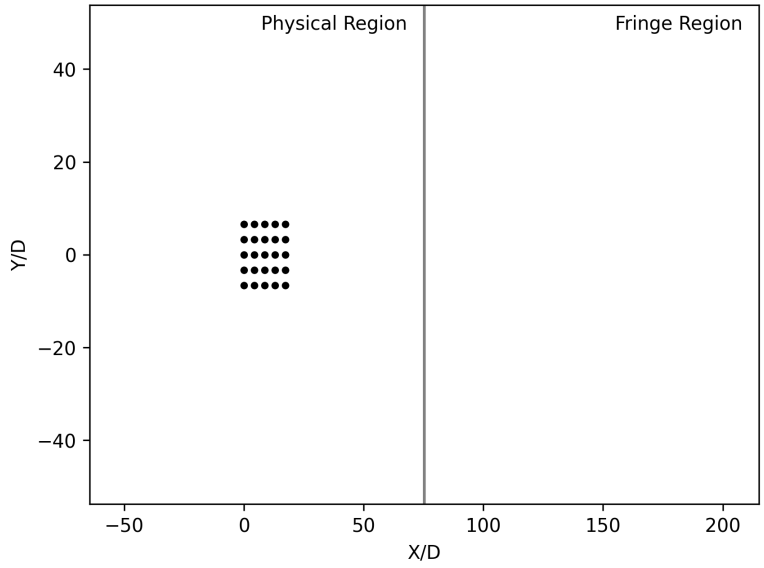

Figure 4.6: The complete computational domain

To find answers for the research questions, the setup so far needs to be run for different reference velocities. The reference velocity is here considered the freestream velocity, U_∞, at hub height Z_{hub} = 65 m. With the cut-in speed, U_C, of 4 m/s and rated wind speed, U_R, of 13 m/s the range of reference wind speeds was selected to be from 3 m/s to 18 m/s. J. Barthelmie [6], M. Holtslag [19], M. Motta [5], R. Barthelmie [23] and A. Sathe [22, 87] all show similar atmospheric stability distributions over wind speed. Figure 4.7 shows an example of the frequency of occurrence of stability classes as a function of wind speed. As can be seen from Figure 4.7 some stability classes barely occur at certain wind speeds. In the simulations, however, this causality is disregarded and for every wind speed bin, all stability classes will be investigated.

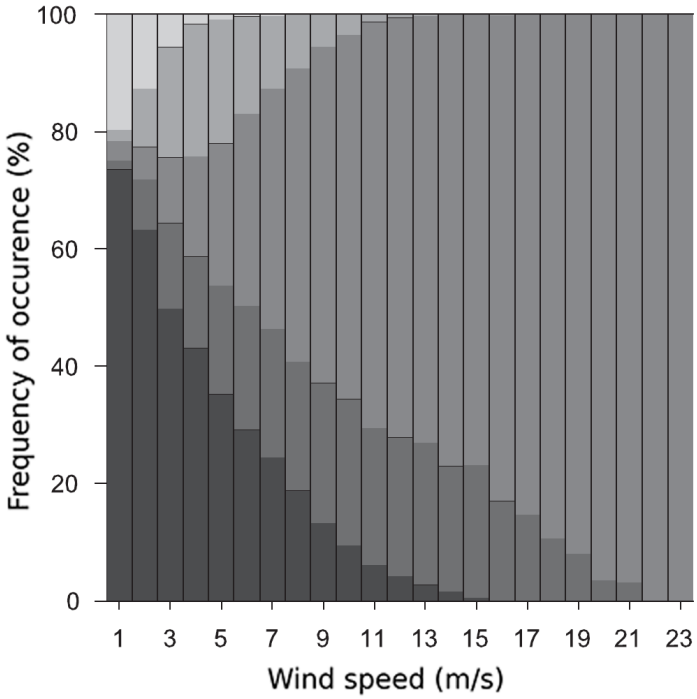

Figure 4.7: Variation of frequency of occurrence of atmospheric stability with respect to wind speed at off-shore farm Omø [5]

J. Bleeg [88] presents two ways of determining the Obukhov length at a given site when measuring the Obukhov length is no option:

1. If the same numerical simulation model, including atmospheric stability, has already been applied to a similar wind farm in a similar location, the same Obukhov length can be used.
2. If the farm is in a region where no previous numerical simulations, including atmospheric stability, has been carried out, the Obukhov length should be calibrated to the most representative value.

As the farm in this thesis project is a 5 by 5 fictitious farm in which no stability classification was delivered, a broad study on the stability classification from literature was done, which is completely shown in Appendix D. To pursue these results, the four different setups as discussed in Section 4.1, will be run under 5 different atmospheric conditions. Based on the stability classification in Table 17 the centre value of every class is taken, leading to the values representing 5 different stability classes as shown in Table 4.8. With the variable height z in the stability parameter z/L, no standard height for stability measurements is set. Converting the selected L classification to the z/L classification leads to different z/L values depending on the z value used in the classification. The values for the selected stability classes, expressed as ranges of L in Table 4.8, are in agreement with the z/L classifications from A. Peña's [26] and S. Rodrigo's [25] which have a reference height $z = 15$ m and $z = 80$ m respectively. Figure 4.8 shows the velocity profiles for the 5 selected stability classes from Table 4.8.

Table 4.8: Selected stability classification for simulations

Stability Class	L	z/L z=15	z/L z=80
Very stable	200 m	0.075	0.40
Stable	600 m	0.025	0.13
Neutral	5000 m	0.0030	0.016
Unstable	-600 m	-0.025	-0.13
Very unstable	-200 m	-0.075	-0.40

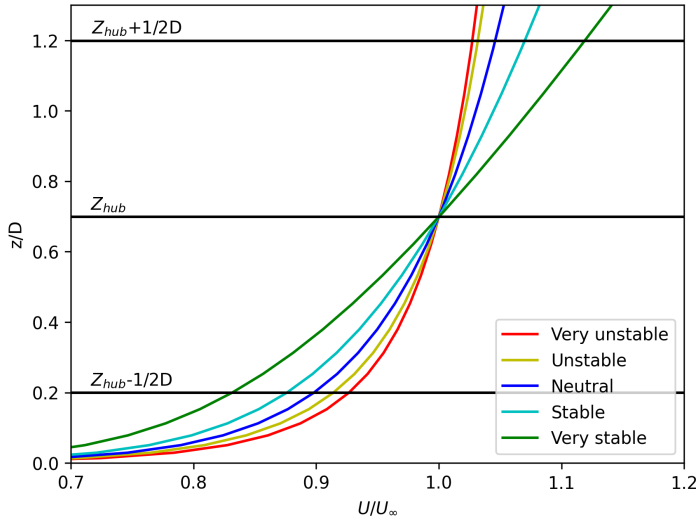

Figure 4.8: Velocity profiles for the 5 stability classes in ORFEUS at X = -59D

Some research questions require the computation of the array efficiency, η_{array}, which expresses the normalized performance of the fully operating farm and is calculated following Segalini's approach [81]:

$$\eta_{array} = \frac{1}{N_t P_{ref}} \sum_{i=1}^{N_t} P_i \tag{4.5}$$

The power curve used for normalising P_{ref}, has to be selected. Figures 4.9 and 4.11 show the normalised power curves for all stability classes over the theoretical power curve, provided by the technical specifications of [15]. While Figures 4.10 and 4.12 show the normalised power curves for all stability classes over the performance of the single turbine and averaged isolated row, respectively, under neutral conditions. ORFEUS is calibrated following Equation 3.16. As no calibration is fully accurate, there is a systematic error in ORFEUS. By normalising over the simulated turbine and averaged isolated row in ORFEUS, the systematic error cancels out. Therefore, the decision was made to select P_{ref} from the single turbine and first row simulations within ORFEUS. The difference in power over changing atmospheric conditions is because freestream velocity profiles vary for every stability class, as previously shown in Figure 4.8.

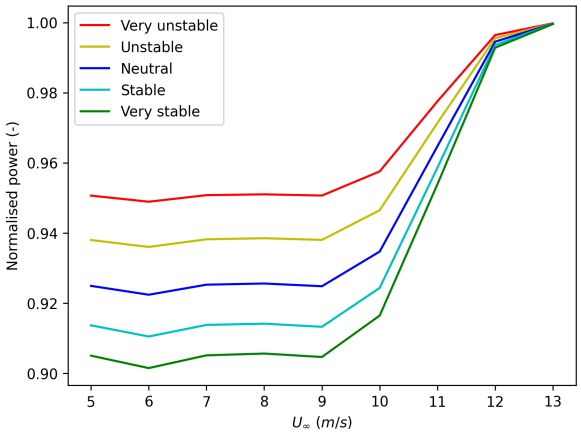

Figure 4.9: The normalised power curve of the averaged first row turbine over P_{ref}, where P_{ref} is the theoretical power curve.

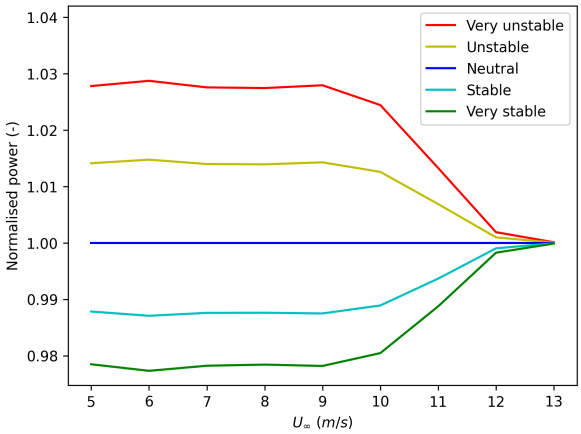

Figure 4.10: The normalised power curve of the averaged first row turbine over P_{ref}, where P_{ref} is the neutral power curve.

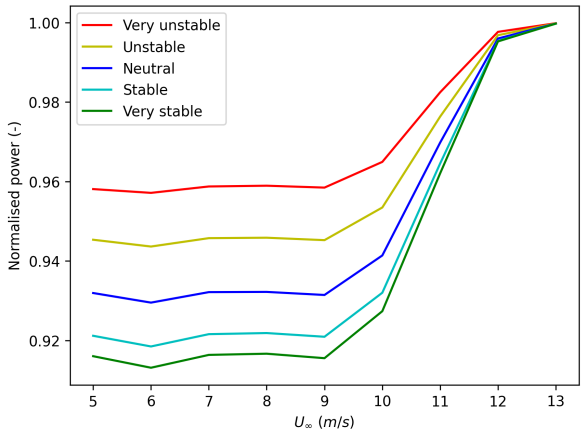

Figure 4.11: The normalised power curve for a single turbine over P_{ref}, where P_{ref} is the neutral power curve.

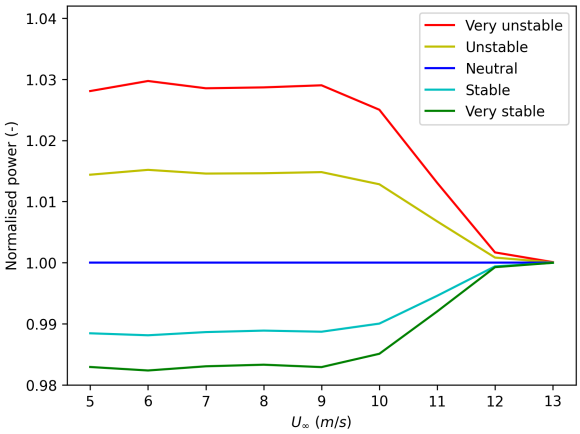

Figure 4.12: The normalised power curve for a single turbine over P_{ref}, where P_{ref} is the theoretical power curve.

Surprisingly, the turbine production decreased with increasing stability, while F. Porté-Agel [32] states that the mean wind speed at hub height often increases with stability. This is explainable by the fact that the stability classes were selected for the reference height, Z_{hub}, meaning that the 5 selected velocity profiles share the same velocity magnitude at Z_{hub}, as Figure 4.13 confirms. The turbine thrust force is calculated by integrating the velocities at all grid points inside the rotor, as stated in Equation 3.15. The area (integral) left of the velocity profile curve within the rotor range in Figure 4.13 becomes smaller with increased stability leading to the decrease in power output of a single turbine as the stability decreases. This difference in the production of a single turbine due to the wind shear is emphasized in Figure 4.13, where the green and red areas indicate the difference in integrated velocity between the very unstable velocity profile and the very stable velocity profile. The green area about equals the red area, which cannot be the cause of the larger production of the freestanding turbine under very unstable conditions. Instead, the non-equispaced grid is a possible cause of the difference in power production, as the density is stronger in both bottom sides of the areas compared to their top sides, leading to a stronger emphasis on the velocity at the bottom of the rotor where the velocities under very unstable conditions dominate, and a lower emphasis on the top side of the rotor where velocities under very stable conditions dominate. This is purely a consequence of the vertical logarithmic computational method of Chebyshev in ORFEUS and should be considered as an error.

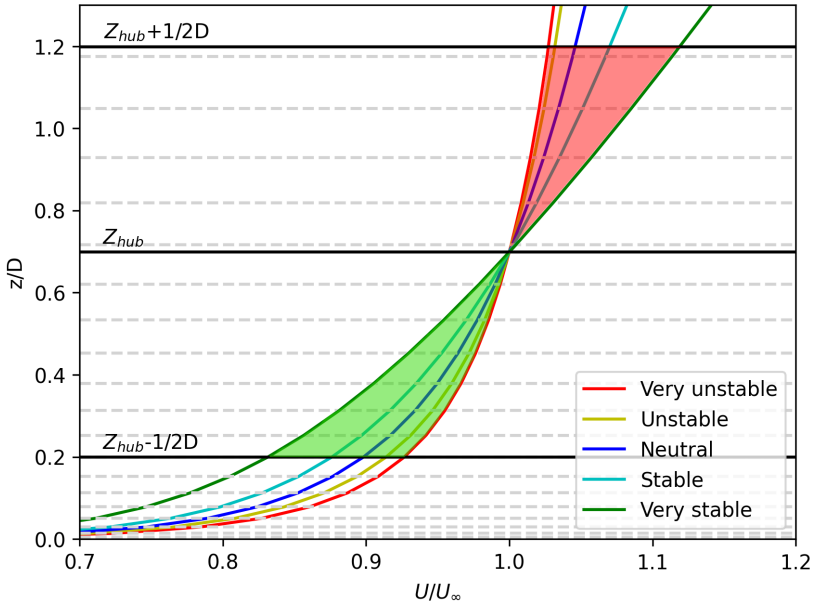

Figure 4.13: Velocity profiles for the 5 stability classes in ORFEUS at X = -59D, with $\int U_{verystable} > \int U_{veryunstable}$ in red and $\int U_{verystable} < \int U_{veryunstable}$ in green.

Equation 4.6 presents the calculation of the number of cases to be run for the 4 setups, further explained in Section 4.4.1.

$$N_{simulations} = N_{setups} \cdot N_{stabilityclasses} \cdot N_{velocities}, \tag{4.6}$$

Where N_{setups} =4 is the number of different farm setups, $N_{stabilityclasses}$ =5 is the number of stability classes, $N_{velocities}$ =16 is the number of velocity bins to be simulated. This leads to a total number of $N_{simulations}$ = 320 simulation cases.

4.4. Quantification of GBE

This section describes how the GBE will be quantified. The section is separated into two Subsections, which both describe a way of quantifying the GBE and will both be applied in this thesis. Subsection 4.4.1 describes the power approach of quantifying the GBE. Subsection 4.4.2 describes the velocity approach of quantifying the GBE.

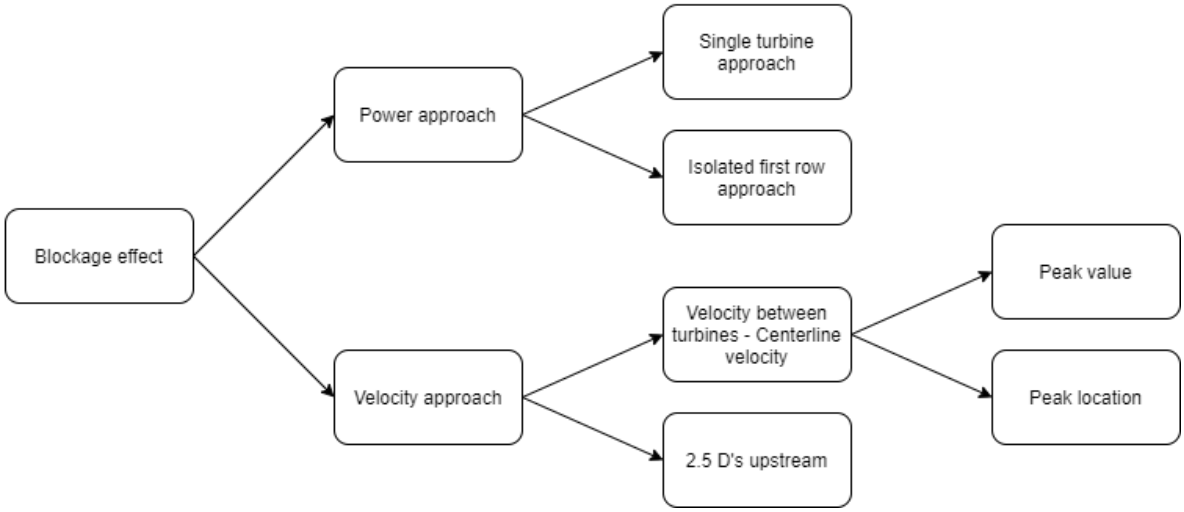

Figure 4.14: Overview of approaches for quantifying the GBE

Figure 4.14 gives an overview of the ways of quantifying the GBE in this thesis. Literature states that an averaged isolated row of turbines outproduces a single turbine [35], due to the Venturi effect. Despite the ”adventage” the isolated row of turbines has over a single turbine, the decision was made to calculate the GBE losses both over a single isolated turbine as well as over an averaged isolated row of turbines. This decision was made because ORFEUS operates with a grid so that a single turbine leads to more uncertainty and dependency on the distribution of the grid points on the single turbine rotor. An entire row leads to more certainty in this regard as more rotors with different grid point distributions are involved.

The velocity approach shown in Figure 4.14 is used as a second approach aimed to find more detailed results on the distribution of the GBE along the first row and its occurrence upstream of the wind farm. The GBE losses are calculated 2.5D upstream, the industry's widely accepted guideline. Apart from the 2.5D value of the GBE losses, the peak in velocity upstream is located.

4.4.1. Power approach of the GBE

The power approach of quantifying the GBE is based on Bleeg's approach [35], which reveals the influence of the GBE on the power production of the first row of turbines by comparing fully operating farm simulations to the freestanding turbine and isolated first row simulations. The GBE based on the power approach will be calculated in two ways.

The first approach of quantifying the GBE loss by power production is done by comparing the first row of a fully operating farm with an identical first row but isolated instead. The GBE can be expressed as an efficiency 2.7 in this thesis however, the GBE is expressed as a loss. Following the First Row (FR) approach, the loss can be expressed as follows,

$$L_{FR,aligned} = 1 - \eta_{GBE,FR} = 1 - \frac{\sum P_{1,aligned}}{\sum P_{1,FR}} \tag{4.7}$$

Where η_{GBE}, is the GBE efficiency. $\sum P_{1,aligned}$ is the sum of the power production of the turbines in the first row of an aligned farm. $\sum P_{1,FR}$ is the sum of the power production of the turbines in an isolated first row simulation.

The second approach of quantifying the GBE loss by power production is done by comparing the average production of the first row of a fully operating farm with the production of a freestanding turbine, called a Single Turbine (ST) in this thesis:

$$L_{ST,aligned} = 1 - \eta_{GBE,ST} = 1 - \frac{\sum P_{1,aligned}/N_{1,t}}{P_{1,ST}} \tag{4.8}$$

Where $N_{1,t}$ is the total number of turbines in the first row, in this case 5, and $P_{1,ST}$ is the power production of a freestanding turbine. When talking about GBE disregarding a specific power calculation approach or farm alignment, the loss is indicated with L_{GBE}, to avoid confusion with the Obukhov parameter, L.

To facilitate both power approaches, three setups need to be run: a fully aligned farm setup, an isolated first row setup and a freestanding turbine setup. A fourth setup is added in the form of a fully staggered farm. Figures 4.15-4.18 show the simulation setups for these four cases, with the first row turbines labelled. The incoming boundary layer follows the streamwise direction, X.

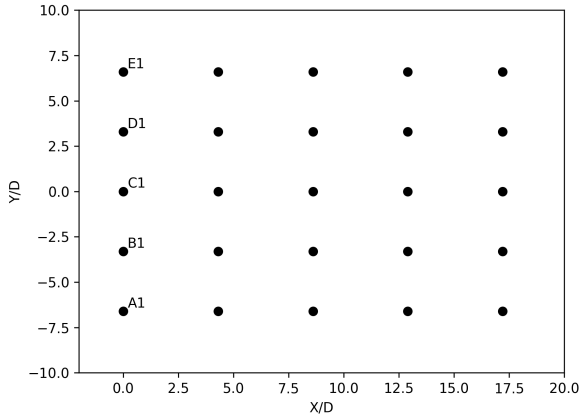

Figure 4.15: Aligned farm layout, in equations referenced to as ”aligned”.

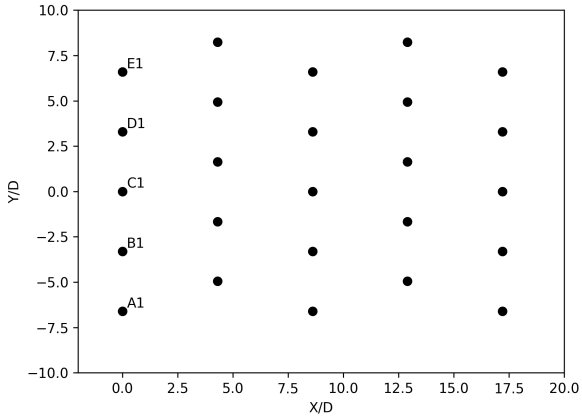

Figure 4.16: Staggered farm layout, in equations referenced to as ”staggered”.

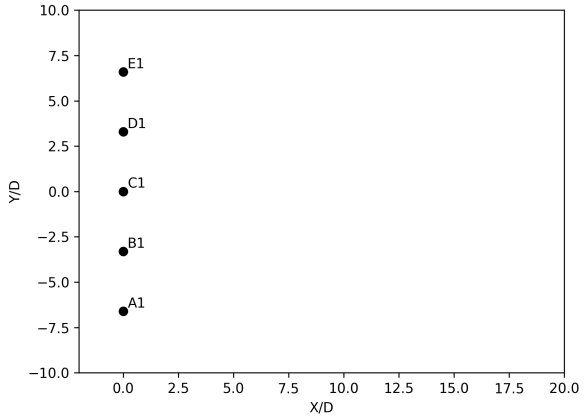

Figure 4.17: First row farm layout, in equations referenced to as ”FR”.

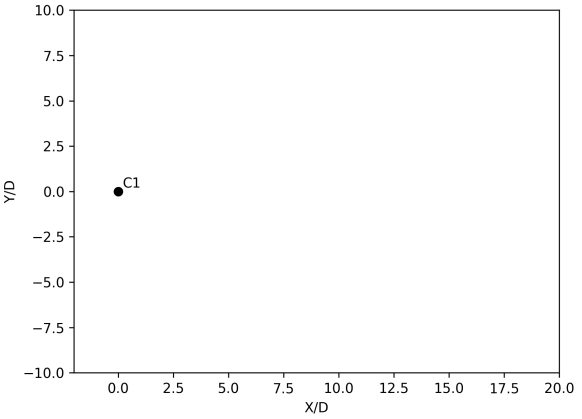

Figure 4.18: Single turbine farm layout, in equations referenced to as ”ST”

4.4.2. Velocity approach of the GBE

A second way of quantifying the GBE is by comparing the upstream velocity directly, rather than by comparing turbine power outputs. This approach offers more freedom of observation of the GBE, as the resolution of this approach follows the grid resolution rather than being bound to the results of the turbines. Through this approach more knowledge on the GBE upstream of the farm is obtained. The GBE behaviour will be looked into by comparing plots of the upstream velocity. From the plots, peak values in GBE can be observed. Industry manufacturers of wind turbines define their power curves with 2.5D upstream velocity measurements, which represents U_∞. This follows the norm set

by International Standard IEC, which states that U_∞ should be measured 2.5D upstream of any wind turbine. The industry standard of looking at the velocity 2.5D upstream will be followed and aside from that the upstream peak value and distance of the GBE will be tracked. The calculation required for this approach is similar to the power approach:

$$p_{FR}(x) = 1 - \frac{U_{aligned}(x)}{U_{ST}(x)} \tag{4.9}$$

Where $U_{aligned}(x)$ is the velocity at distance x upstream of the aligned farm. $U_{ST}(x)$ is the velocity at distance x upstream of the ST. Emmanuel Branlard states [10] that p_{GBE} = 3% of the freestream velocity at hub height 2.5D upstream of a wind farm is easily met.

4.5. Validation

This study was not validated with experimental data, due to the lack of availability of the required data. Instead, the GBE of this thesis is first validated by comparing with an empirical function in Section 4.5.1 and secondly validated by comparing with J. Strickland's LES simulations on the GBE [89] in Section 4.5.2.

4.5.1. Empirical correlation

Equation 4.10 shows A. Segalini's empirical correlation [69] which estimates the decrease in velocity perceived at the farm due to the GBE under neutral conditions in a staggered farm:

$$U(\Delta x = 0) = U_\infty \left\{ 1 - 0.097 \left(\frac{S_x S_y}{D^2} \right)^{-0.9} [1 - \exp(0.88 - 0.88 N_{rows})] \right\} \tag{4.10}$$

Where $U(\Delta x = 0)$ is the perceived velocity at the start of the farm (m/s), U_∞ is the reference velocity (m/s), in this case $U_\infty = U_\infty$. S_x and S_y are the streamwise and spanwise turbine spacings respectively (m), D is the rotor diameter and N_{rows} is the number of rows in the farm. This equation does not include atmospheric conditions, which are assumed to be neutral. With U_∞ = 8 m/s, S_x = 400 m, S_y = 307 m, D = 93 m, N_{rows} = 5 this gives a $U(\Delta x = 0)$ = 7.930812 m/s. This would correspond to a velocity deficit of 0.069188 m/s, which leads to the theoretical power loss due to the GBE of: $L_{GBE} = (1-(\frac{7.930812}{8})^3)\cdot 100$ = 2.57 % power loss. The L_{GBE} = 2.40 % from the First Row results shown in Table 5.2, correspond closely to this L_{GBE} = 2.57 % from the empirical equation.

4.5.2. LES study on the GBE

The second form of validation is by comparing GBE losses from ORFEUS with J. Strickland's LES study on the GBE [89]. During this validation, the GBE is expressed as an efficiency rather than a loss, following J. Stricklands approach as shown in Equation 4.11:

$$\eta_{GBE} = \frac{\sum P_{1,aligned}}{\sum P_{1,infiniterow}} \tag{4.11}$$

New simulations in ORFEUS were run with the computational settings of this thesis, but rather with the turbines used in the LES study placed in an infinite row and farm.

Table 4.9 shows the results of this validation study. Although the results between the simulation in ORFEUS and the LES study seem to be corresponding, the GBE losses in ORFEUS are consistently slightly higher. This might be due to the different way of computing between the LES simulations and ORFEUS. or because ORFEUS is calibrated differently.

Table 4.9: Comparing blockage efficiency with J. Strickland's LES study

Turbine spacing	J. van Til (ORFEUS)	J. Strickland (LES) [89]
sx = 1.96, sy = 1.57[1]	0.914	0.924
sx = 1.96, sy = 1.57[2]	0.932	0.933
sx = 3.93, sy = 1.57[1]	0.948	0.969
sx = 7.85, sy = 1.57[1]	0.976	0.991

[1] Farm size of 8 rows.
[2] Farm size of 4 rows.

5

Results and Discussion

This Chapter presents the obtained results from the simulations performed in ORFEUS, following the described strategy in Chapter 4. The first Section of this Chapter presents results and conclusions on the direct effect of atmospheric stability on the GBE. The following 4 Sections 5.1-5.4 of this Chapter each treat a sub-research question which is repeated in its Section title.‘

Note that ORFUES is a linearised RANS model which does not include a capping inversion, but rather lets the velocity profile go vertically to infinity, following the MOST as explained in Section 2.2.2. As the turbines are located relatively close to the ground, and the velocity profiles correspond well at these heights, this is not seen as an obstacle. Yet and still, one needs to take into account that the capping effect of the capping inversion and the Free Atmosphere (FA) stability are not included.

5.1. *Relation between the freestream wind speed and the GBE*

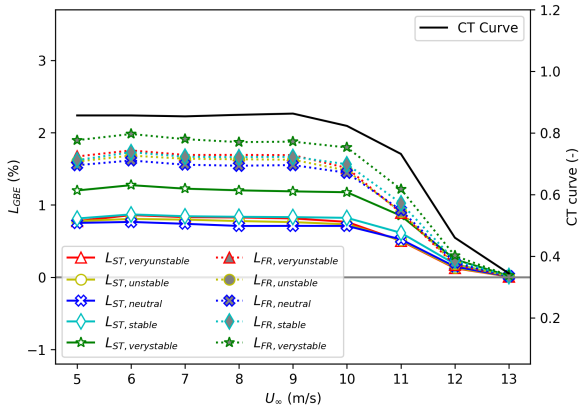

Figure 5.1: U_∞-$L_{aligned}$

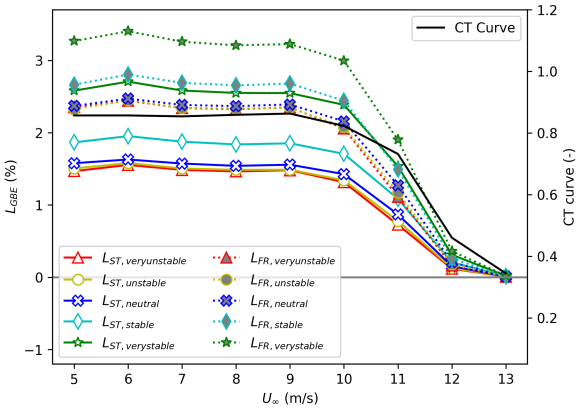

Figure 5.2: U_∞-$L_{staggered}$

Figure 5.1 plots L_{GBE}, computed with Equations 4.7 and 4.8, over U_∞ for all 5 stability classes, calculated both through the First Row and Single Turbine approach for the aligned farm, as explained in Section 4.4.1. Figure 5.2 plots the L_{GBE} for the staggered farm. L_{GBE} values at wind speeds $U_\infty = 3$m/s and $U_\infty = 4$m/s are left out of Figures 5.1 and 5.2 as values of U_∞ this close to the cut-in speed resulted in the first row of the fully operating farm to be completely turned off, due to the GBE, leading to extreme values of L_{GBE}. L_{GBE} values above 13 m/s remained 0% for all scenario's and are cut off from the plots. Appendix E reveals the complete GBE loss results, including the obtained values for $U_\infty = 3$ m/s, $U_\infty = 4$ m/s and $U_\infty > 13$ m/s.

From Figure 5.1 and 4.8 one can observe that the GBE increases with more stable atmospheric conditions. This agrees with J. Schneemann's conclusion in his research on the GBE and

atmospheric stability [59], in which he states that increased convection, which is the case for unstable conditions, cancels out the GBE, due to the vertical transport of momentum. In other words, the more dynamic air at unstable atmospheric conditions leads to faster recovery of the disturbed air and thereby a lower pressure field for the farm as a whole, leading to lower GBE losses.

Figures 5.1 and 5.2 show that there is a shift in magnitude of the L_{GBE} calculated by the First Row power approach and the Single Turbine power approach, where the Single Turbine power approach shows a smaller L_{GBE}, $L_{FR} > L_{ST}$. Comparing the two approaches following Equations 4.7 and 4.8 reveal that the average production of the 5 turbines in the First Row simulation produce more than the turbine from the Single Turbine simulation. A. R. Meyer Forsting [33], S. McTavish [90] and J. Strickland [36] show that there is a channelling effect between turbines, due to the Venturi effect, which would decrease the GBE. J. Bleeg's research [35] shows that a row of 5 turbines with a $s_y = 3.0$D, produce 0.57% more energy than a single freestanding turbine.

This Venturi effect is also a possible explanation for the fact that the L_{GBE} among different atmospheric conditions seem to deviate more for the First Row simulations compared to the Single Turbine simulations, especially for less stable conditions. The Single Turbine results in a more consistent L_{GBE} for all wind speeds, in that way.

As the L_{GBE} for all atmospheric conditions converge to 0% at 13 m/s, and as the more stable cases have a higher L_{GBE}, these cases also show the biggest shrink in the L_{GBE} curve. While more stable cases show less of a jump towards the 13 m/s mark.

Region 2 of the power curve reaches up to 13 m/s as previously shown in Figure 2.11. Figures 5.1 and 5.2 show that the GBE is only present in region 2 of the power curve. The Ct curves plotted in the L_{GBE} plots of Figure 5.1 and 5.2, show that, for every stability class, the L_{GBE} follows the course of the Ct curve. Where the L_{GBE} converges to 0 at the end of region 2, the Ct curve does not. The plot does not show region 3 in which the Ct curve keeps decreasing while the L_{GBE} remains 0. The L_{GBE} curves follow the same horizontal slope for all wind speeds in Region 2, regardless of the atmospheric stability. Following this observation one can conclude that the atmospheric stability does not influence the relation between freestream wind speed and GBE.

5.2. *Farm alignment and power output*

This Section is divided into 3 Subsections. The sub-research question described in this Sections is treated in the first two Subsections. While the last Subsection aims to decompose the total turbine interaction losses into GBE losses and wake losses.

5.2.1. Power output

Based on the fact that the performance of a single turbine decreases with increasing stability conditions, as concluded previously from Figure 4.13, one would expect an identical behaviour for a fully operating farm. On top of that, wakes recover faster at unstable conditions, meaning longitudinally aligned turbines behind the first row receive wind that is recovered better and therefore perform better under unstable conditions compared to stable conditions. This would lead to an even bigger difference in performance at stable conditions. Tables 5.1 and 5.2 show the power output of the fully operating farm for every atmospheric stability class at U_∞= 8 m/s. With those outputs, η_{array} was calculated, following Equation 4.5. Tables 5.1 and 5.2 show that the production of a fully operating farm, and with that η_{array}, decreases with increasing atmospheric stability.

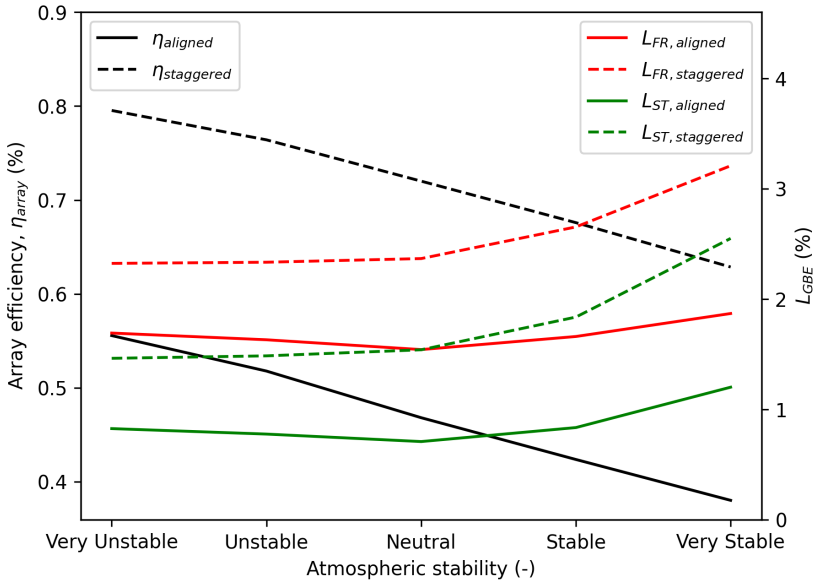

Figure 5.3: η_{array} and L_{GBE} over atmospheric stability at U_∞= 8m/s

With decreasing power output and η_{array} one would expect a decreasing GBE, as less power is extracted from the wind, which would lead to the farm being less of an obstacle. The results show the opposite, where the production of the farm decreases with stability, L_{GBE} increases. Figure 5.3 shows this, with a linearly decreasing η_{array} and an increasingly growing L_{GBE} over atmospheric stability, which is confirmed by Tables 5.1 and 5.2. A more stable atmosphere leads to slower wake recovery and therefore a lower array efficiency of the farm. While a more stable atmosphere creates a higher GBE due to the lower mixing length of disturbed air, leading to a higher pressure field of the farm and with that higher a L_{GBE}. The increase in L_{GBE} can only be partly accountable for the decrease in farm production, as the magnitude of the decrease in array efficiency outweighs the increased L_{GBE}.

5.2.2. Farm alignment

Table 5.1: Power output (U_∞ = 8 m/s), η_{array} (U_∞ = 8 m/s) and averaged (U_∞ = 5 to 9 m/s) GBE loss for the aligned farm

Stability Class	Aligned (kW)	η_{array}	L_{FR}	L_{ST}
Very Unstable	11834.5	0.556	1.70	0.822
Unstable	11029.7	0.518	1.64	0.784
Neutral	9971.36	0.468	1.56	0.735
Stable	9023.43	0.424	1.67	0.839
Very Stable	8096.63	0.38	1.91	1.22

Table 5.2: Power output (U_∞ = 8 m/s), η_{array} (U_∞ = 8 m/s) and averaged (U_∞ = 5 to 9 m/s) GBE loss for the staggered farm

Stability Class	Staggered (kW)	η_{array}	L_{FR}	L_{ST}
Very Unstable	16942.2	0.795	2.36	1.49
Unstable	16275.9	0.764	2.36	1.51
Neutral	15338.6	0.720	2.40	1.58
Stable	14396.8	0.676	2.70	1.88
Very Stable	13390.3	0.629	3.27	2.59

Tables 5.1 and 5.2 present η_{array} together with the average L_{GBE} between U_∞= 5 and 9 m/s, in which L_{GBE} remains constant over U_∞ for every atmospheric stability. From Tables 5.1 and 5.2 and from Figures 5.4-5.7 one can conclude that the GBE at a staggered farm is dominant over the GBE at an aligned farm. This is expected as the staggered layout implies a more blocking layout compared to the aligned layout.

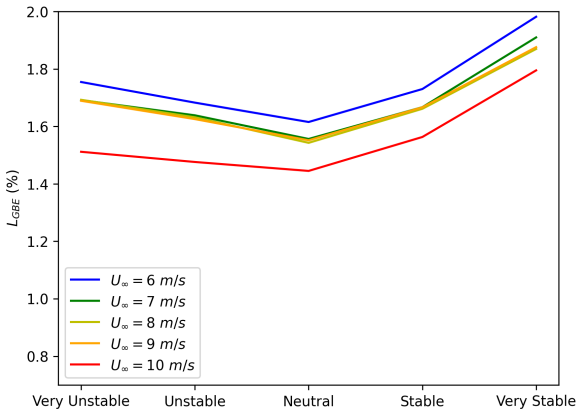

Figure 5.4: $L_{FR,aligned}$ over stability for different U_∞.

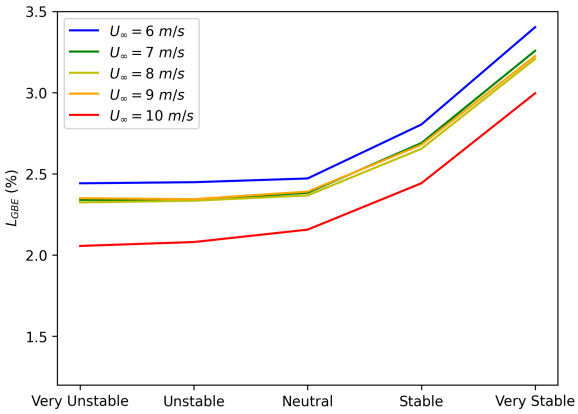

Figure 5.5: $L_{FR,staggered}$ over stability for different U_∞.

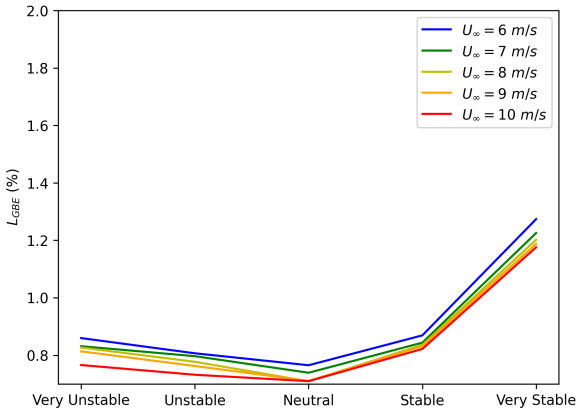

Figure 5.6: $L_{ST,aligned}$ over stability for different U_∞.

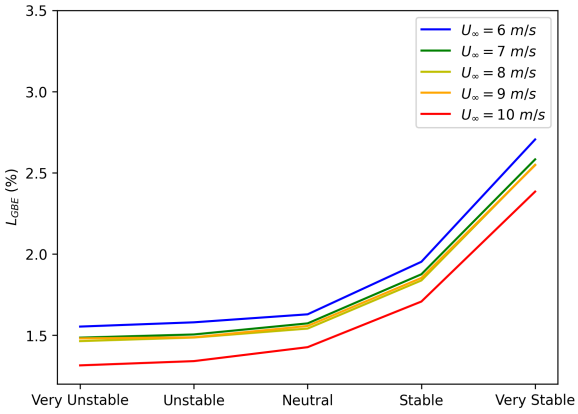

Figure 5.7: $L_{ST,staggered}$ over stability for different U_∞.

Figures 5.4-5.7 show that L_{GBE} peaks towards very stable conditions. $L_{aligned}$ is the lowest under neutral conditions, while $L_{staggered}$ is the lowest under very unstable conditions. Two effects possibly explain the $L_{veryunstable} > L_{neutral}$ in the aligned farm.

The first explanation is that the turbines are streamwise closer aligned in the aligned farm than in the staggered farm. Smaller spacing between turbines means less time for their wakes to recover between the turbines. As wakes in unstable conditions recover faster compared to wakes in neutral conditions, the laterally aligned turbines behind the first row are able to produce more power under unstable conditions and thereby create a higher array efficiency which leads to a larger GBE.

The second explanation is that in the aligned farm, the open spaces between the turbines in the lateral direction throughout the entire length of the farm give the opportunity for airflow to pass ”freely” through the wind farm, with help of the Venturi effect. While under unstable conditions there is increased turbulence, leading to less ease for airflows to freely pass through the farm compared to neutral conditions. This effect is more present in the aligned farm as a staggered farm does not facilitate the passing of airflows as much as an aligned farm. This effect can be observed in Figure 5.13.

5.2.3. Wake losses and GBE losses

η_{array} is the calculated farm performance by a reference turbine, in this case, the neutral single turbine. In order to separate the wake losses and GBE losses for every stability class, the farm should be normalised over a single turbine operating at identical operating stability conditions. Consider no wake and GBE losses. The power of every wind turbine in a wind farm would theoretically be identical. The wake losses can be determined by subtracting a theoretical optimal farm without losses by the GBE losses as shown in Equations 5.1 and 5.2.

$$\frac{1}{N_t P_{\infty,k}} \sum_{i=1}^{N_t} P_{i,k} = 1 - L_{GBE} - Lwake \tag{5.1}$$

$$L_{wake} = 1 - \frac{1}{N_t P_{\infty,k}} \sum_{i=1}^{N_t} P_{i,k} - L_{GBE} \tag{5.2}$$

where L_{wake} are the wake losses (%) and k is the specific stability class. This led to the values plotted in Figures 5.9 - 5.10. Figure 5.9 shows the linear increase in wake effects with increasing atmospheric stability. Even though L_{GBE} grows increasingly with increasing stability, its impact is highest under very unstable conditions, as can be concluded from Figure 5.10, due to the low impact of the wake losses. Due to the magnitude and constant growth of L_{wake} which outweigh L_{GBE}, the impact of the GBE on the total loss decreases with increasing stability conditions.

The aligned farm shows relatively high L_{wake} and L_{GBE}, compared to the staggered farm which shows lower L_{wake} and higher L_{GBE}. This is in line with expectations and previous conclusions, as an aligned farm has smaller streamwise turbine spacing compared to a staggered farm, meaning turbines suffer more from turbine wakes, resulting in a smaller L_{wake}. The staggered farm extracts more energy from the wind and has a more optimal blocking layout leading to higher L_{GBE}. Figure 5.8 shows the distribution of the ratio of GBE at a staggered farm compared to that under the same conditions at an aligned farm.

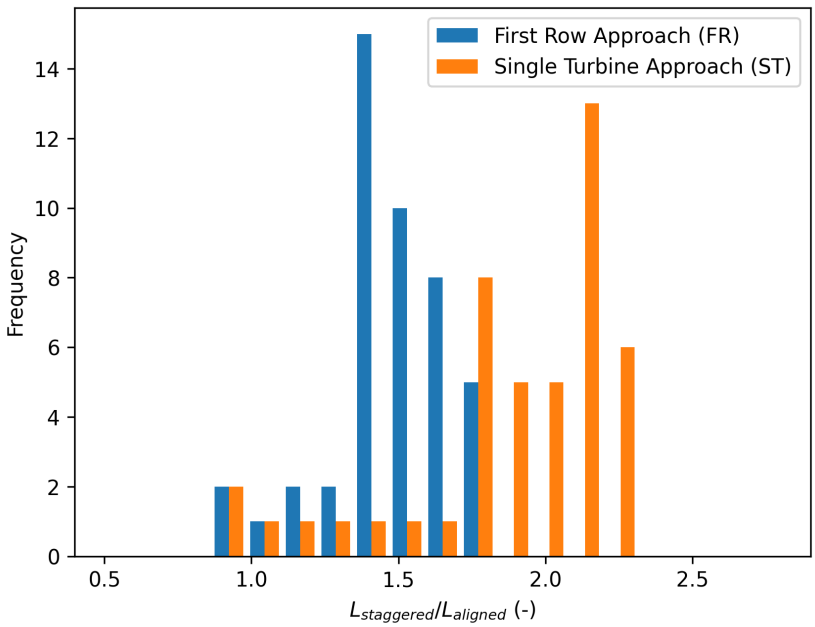

Figure 5.8: Distribution of magnitude of GBE losses at the staggered farm compared to the aligned farm.

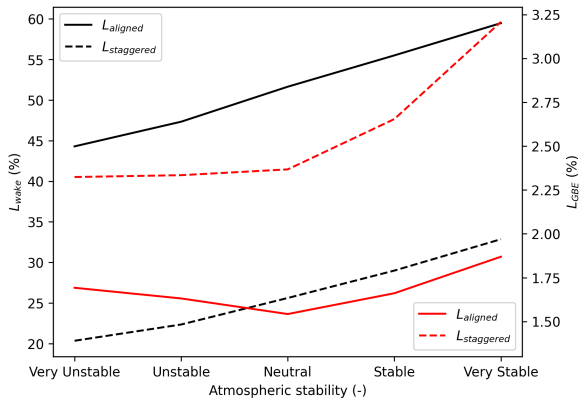

Figure 5.9: Wake loss (black) and GBE loss (red) over atmospheric stability at U_∞ = 8 m/s

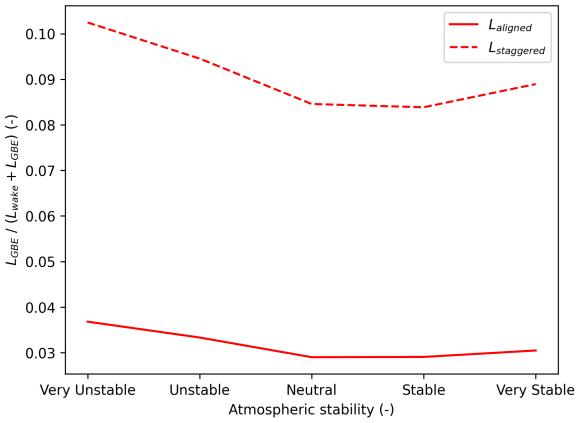

Figure 5.10: Loss distribution per atmospheric stability at U_∞ = 8 m/s

Figure 5.10 shows the share of the wake losses to the total losses for both farm setups. The highest contribution of L_{GBE} was found with a total contribution of ≈ 10% of the losses in the wind farm, in a staggered farm under unstable conditions. While the lowest contribution of L_{GBE} was present in the aligned farm under neutral conditions and was ≈ 3%.

5.3. *Power and GBE behaviour along the first row*

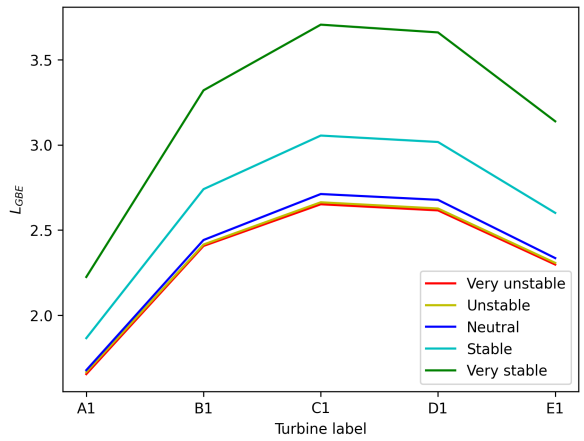

Figure 5.11: L_{GBE} along the first row of a staggered farm

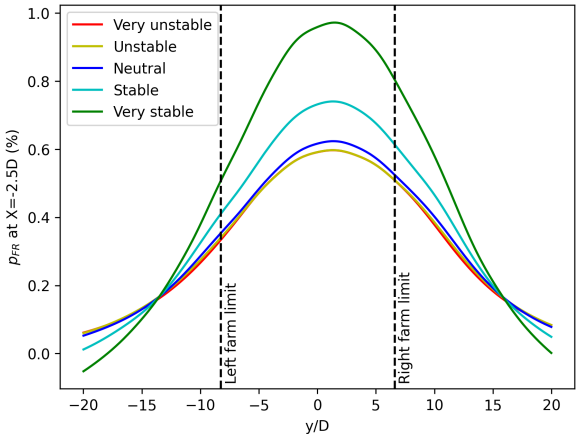

Figure 5.12: Velocity deficit due to GBE, p_{GBE}, along the first row of a staggered farm

Figure 5.11 plots the L_{GBE} calculated for every turbine individually in the first row. As the results for the aligned farm and staggered farm showed similar effects regarding the behaviour of the GBE along the first row, and as the farm alignment is not included in this sub-research question, only the staggered farm is discussed. The curve is not symmetrical because, unlike the aligned farm, the staggered farm is asymmetrical. A clear peak in L_{GBE} can be seen at the centre turbine L_{GBE}, which agrees with conclusions by A. Segalini in [69]. The peak in L_{GBE} at the centre can be explained by the fact that the edges of the farm have more freedom for airflow to pass around the farm and are therefore less blocked compared to the airflow towards the centre of the farm.

The gradient effect of L_{GBE} along the first row scales with stability, meaning that L_{GBE} towards the edge turbines differs less over varying atmospheric stability compared to the turbines located towards the centre. Figure 5.12 plots $p_{FR}(X = -2.5D)$ of the staggered farm, as defined in Equation 4.9. A similar curve of the GBE along the first row can be seen as in Figure 5.11. This dependency of the atmospheric

stability is in line with previous results of the GBE under changing atmospheric conditions, where very stable conditions seem to be more affected due to larger Prandtl's mixing length higher pressure field of the farm, as explained in Sections 3.1 and 5.1.

5.4. *Extent and magnitude of upstream velocity loss due to the GBE*

Figure 5.13 shows the velocity development in front of and through the wind farm. U_c indicates the velocity development at the centreline of the centre front turbine, while U_{mid} indicates the velocity development spanwise midway (Y = 0.5 sy) between two turbines. Figure 5.14 shows the same values but zoomed in on the velocity development in front of the farm. It is challenging to make a quantitative separation between the local and global blockage effect. One can make a rough estimate of the separation between local and global blockage effect by assuming that the wind in front of the centre of a first row turbine of a farm is affected by both local and global blockage effect, while a turbine midway (laterally) between two first row turbines of a farm are only affected by the global blockage effect of the farm. The values for U_{mid} and U_{centre} are plotted in Figures 5.13 and 5.14, where U_{centre} contains both the local and global blockage effect and U_{mid} only contains the local blockage effect. One might say that the boundary between the local and global blockage effects can be found when the two curves separate at $X \approx 3D$, as shown in Figure 5.14. However, this should be rather seen as an indicator than as a rule, as 1) there is room for interpretation when quantitatively deciding on the point of separation of the two curves and 2) as velocities at U_{mid} are not purely affected by the global blockage effect, but also by the local blockage effect of the front turbines close by, which do not only develop in the streamwise direction.

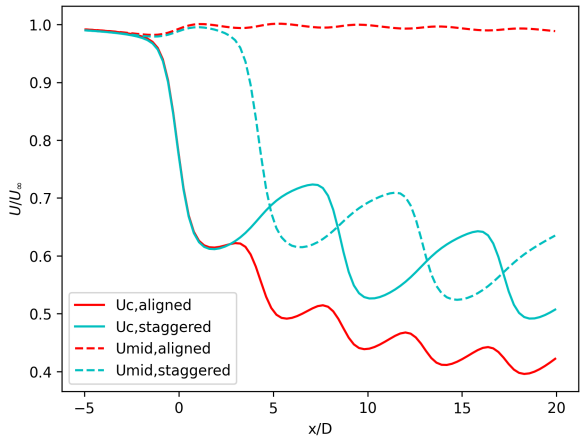

Figure 5.13: Neutral conditions at U_∞ = 8 m/s

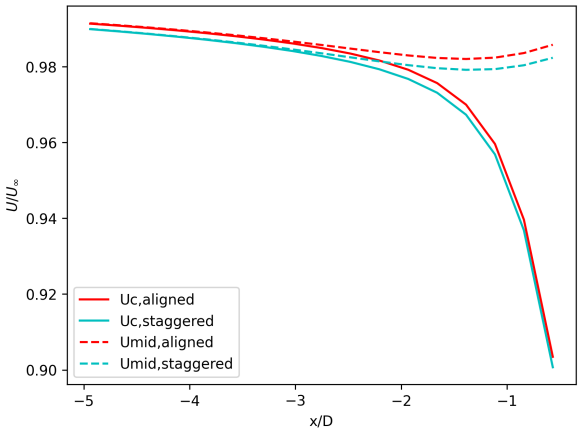

Figure 5.14: Neutral conditions at U_∞ = 8 m/s

From Figures 5.15 and 5.16 one can observe the decreased upstream wind speed because of the loss in velocity, p_{GBE}, defined in Equation 4.9. Figure 5.16 plots the 2.5D line upstream of the wind farm, taken as a reference for p_{GBE} by the industry. The peaks in p_{GBE} will be denoted as p_{max} which occur X_{max} upstream of the farm and are indicated by an "X" in Figure 5.16. A clear increase in p_{max} can be seen the more stable the atmosphere is. Furthermore, a more unstable atmosphere leads to a lower $|X_{max}|$, meaning that the peak in upstream velocity deficit due to the GBE effect is located closer to the wind farm. A possible explanation for this is that displaced air parcels in unstable atmospheric conditions restore their initial position easier than in stable atmospheric conditions, as explained in Section 2.2. This ease of displacement of parcels leads to shorter wake recoveries and with that to faster wake recoveries and possibly the smaller $|X_{max}|$ under unstable conditions. This agrees with the earlier explanation made in Section 5.1. The unstable air leads to increased (faster) vertical mixing of disturbed air, not only at the back (wake side) of the turbines but also on the front side of the turbines, leading to a shift of the GBE towards the farm and a decreased magnitude of the GBE.

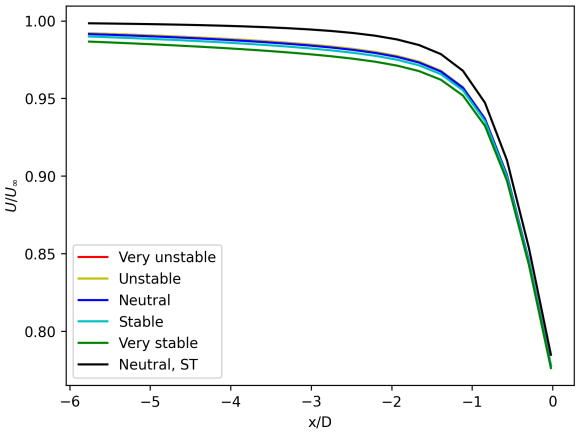

Figure 5.15: Normalized upstream velocity of the staggered farm at U_∞ = 8 m/s

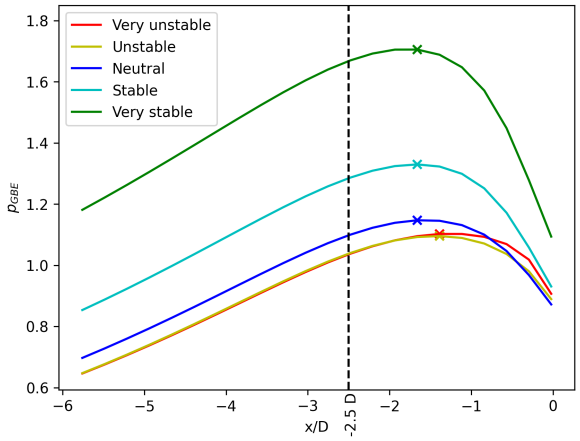

Figure 5.16: $p_{staggered}(X)$ at U_∞ = 8 m/s

Table 5.3: Peaks of $p_{staggered}(X)$ in upstream velocity

Stability class	$p_{-2.5D}$ (m/s)	p_{max} (m/s)	X_{max} (x/D)
Very Unstable	1.04	1.10	-1.39
Unstable	1.04	1.10	-1.39
Neutral	1.10	1.15	-1.66
Stable	1.29	1.33	-1.66
Very Stable	1.67	1.71	-1.66

Table 5.3 shows the peak value and distance upstream, p_{max} (D), of the p_{GBE}(X) plot of Figure 5.15. Table 5.3 confirms the earlier results from Figure 5.15 that more unstable conditions lead to a peak in velocity deficit closer to the wind farm. Taking the 2.5D instead of the peak value of p_{GBE} would lead in this case to an offset in the quantification of the velocity loss due to the GBE of 2.33-5.45%. There are critics on the assumption by the IEC protocol [66] that at an upstream distance of X=2.5D there are no local blockage effects present [10]. When quantifying or measuring the GBE at a certain distance from the farm, one should keep in mind that the GBE might peak at a different upstream distance depending on the stability. Knowing that the peak in velocity deficit due to the GBE depends on the atmospheric conditions might be interesting for the wind industry:

1. To know the varying location of the peak in GBE might be interesting for wind farm developers, as existing or planned structures in front of the wind farm are impacted by the GBE and knowing the peak at every atmospheric stability in combination with a stability distribution can improve predictions of the affected structures.

2. When creating an empirical function to predict the GBE, the peak and course of the velocity deficit due to the GBE have to be included. Knowing the dependency on the atmospheric conditions is key.

p_{max} in Table 5.3 follows the grid step size from the simulation. As the velocity is calculated at every grid point in ORFEUS, the gradient in the occurrence of the peak is discontinuous.

6

Conclusions

This chapter presents the main conclusions on the research question: *"How does atmospheric stability affect the global blockage effect?"*. With the goal of tackling this research question and its sub-research questions, simulations were run on a theoretical farm in the linearised RANS modelling software, ORFEUS. A 5 by 5 perfectly aligned farm and a 5 by 5 staggered farm were investigated under different stability conditions and varying incoming wind speeds, in order to find out the influence of these varying inputs on the impact of atmospheric stability on the GBE. The GBE was observed both by looking at the difference in generated power by the wind turbines on the first row of the farm, in order to investigate the influence of the GBE on the production. As well as by comparing the incoming velocity intensity upstream of the farm, to obtain more insight on the cause of the GBE.

Keep in mind that linearised RANS models are simplified models and are limited in their computational accuracy. The results in this study are not compared to experimental data, so can only function as a reference and setup for further research on how the Global Blockage Effect (GBE) behaves under different atmospheric conditions. Remember that the capping inversion is not implemented in the linearised RANS model. Due to the lack of capping inversion and the velocity profile not being extrapolated to the top, but rather running infinitely high, the flow around the farm behaved differently. Developments in this thesis ignore the turning effects of the Coriolis forces as well as buoyancy forces.

The Chapter is split into 2 Sections. Section 6.1 provides the conclusions from this thesis project, followed by Section 6.2 presenting recommendations for further research.

6.1. Conclusions

The GBE loss, L_{GBE}, was found to be only present in region 2 of the power curve, where it follows the slope of the Ct curve, but converges to zero at the end of Region 2, where the Ct curve does not. When Ct stayed constant, L_{GBE} seemed to be independent of the wind speed for all simulated cases.

The farm produced less power at more stable conditions, which was explained by the similar behaviour of a single turbine along changing atmospheric conditions. The behaviour of the single turbine was explained by the upstream velocity profile and the selected atmospheric condition settings. Where η_{array} of the farm decreased with stability, L_{GBE} increased with stability, which was concluded to not be a cause of the η_{array} decrease.

The difference in results between the calculation of L_{GBE} through an isolated first row or through a single turbine was explained by the Venturi effect which caused the turbines in the isolated first row to produce more power compared to the single freestanding turbine.

Farm alignment had an impact on the influence of atmospheric stability on the GBE. For both the aligned farm and the staggered farm, L_{GBE} showed an increasing growth from very unstable to very

stable conditions, whereas the staggered farm showed a sharper increase than the aligned farm. The aligned farm showed a smaller L_{GBE}, and with that less sensitivity to atmospheric conditions compared to the staggered farm. L_{GBE} of the aligned farm had its minimum at neutral conditions, while the staggered farm had its minimum of L_{GBE} under very unstable conditions. This difference of impact of the atmospheric stability on the L_{GBE} depending on the farm alignment was explained by a different reaction of the wake recovery and Venturi effects related to the farm alignment with changing stability.

The total farm loss was separated into wake losses, L_{wake} and L_{GBE}. L_{wake} outweighed L_{GBE} as expected. L_{wake} showed a continuous growth over atmospheric stability. While L_{GBE} was highest at very stable conditions, the relative L_{GBE} over the total losses was found at very unstable conditions, as the increase in L_{wake} over stability out-scaled the growth of L_{GBE} over stability. The aligned farm had a contribution of L_{GBE} to the total losses of 3-4%, while the staggered farm contributed for 8-11%. The contribution of the L_{GBE} to the total losses did not show an increase or decrease over atmospheric stability.

As expected, there is a variation of the GBE losses along the first row of the wind farm, where the centre of the farm impede a higher L_{GBE}, compared to the edge of the farm. The magnitude of this gradient in L_{GBE} is dependent on atmospheric stability. Where stable conditions lead to a stronger gradient between centre and edge turbines. This course of the GBE losses along the first row and the sensibility of that course to the atmospheric conditions was confirmed by looking at the velocity behaviour and explained by the fact that stable conditions are more affected by the GBE

On top of that, the peak in the upstream velocity deficit due to the GBE was tracked for all stability classes. The upstream distance of the peak of velocity deficit ranged between 1.66-2.21D upstream of the staggered farm, closer than the 2.5D the industry assumes. The magnitude of this peak stayed constant between very unstable and neutral conditions. Under stable and very stable conditions, there was a significant increase in velocity deficit compared to the other stability classes.

L_{GBE} for the 5 different stability classes ranged between 1.56% - 1.91% in the perfectly aligned 5 by 5 farm, while ranging between 2.36% - 3.27% in the staggered 5 by 5 farm. It was concluded that the magnitude of L_{GBE} was dependent on atmospheric stability and specifically strongly reactive to stable conditions. L_{GBE} was highest under very stable conditions, while relative to the total farm losses, L_{GBE} was highest under very unstable atmospheric conditions.

The goal was to increase the general knowledge about the behaviour of the GBE, on this occasion, specifically under different atmospheric conditions. Repeating the main findings in this thesis, increasing atmospheric stability seemed to:

- decrease farm production and, η_{array}
- increase the L_{GBE}
- not impact a possible dependency of the GBE on C_t, which was nonexistent, but rather a possible dependence on the Ct curve was found.
- impact farm alignment influence on the GBE.
- increase L_{wake}
- decrease L_{GBE}/L_{total}
- increase distance between the farm and the upstream peak in velocity deficit due to the GBE

The results and ORFEUS' performance were validated both by an empirical function and by comparing with J. Strickland's LES study on the GBE [89].

6.2. Recommendations

To enable the continuation of the general knowledge and understanding of the GBE, and to reach an agreement in more extensive guidelines regarding the GBE, the following recommendations were made:

- Pursue validation of the influence of atmospheric stability on the GBE and expand the research on existing wind farms.
- Include the dependency of atmospheric conditions on the surface roughness, z_0, and its influence on the GBE for offshore wind farms.
- Look at the behaviour of atmospheric conditions at bigger sized wind farms (mammoth farms).
- Investigate the location of the peak in GBE and the impact of the GBE on the power curve, measured at 2.5D upstream.
- More in-depth research on separation of GBE losses and wake losses, and their correlation.
- Ultimately, formulate an algebraic equation to predict and quantify the GBE for wind farm designs, including all impacting parameters on the GBE.

This thesis project agrees with the conclusion of J. Schneemann [59] that the GBE depends on atmospheric stability. As well as with the statement of M. Popescu [91] that the extent and strength of the GBE depend on the farm layout, turbulence (atmospheric stability) and thrust coefficient. The parameters of possible influence in the same statement, which were not included in this thesis project, were the dependency of GBE on the wind-farm size, wind direction and turbine spacing.

Appendices

Appendix A - DoE upstream reflections study

This Appendix Chapter shows the complete Design of Experiments (DoE). Every table represents a series of simulations in which one single parameter is varying in order to find its influence on the upstream reflections, as discussed in Section 4.2.2. Note that, after finding the desired fringe intensity in Table 4, the desired value of 1.2 was assumed for the rest of this study.

Table 1: Simulation configuration extending the fringe length (with a constant fringe start)

Fringe start [m]	Fringe end [m]	Ymin [m]	Ymax [m]
5000	11000	-7000	7000
5000	14000	-7000	7000
5000	17000	-7000	7000
5000	20000	-7000	7000
5000	23000	-7000	7000

Table 2: Simulation configuration extending the start of the fringe region (with a constant fringe length)

Fringe start [m]	Fringe end [m]	Ymin [m]	Ymax [m]
5000	15000	-7000	7000
7000	17000	-7000	7000
9000	19000	-7000	7000
11000	21000	-7000	7000
13000	23000	-7000	7000

Table 3: Simulation configuration extending start fringe region (i.e. a constant fringe ending)

Fringe start [m]	Fringe end [m]	Ymin [m]	Ymax [m]
5000	23000	-7000	7000
7000	23000	-7000	7000
9000	23000	-7000	7000
11000	23000	-7000	7000
13000	23000	-7000	7000

Table 4: Simulation configuration extending the fringe intensity

Fringe start [m]	Fringe end [m]	Ymin [m]	Ymax [m]	Fringe Intensity
7000	23000	-7000	7000	0.9
7000	23000	-7000	7000	1
7000	23000	-7000	7000	1.1
7000	23000	-7000	7000	1.2
7000	23000	-7000	7000	1.3

Table 5: Simulation configuration extending the domain start

Fringe start [m]	Fringe end [m]	Ymin [m]	Ymax [m]	Fringe Intensity	domain start [m]
7000	23000	-7000	7000	1.2	-4000
7000	23000	-7000	7000	1.2	-6000
7000	23000	-7000	7000	1.2	-8000
7000	23000	-7000	7000	1.2	-10000
7000	23000	-7000	7000	1.2	-12000

Table 6: Simulation configuration extending the spanwise domain

Fringe start [m]	Fringe end [m]	Ymin [m]	Ymax [m]
5000	23000	-7000	7000
5000	23000	-9000	9000
5000	23000	-11000	11000
5000	23000	-13000	13000
5000	23000	-15000	15000

Table 7: Simulation configuration extending the vertical domain

Fringe start [m]	Fringe end [m]	Ymin [m]	Ymax [m]	Fringe Intensity	Zmax [m]
7000	23000	-7000	7000	1	1000
7000	23000	-7000	7000	1	2000
7000	23000	-7000	7000	1	3000
7000	23000	-7000	7000	1	4000
7000	23000	-7000	7000	1	5000

Table 8: Simulation configuration extending the turbine delta parameter

Fringe start [m]	Fringe end [m]	Ymin [m]	Ymax [m]	Fringe Intensity	Sigma
7000	23000	-7000	7000	1.2	30
7000	23000	-7000	7000	1.2	50
7000	23000	-7000	7000	1.2	70
7000	23000	-7000	7000	1.2	90
7000	23000	-7000	7000	1.2	110

Table 9: Simulation configuration extending Nz

Fringe start [m]	Fringe end [m]	Ymin [m]	Ymax [m]	Fringe Intensity	Nz
7000	23000	-7000	7000	1.2	30
7000	23000	-7000	7000	1.2	40
7000	23000	-7000	7000	1.2	50
7000	23000	-7000	7000	1.2	60
7000	23000	-7000	7000	1.2	70

Table 10: Simulation configuration extending Nx and Ny

Fringe start [m]	Fringe end [m]	Ymin [m]	Ymax [m]	Fringe Intensity	Nx	Ny
7000	23000	-7000	7000	1.2	64	64
7000	23000	-7000	7000	1.2	128	128
7000	23000	-7000	7000	1.2	256	256
7000	23000	-7000	7000	1.2	512	512
7000	23000	-7000	7000	1.2	1028	1028

Table 11: Simulation configuration extending the surface roughness (not computational)

Fringe start [m]	Fringe end [m]	Ymin [m]	Ymax [m]	Fringe Intensity	Z0 [m]
7000	23000	-7000	7000	1	0.0001
7000	23000	-7000	7000	1	0.0002
7000	23000	-7000	7000	1	0.001
7000	23000	-7000	7000	1	0.005
7000	23000	-7000	7000	1	0.01

Appendix B - Upstream reflections study

This Appendix Chapter presents the colour plots of the farm before the upstream reflections study and after the upstream reflections study. Note that the colour plots for all previously named parameters in Appendix 6.2 has been created but are not included in this Appendix for the sake of clarity and structure. Also, note that the results for the very stable conditions are missing as they are included in the text in Section 4.2.2.

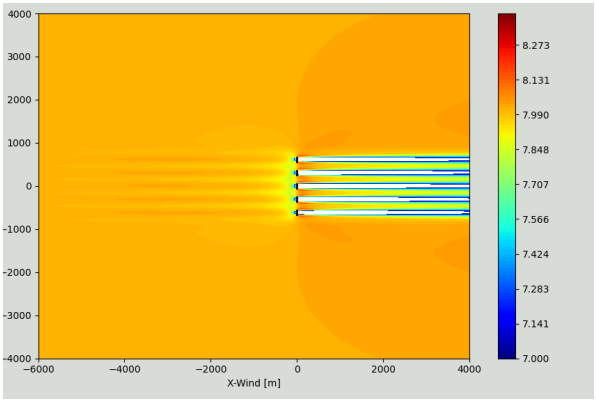

Figure 1: Colour plot of farm under stable conditions with pre-verification settings

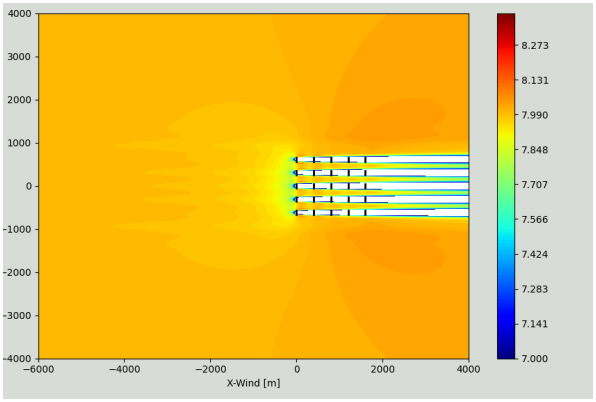

Figure 2: Colour plot of farm under stable conditions with post-verification settings

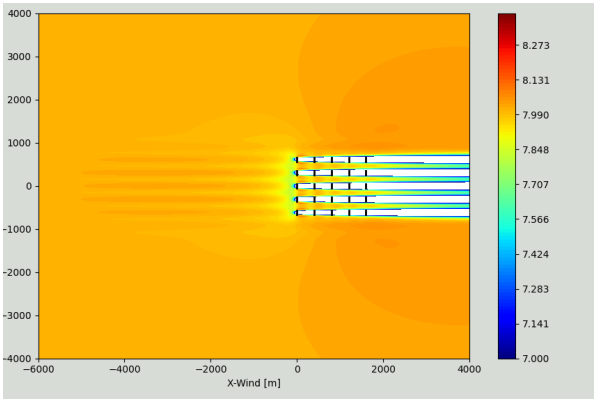

Figure 3: Colour plot of farm under neutral conditions with pre-verification settings

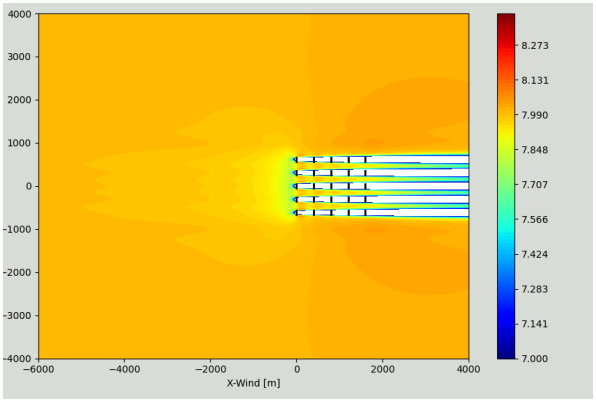

Figure 4: Colour plot of farm under neutral conditions with post-verification settings

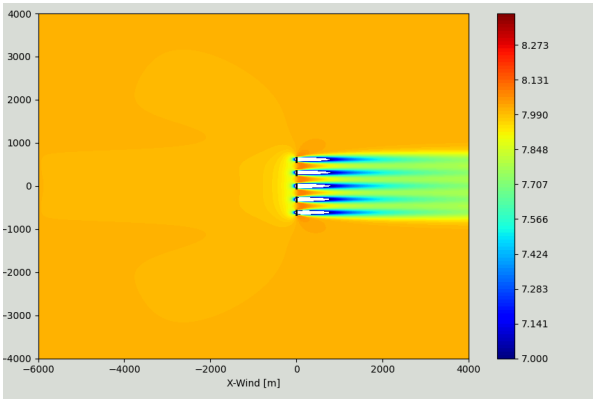

Figure 5: Colour plot of farm under unstable conditions with pre-verification settings

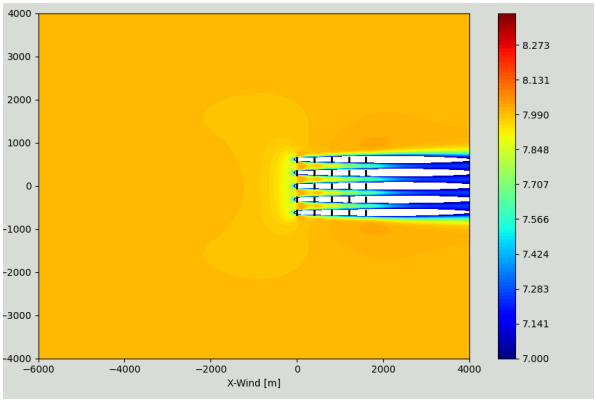

Figure 6: Colour plot of farm under unstable conditions with post-verification settings

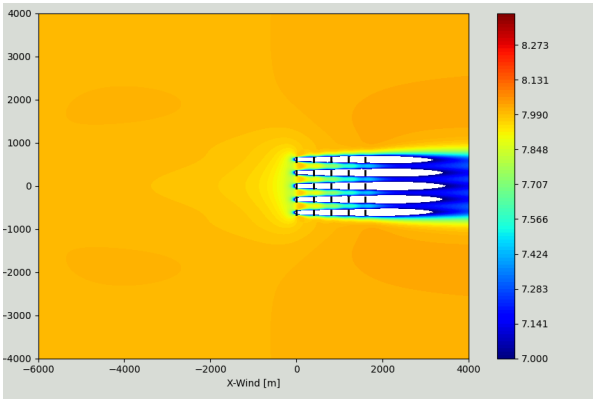

Figure 7: Colour plot of farm under very unstable conditions with pre-verification settings

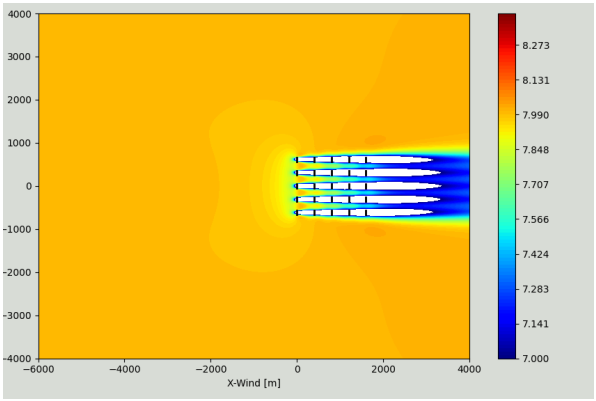

Figure 8: Colour plot of farm under very unstable conditions with post-verification settings

Appendix C - Grid convergence study

This Appendix Chapter presents the complete results of the Grid Convergence Study (GCS) with which the ratio's in Section 4.2.4 are calculated. In Tables 12 - 15 0 is given when no grid points were present in the corresponding rotor. Tables 12 - 13 present the non-normalised power output results, while Tables 14 - 15 show the normalised power output results over the theoretical power curve, as shown in Figure 2.11.

Table 12: Absolute results convergence study at fringe intensity 1.1

Fringe	Ny	Nz	A1	B1	C1	D1	E1
1.1	50	20	0	1201.21	0	1201.21	0
1.1	50	50	0	1208.05	0	1208.05	0
1.1	50	100	0	1193.19	0	1193.19	0
1.1	300	20	870.6	851.68	778.41	851.68	870.6
1.1	300	50	873.38	835.67	766.49	835.67	873.38
1.1	300	100	866.86	834.05	767.86	834.05	866.86
1.1	625	20	858.17	856.04	855.05	856.04	858.17
1.1	625	50	852.72	844.03	836.51	844.03	852.72
1.1	625	100	850.53	839.3	829.08	839.3	850.53
1.1	1000	20	860.31	857.11	856.69	857.11	860.31
1.1	1000	50	850.73	847.45	849.36	847.45	850.73
1.1	1000	100	845.76	842.57	846.46	842.57	845.76

Table 13: Absolute results convergence study at fringe intensity 1.2

Fringe	Ny	Nz	A1	B1	C1	D1	E1
1.2	50	20	0	1200	0	1200	0
1.2	50	50	0	1206.94	0	1206.94	0
1.2	50	100	0	1192.09	0	1192.09	0
1.2	300	20	869.98	851.03	777.71	851.03	869.98
1.2	300	50	872.85	835.03	765.74	835.03	872.85
1.2	300	100	866.32	833.42	767.24	833.42	866.32
1.2	625	20	857.58	855.36	854.28	855.36	857.58
1.2	625	50	852.21	843.36	835.64	843.36	852.21
1.2	625	100	850.01	838.65	828.36	838.65	850.01
1.2	1000	20	859.71	856.42	855.92	856.42	859.71
1.2	1000	50	850.22	846.77	848.47	846.77	850.22
1.2	1000	100	845.25	841.91	845.71	841.91	845.25

Note that in Tables 14 and 15 a low N_z consistently lead to the highest average power output, while a high N_z consistently lead to the lowest average power output. The impact of N_y on the power output is less notable.

Table 14: Normalised results over theoretical power from power curve of convergence study at fringe intensity 1.1

Fringe	Ny	Nz	A1	B1	C1	D1	E1	Average
1.1	50	20	0	1.314	0	1.314	0	0.5256
1.1	50	50	0	1.322	0	1.322	0	0.5288
1.1	50	100	0	1.305	0	1.305	0	0.522
1.1	300	20	0.953	0.932	0.852	0.932	0.953	0.9244
1.1	300	50	0.956	0.914	0.839	0.914	0.956	0.9158
1.1	300	100	0.948	0.913	0.84	0.913	0.948	0.9124
1.1	625	20	0.939	0.937	0.936	0.937	0.939	0.9376
1.1	625	50	0.933	0.923	0.915	0.923	0.933	0.9254
1.1	625	100	0.931	0.918	0.907	0.918	0.931	0.921
1.1	1000	20	0.941	0.938	0.937	0.938	0.941	0.939
1.1	1000	50	0.931	0.927	0.929	0.927	0.931	0.929
1.1	1000	100	0.925	0.922	0.926	0.922	0.925	0.924

Table 15: Normalised results over theoretical power from power curve of convergence study at fringe intensity 1.2

Fringe	Ny	Nz	A1	B1	C1	D1	E1	Average
1.2	50	20	0	1.313	0	1.313	0	0.5252
1.2	50	50	0	1.321	0	1.321	0	0.5284
1.2	50	100	0	1.304	0	1.304	0	0.5216
1.2	300	20	0.952	0.931	0.851	0.931	0.952	0.9234
1.2	300	50	0.955	0.914	0.838	0.914	0.955	0.9152
1.2	300	100	0.948	0.912	0.839	0.912	0.948	0.9118
1.2	625	20	0.938	0.936	0.935	0.936	0.938	0.9366
1.2	625	50	0.932	0.923	0.914	0.923	0.932	0.9248
1.2	625	100	0.93	0.918	0.906	0.918	0.93	0.9204
1.2	1000	20	0.941	0.937	0.936	0.937	0.941	0.9384
1.2	1000	50	0.93	0.926	0.928	0.926	0.93	0.928
1.2	1000	100	0.925	0.921	0.925	0.921	0.925	0.9234

Appendix D - Atmospheric stability classifications

This Appendix Chapter summarizes the stability classifications investigated during the literature research of this thesis. Note that the classifications in Tables 16-18 are based on the Obukhov length, L, as explained in Section 2.2.2. While the classifications in Tables 19-21 are based on the Obukhov parameter, z/L, each with their proper reference height, as explained in Section 2.2.2. The caption of every Table shows the relevant researchers and references are included.

Table 16: Stability Classification [A. van Wijk (1988) [16], J.P. Coelingh (1996) [17], M. Motta (2005) [5], Andrea Venora (2009) [18]]

Stability Class	Range
Very stable	0 < L < 200 m
Stable	200 < L < 1000 m
Near-neutral	|L| > 1000 m
Unstable	-1000 < L < -200 m
Very unstable	-200 < L < 0 m

Table 17: Stability Classification [Maarten Holtslag] (2016) [19]

Stability Class	Range
Very stable	0 < L ≤ 80 m
Stable	80 < L ≤ 480 m
Neutral	480 ≤ L or L ≤ -80 m
Unstable	-80 ≤ L < -20 m
Very unstable	-20 ≤ L < 0 m

Table 18: Stability Classification [Sven Erik Gryning (2007) [20], A. Peña (2008) [21]], A. Sathe (2011) [22], R. Barthelmie (2015) [23]

Stability Class	Range
Very stable	10 < L < 50 m
Stable	50 < L < 200 m
near neutral/stable	200 < L < 500 m
Neutral	|L| > 500 m
near neutral/unstable	−500 < L < −200 m
Unstable	-200 < L < -100 m
Very unstable	-100 < L < −50 m

Table 19: Stability Classification [Sorbjan and Grachev][24], z = 40 m

Stability Class	Range
Extremely stable	$\zeta > 50$
Very stable	$0.6 < \zeta < 50$
Weakly stable	$0.02 < \zeta < 0.6$
Near neutral	$0 < \zeta < 0.02$

Table 20: Stability Classification [Sanz Rodrigo] [25], z = 80 m

Stability Class	Range
Extremely stable	$\zeta > 2$
Very stable	$0.6 < \zeta < 2$
Stable	$0.2 < \zeta < 0.6$
Weakly stable	$0.02 < \zeta < 0.2$
Near neutral	$0 < \zeta < 0.02$

Table 21: Stability Classification [Peña] [26], z = 15 m

Stability Class	Range
stable	$0.03 < \zeta < 3$
neutral	$\lvert\zeta\rvert < 0.03$
unstable	$-0.2 < \zeta < -0.03$
very unstable	$-1.5 < \zeta < -0.2$

Appendix E - GBE loss results

This Appendix Chapter presents the results of the calculated GBE, for all investigated stability classes, farm setups and wind speeds, for the sake of completion.

Table 22: Power losses (%) due to the GBE of the aligned farm calculated through the FR approach

	3 m/s	4 m/s	5 m/s	6 m/s	7 m/s	8 m/s	9 m/s	10 m/s	11 m/s	12 m/s	13 m/s	14 m/s	15 m/s	16 m/s	17 m/s	18 m/s
Very unstable	-46.56	2.61	1.67	1.75	1.69	1.69	1.69	1.51	0.89	0.17	0.01	0.00	0.00	0.00	0.00	0.00
Unstable	-29.85	2.56	1.60	1.68	1.64	1.63	1.63	1.48	0.90	0.18	0.01	0.00	0.00	0.00	0.00	0.00
Neutral	-22.73	2.60	1.55	1.62	1.56	1.54	1.55	1.45	0.93	0.20	0.01	0.00	0.00	0.00	0.00	0.00
Unstable	-18.25	2.73	1.62	1.73	1.67	1.66	1.67	1.56	1.02	0.23	0.02	0.00	0.00	0.00	0.00	0.00
Very stable	-19.39	3.28	1.90	1.98	1.91	1.87	1.88	1.80	1.22	0.30	0.02	0.00	0.00	0.00	0.00	0.00

Table 23: Power losses (%) due to the GBE of the staggered farm calculated through the FR approach

	3 m/s	4 m/s	5 m/s	6 m/s	7 m/s	8 m/s	9 m/s	10 m/s	11 m/s	12 m/s	13 m/s	14 m/s	15 m/s	16 m/s	17 m/s	18 m/s
Very unstable	-63.95	3.77	2.36	2.44	2.34	2.32	2.35	2.06	1.11	0.16	0.01	0.00	0.00	0.00	0.00	0.00
Unstable	-43.14	3.79	2.32	2.45	2.34	2.33	2.34	2.08	1.17	0.18	0.01	0.00	0.00	0.00	0.00	0.00
Neutral	-33.45	3.98	2.37	2.47	2.38	2.37	2.39	2.16	1.27	0.21	0.01	0.00	0.00	0.00	0.00	0.00
Unstable	-29.55	4.52	2.66	2.80	2.69	2.65	2.68	2.44	1.49	0.26	0.02	0.00	0.00	0.00	0.00	0.00
Very stable	-31.96	5.69	3.27	3.40	3.26	3.21	3.23	3.00	1.90	0.36	0.02	0.00	0.00	0.00	0.00	0.00

Table 24: Power losses (%) due to the GBE of the aligned farm calculated through the ST approach

	3 m/s	4 m/s	5 m/s	6 m/s	7 m/s	8 m/s	9 m/s	10 m/s	11 m/s	12 m/s	13 m/s	14 m/s	15 m/s	16 m/s	17 m/s	18 m/s
Very unstable	-15.60	1.16	0.78	0.86	0.83	0.83	0.81	0.77	0.50	0.12	0.01	0.00	0.00	0.00	0.00	0.00
Unstable	-10.14	1.20	0.78	0.81	0.80	0.78	0.76	0.73	0.51	0.13	0.01	0.00	0.00	0.00	0.00	0.00
Neutral	-9.14	1.27	0.75	0.77	0.74	0.71	0.71	0.71	0.52	0.15	0.01	0.00	0.00	0.00	0.00	0.00
Unstable	-8.70	1.42	0.81	0.87	0.84	0.84	0.83	0.82	0.61	0.18	0.01	0.00	0.00	0.00	0.00	0.00
Very stable	-10.78	2.06	1.20	1.27	1.23	1.20	1.19	1.18	0.85	0.25	0.02	0.00	0.00	0.00	0.00	0.00

Table 25: Power losses (%) due to the GBE of the staggered farm calculated through the ST approach

	3 m/s	4 m/s	5 m/s	6 m/s	7 m/s	8 m/s	9 m/s	10 m/s	11 m/s	12 m/s	13 m/s	14 m/s	15 m/s	16 m/s	17 m/s	18 m/s
Very unstable	-29.32	2.34	1.47	1.55	1.49	1.46	1.48	1.31	0.73	0.12	0.01	0.00	0.00	0.00	0.00	0.00
Unstable	-21.41	2.44	1.50	1.58	1.50	1.49	1.49	1.34	0.78	0.13	0.01	0.00	0.00	0.00	0.00	0.00
Neutral	-18.67	2.67	1.58	1.63	1.57	1.54	1.56	1.43	0.87	0.15	0.01	0.00	0.00	0.00	0.00	0.00
Unstable	-19.09	3.23	1.87	1.95	1.88	1.84	1.85	1.71	1.08	0.21	0.01	0.00	0.00	0.00	0.00	0.00
Very stable	-22.45	4.49	2.58	2.71	2.58	2.55	2.55	2.38	1.54	0.31	0.02	0.00	0.00	0.00	0.00	0.00

Bibliography

[1] V. e. a. Masson-Delmotte, "Climate change 2021: The physical science basis summary for policymakers," *Climate Change 2021: The Physical Science Basis. Contribution of Working Group I to the Sixth Assessment Report of the Intergovernmental Panel on Climate Change*, 2021.

[2] A. R. Henderson, "Offshore wind in Europe: The current state of the art," *Refocus*, vol. 3, no. 2, pp. 14–17, 2021.

[3] WindREN, "Summary of the workshop regarding the Wind Farm Blockage Effect for onshore wind farms , at WinterWind , February 3rd , 2020 Background," in *WinterWind 2020*, p. 5, 2020.

[4] R. B. Stull, *An introduction to boundary layer meteorology*. Dordrecht: Kluwer Academic Publishers, 1988.

[5] M. Motta, R. J. Barthelmie, and PVølund, "The influence of non-logarithmic wind speed profiles on potential power output at danish offshore sites," *Wind Energy*, vol. 8, no. 2, pp. 219–236, 2005.

[6] R. J. Barthelmie, "The effects of atmospheric stability on coastal wind climates," *Meteorological Applications*, vol. 6, no. 1, pp. 39–47, 1999.

[7] J. Schneemann, A. Rott, M. Dörenkämper, G. Steinfeld, and M. Kühn, "Cluster wakes impact on a far-distant offshore wind farm's power," *Wind Energy Science*, vol. 5, no. 1, pp. 29–49, 2020.

[8] D. Medici, S. Ivanell, J. Å. Dahlberg, and P. H. Alfredsson, "The upstream flow of a wind turbine: Blockage effect," *Wind Energy*, vol. 14, no. 5, pp. 691–697, 2011.

[9] R. V. Rodrigues and C. Lengsfeld, "Aligned and Staggered Layouts : What is the Impact on Wind Farms Land-Use?," *Preprints 2020*, vol. 2020070315, no. 1, pp. 1–21, 2020.

[10] E. Branlard and R. Applications, *Wind Turbine Aerodynamics and Methods*. Springer, 2017.

[11] A. Segalini, "Linearized simulation of flow over wind farms and complex terrains," *Philosophical Transactions of the Royal Society A: Mathematical, Physical and Engineering Sciences*, vol. 375:201600, 2017.

[12] B. Landers, *Mixing Characteristics of Turbulent Twin Impinging Axisymmetric Jets at Various Impingement Angles*. PhD thesis, University of Florida, 2014.

[13] J. Nordström, N. Nordin, and D. Henningson, "Fringe region technique and the Fourier method used in the direct numerical simulation of spatially evolving viscous flows," *SIAM Journal on Scientific Computing*, vol. 20, no. 4, pp. 1365–1393, 1999.

[14] P. Schlatter, N. A. Adams, and L. Kleiser, "A windowing method for periodic inflow/outflow boundary treatment of non-periodic flows," *Journal of Computational Physics*, vol. 206, no. 2, pp. 505–535, 2005.

[15] J. Jeppsson, P. E. Larsen, and A. Larsson, "Technical Description Lillgrund Wind Power Plant," *Vattenfall Vindkraft AB*, no. September, p. 79, 2008.

[16] A. J. Van Wijk, A. C. Beljaars, A. A. Holtslag, and W. C. Turkenburg, "Evaluation of stability corrections in wind speed profiles over the North Sea," *Journal of Wind Engineering and Industrial Aerodynamics*, vol. 33, no. 3, pp. 551–566, 1990.

[17] J. P. Coelingh, A. J. Van Wijk, and A. A. Holtslag, “Analysis of wind speed observations over the North Sea,” *Journal of Wind Engineering and Industrial Aerodynamics*, vol. 61, no. 1, pp. 51–69, 1996.

[18] A. Venora, “Monin-Obukhov Similarity Theory Applied to Offshore Wind Data,” *Thesis*, no. August, pp. 1–110, 2009.

[19] M. C. Holtslag, W. A. Bierbooms, and G. J. Van Bussel, “Estimating atmospheric stability from observations and correcting wind shear models accordingly,” *Journal of Physics: Conference Series*, vol. 555, no. 1, 2014.

[20] S. E. Gryning, E. Batchvarova, B. Brümmer, H. Jørgensen, and S. Larsen, “On the extension of the wind profile over homogeneous terrain beyond the surface boundary layer,” *Boundary-Layer Meteorology*, vol. 124, no. 2, pp. 251–268, 2007.

[21] A. Peña, S. E. Gryning, and C. B. Hasager, “Measurements and modelling of the wind speed profile in the marine atmospheric boundary layer,” *Boundary-Layer Meteorology*, vol. 129, no. 3, pp. 479–495, 2008.

[22] A. Sathe, S.-E. Gryning, and A. Peña, “Comparison of the atmospheric stability and wind profiles at two wind farm sites over a long marine fetch in the North Sea,” *Wind Energy*, vol. 14, no. 6, pp. 767–780, 2011.

[23] R. J. Barthelmie, M. J. Churchfield, P. J. Moriarty, J. K. Lundquist, G. S. Oxley, S. Hahn, and S. C. Pryor, “The role of atmospheric stability/turbulence on wakes at the Egmond aan Zee offshore wind farm,” *Journal of Physics: Conference Series*, vol. 625, no. 1, pp. 1–10, 2015.

[24] Z. Sorbjan and A. A. Grachev, “An evaluation of the flux-gradient relationship in the stable boundary layer,” *Boundary-Layer Meteorology*, vol. 135, no. 3, pp. 385–405, 2010.

[25] J. S. Rodrigo, E. Cantero, B. García, F. Borbón, U. Irigoyen, S. Lozano, P. M. Fernande, and R. A. Chávez, “Atmospheric stability assessment for the characterization of offshore wind conditions,” *Journal of Physics: Conference Series*, vol. 625, no. 1, 2015.

[26] A. Peña, P. E. Réthoré, and O. Rathmann, “Modeling large offshore wind farms under different atmospheric stability regimes with the Park wake model,” *Renewable Energy*, vol. 70, pp. 164–171, 2014.

[27] J. Delbeke, A. Runge-Metzger, Y. Slingenberg, and J. Werksman, “The paris agreement,” *Towards a Climate-Neutral Europe: Curbing the Trend*, pp. 24–45, 2019.

[28] T. Gerden, “The adoption of the kyoto protocol of t he united nations framework convention on climate change,” *Prispevki za Novejso Zgodovino*, vol. 58, no. 2, 2018.

[29] IEA (2020), “Global Energy Review 2020,” *IEA, Paris*, 2020.

[30] International Energy Agency, “Global Energy Review 2021,” *Global Energy Review 2020*, pp. 1–36, 2021.

[31] IRENA, *Future of Wind: Deployment, investment, technology, grid integration and socio-economic aspects*. Abu Dhabi: International Renewable Energy Agency, 2019.

[32] F. Porté-agel, M. Bastankhah, and S. Shamsoddin, *Wind-Turbine and Wind-Farm Flows : A Review*. Springer Netherlands, 2020.

[33] A. R. Meyer Forsting and N. Troldborg, “The effect of blockage on power production for laterally aligned wind turbines,” *Journal of Physics: Conference Series*, vol. 625, no. 1, 2015.

[34] P. Gebraad, *DATA-DRIVENWIND PLANT CONTROL*. PhD thesis, TU Delft, 2014.

[35] J. Bleeg, M. Purcell, R. Ruisi, and E. Traiger, "Wind farm blockage and the consequences of neglecting its impact on energy production," *Energies*, vol. 11, no. 6, 2018.

[36] J. M. Strickland and R. J. Stevens, "Effect of thrust coefficient on the flow blockage effects in closely-spaced spanwise-infinite turbine arrays," *Journal of Physics: Conference Series*, vol. 1618, no. 6, 2020.

[37] D. Allaerts and J. Meyers, "Gravity Waves and Wind-Farm Efficiency in Neutral and Stable Conditions," *Boundary-Layer Meteorology*, vol. 166, no. 2, pp. 269–299, 2018.

[38] R. Ebenhoch, *Simplified modeling of wind-farm flows*. PhD thesis, KTH Royal Institute of Technology, 2015.

[39] I. N. Nisbet, "Cumulative Induction Zone (Global Blockage) Effect," 2020.

[40] D. B. Jiménez Douglas, "WIND FARM BLOCKAGE EFFECT," 2020.

[41] E. Branlard, E. Quon, A. R. Meyer Forsting, J. King, and P. Moriarty, "Wind farm blockage effects: Comparison of different engineering models," *Journal of Physics: Conference Series*, vol. 1618, no. 6, pp. 1–11, 2020.

[42] M. Abkar and F. Porté-Agel, "Influence of atmospheric stability on wind-turbine wakes: A large-eddy simulation study," *Physics of Fluids*, vol. 27, no. 3, 2015.

[43] B. R. Sutherland, *Internal gravity waves*. Cambridge: Cambridge University Press, 2010.

[44] T. Foken, "50 years of the Monin-Obukhov similarity theory," *Boundary-Layer Meteorology*, vol. 119, no. 3, pp. 431–447, 2006.

[45] D. Allaerts and J. Meyers, "Boundary-layer development and gravity waves in conventionally neutral wind farms," *Journal of Fluid Mechanics*, vol. 814, pp. 95–130, 2017.

[46] J. R. Holton, *An introduction to Dynamic Meteorology*. Academic Press, 2004.

[47] J. E. Cermak and L. S. Cochran, "Physical modelling of the atmospheric surface layer," *Journal of Wind Engineering and Industrial Aerodynamics*, vol. 42, no. 1-3, pp. 935–946, 1992.

[48] M. Z. Jacobson, *Fundamentals of Atmospheric Modeling*. Cambridge University Press, 5 2005.

[49] S. Larsen, "The atmospheric boundary layer over land and sea: Focus on the off-shore Southern Baltic and Southern North Sea region.," Tech. Rep. February, DTU Wind Energy, 2013.

[50] B. Zäncker, M. Cunliffe, and A. Engel, "Eukaryotic community composition in the sea surface microlayer across an east-west transect in the Mediterranean Sea," *Biogeosciences*, vol. 18, no. 6, pp. 2107–2118, 2021.

[51] S. Emeis, "Current issues in wind energy meteorology," *Meteorological Applications*, vol. 21, no. 4, pp. 803–819, 2014.

[52] K. L. Wu and F. Porté-Agel, "Flow adjustment inside and around large finite-size wind farms," *Energies*, vol. 10, no. 12, pp. 4–9, 2017.

[53] M. Holtslag, *Far offshore wind conditions in scope of wind energy*. PhD thesis, TU Delft, 2016.

[54] J. A. P. Veiga and M. R. Queiroz, "Impact of the Waves on the Sea Surface Roughness Length under Idealized Like-Hurricane Wind Conditions (Part II)," *Atmospheric and Climate Sciences*, vol. 05, no. 03, pp. 326–335, 2015.

[55] D. Allaerts and J. Meyers, “Large eddy simulation of a large wind-turbine array in a conventionally neutral atmospheric boundary layer,” *Physics of Fluids*, vol. 27, no. 6, 2015.

[56] E. Fennell, *Comparison of Onshore and Offshore Boundary Layers in the HARMONIE Model for Wind Energy Purposes*. PhD thesis, Wageningen University, 2018.

[57] A. Peña and S. E. Gryning, “Charnock’s roughness length model and non-dimensional wind profiles over the sea,” *Boundary-Layer Meteorology*, vol. 128, no. 2, pp. 191–203, 2008.

[58] K. S. M. Essa, “Estimation of Monin-Obukhov Length Using Richardson and Bulk Richardson Number,” *Conference on Nuclear and Particle Physics*, vol. 591, no. 1, pp. 591–602, 1999.

[59] J. Schneemann, F. Theuer, A. Rott, M. Dörenkämper, and M. Kühn, “Offshore wind farm global blockage measured with scanning lidar,” *Wind Energy Science*, vol. 6, no. 2, pp. 521–538, 2021.

[60] T. Foken and M. Börngen, “Lettau’s Contribution to the Obukhov Length Scale: A Scientific Historical Study,” *Boundary-Layer Meteorology*, vol. 179, no. 3, pp. 369–383, 2021.

[61] T. Nishino and S. Draper, “Local blockage effect for wind turbines,” *Journal of Physics: Conference Series*, vol. 625, no. 1, 2015.

[62] N. Troldborg and A. R. Meyer Forsting, “A simple model of the wind turbine induction zone derived from numerical simulations,” *Wind Energy*, vol. 20, no. 12, pp. 2011–2020, 2017.

[63] M. Asimakopoulos, P. Clive, G. More, and R. Boddington, “Offshore compression zone measurement and visualization,” *European Wind Energy Association Conference and Exhibition 2014, EWEA 2014*, pp. 1–10, 2014.

[64] T. Nishino and R. H. Willden, “The efficiency of an array of tidal turbines partially blocking a wide channel,” *Journal of Fluid Mechanics*, vol. 708, pp. 596–606, 2012.

[65] A. Sebastiani, F. Castellani, G. Crasto, and A. Segalini, “Data analysis and simulation of the Lillgrund wind farm,” *Wind Energy*, no. January, pp. 1–15, 2020.

[66] IEC 61400–12, “Power performance measurements of electricity producing wind turbines,” *61400–12*, vol. 2005, p. 90, 2005.

[67] O. Apata and D. T. Oyedokun, “An overview of control techniques for wind turbine systems,” *Scientific African*, vol. 10, 2020.

[68] R. J. Stevens, D. F. Gayme, and C. Meneveau, “Large eddy simulation studies of the effects of alignment and wind farm length,” *Journal of Renewable and Sustainable Energy*, vol. 6, no. 2, 2014.

[69] A. Segalini and J. Å. Dahlberg, “Blockage effects in wind farms,” *Wind Energy*, vol. 23, no. 2, pp. 120–128, 2020.

[70] A. Segalini and F. Castellani, “Wind-farm simulation over moderately complex terrain,” *Journal of Physics: Conference Series*, vol. 854, no. 1, 2017.

[71] R. Braunbehrens and A. Segalini, “A statistical model for wake meandering behind wind turbines,” *Journal of Wind Engineering and Industrial Aerodynamics*, vol. 193, no. June, 2019.

[72] R. Absi, “A simple eddy viscosity formulation for turbulent boundary layers near smooth walls,” *Comptes Rendus - Mecanique*, vol. 337, no. 3, pp. 158–165, 2009.

[73] J. Virieux and H. Calandra, “A review of the spectral , pseudo-spectral , finite-difference and finite-element modelling techniques for geophysical imaging,” *Geophysical Prospecting*, vol. 59, no. 5, pp. 794–813, 2011.

[74] B. L. Sill, “Turbulent boundary layer profiles over uniform rough surfaces,” *Journal of Wind Engineering and Industrial Aerodynamics*, vol. 31, no. 2-3, pp. 147–163, 1988.

[75] N. J. Cook, “The Deaves and Harris ABL model applied to heterogeneous terrain,” *Journal of Wind Engineering and Industrial Aerodynamics*, vol. 66, no. 3, pp. 197–214, 1997.

[76] M. Zaayer and A. Vire, “Introduction to wind turbines: physics and technology,” 2018.

[77] S. Emeis and M. Turk, “Comparison of Logarithmic Wind Profiles and Power Law Wind Profiles and their Applicability for Offshore Wind Profiles,” *Wind Energy*, no. February 2007, pp. 61–64, 2007.

[78] B. Wasistho, B. J. Geurts, and J. G. Kuerten, “Simulation techniques for spatially evolving instabilities in compressible flow over a flat plate,” *Computers and Fluids*, vol. 26, no. 7, pp. 713–739, 1997.

[79] P. Spalart, “Direct Numerical Study of Leading-Edge Contamination,” *Fluid Dynamics of 3D Turbulent Shear Flows and Transition*, 1988.

[80] A. Lundbladh, S. Berlin, M. Skote, C. Hildings, J. Choi, J. Kim, and D. S. Henningson, “An efficient spectral method for simulation of incompressible flow over a flat plate,” *Technical Report*, 1999.

[81] A. Sebastiani, F. Castellani, G. Crasto, and A. Segalini, “Data analysis and simulation of the Lillgrund wind farm,” *Wind Energy*, vol. 24, no. 6, pp. 634–648, 2021.

[82] S. Ivanell, K. Nillson, O. Erikkson, S. Söderberg, and I. Carlén, “Wind turbine wakes and wind farm wakes,” tech. rep., Energiforsk, 2018.

[83] I. Troen and E. Lundtang Petersen, *European wind atlas*. Roskilde: Risø National Laboratory, 1989.

[84] A. C. Creech, W. G. Früh, and A. E. Maguire, “High-resolution CFD modelling of lillgrund wind farm,” *Renewable Energy and Power Quality Journal*, vol. 1, no. 11, pp. 983–988, 2013.

[85] N. G. Mortensen, L. Landberg, I. Troen, and E. Lundtang Petersen, “Wind Atlas Analysis and Application Program (WASP) Vol. 1: Getting Started,” tech. rep., Risø National Laboratory, 1998.

[86] A. Segalini, “ORFEUS - A User Manual,” 2020.

[87] A. Sathe and W. Bierbooms, “Influence of different wind profiles due to varying atmospheric stability on the fatigue life of wind turbines,” *Journal of Physics: Conference Series*, vol. 75, no. 1, 2007.

[88] J. Bleeg, D. Digraskar, J. Woodcock, and J.-F. Corbett, “Modeling stable thermal stratification and its impact on wind flow over topography,” *AWEA Windpower*, no. January 2014, pp. 1–20, 2012.

[89] J. Strickland, *Modeling wakes and blockage in large-scale wind farms*. PhD thesis, University of Twente, 2021.

[90] S. McTavish, D. Feszty, and F. Nitzsche, “A study of the performance benefits of closely-spaced lateral wind farm configurations,” *Renewable Energy*, vol. 59, pp. 128–135, 2013.

[91] M. Popescu and T. Flåtten, “A Study of Blockage Effects at the Wind Turbine and Wind Farm Scales,” *Energies*, vol. 14, no. 6124, pp. 1–19, 2021.